

ADVANCED HIGH-TEMPERATURE SHAPE-MEMORY ALLOY DEVELOPMENT
AND THERMOMECHANICAL CHARACTERIZATION OF PLATINUM AND
PALLADIUM MODIFIED NiTi BASED SMA_s

By

ORLANDO RIOS

A THESIS PRESENTED TO THE GRADUATE SCHOOL
OF THE UNIVERSITY OF FLORIDA IN PARTIAL FULFILLMENT
OF THE REQUIREMENTS FOR THE DEGREE OF
MASTER OF SCIENCE

UNIVERSITY OF FLORIDA

2006

Copyright 2006

by

Orlando Rios

To my father and family

ACKNOWLEDGMENTS

I thank my mother and father. I thank my family for not letting distance separate us. I thank the great friends I have made here. I would like to thank Dr. Nathal and Dr. Ronald Noebe of the NASA Glenn Research Center's Advanced Structures Division for their support, guidance, materials and processing and unlimited use of the division's characterization and mechanical testing facilities. Without their support I would not have an acknowledgments section to write nor would I have as interesting a study. I would like to thank the kind effort of my committee members. I would like to thank Dr. Donnelly for her support and guidance at all times, and all of my colleagues here and afar.

TABLE OF CONTENTS

	<u>page</u>
ACKNOWLEDGMENTS	iv
LIST OF TABLES	viii
LIST OF FIGURES	ix
ABSTRACT	xiii
CHAPTER	
1 INTRODUCTION AND BACKGROUND	1
Significance	1
Background.....	3
General Shape Memory Alloy Behavior	3
SMA Structural Characteristics.....	4
SMA Mechanical Behavior	10
Thermoelastic Shear Transformations.....	12
2 MATERIALS PROCESSING AND PROCEDURES	22
Melting Procedures.....	22
Arc Melting	22
Arc Melt Machining	22
Induction Melting.....	23
Homogenization	23
Extrusion.....	24
Stress Relief Heat Treatment.....	25
Characterization Procedures	25
Dynamic Modulus	25
Compositional Analysis.....	26
Nitrogen, Oxygen, Carbon and Sulfur Analysis.....	27
Thermal Analysis.....	28
Microstructural and Semi-Quantitative Compositional Analysis.....	30
Dilatometry Measurements	31
Resistivity Measurements.....	31
Sample instrumentation.....	31
Resistivity apparatus	32

Thermomechanical Testing	37
Thermomechanical instrumentation	37
Uniaxial isothermal mechanical tests	39
Load free strain recovery tests	40
Load bias test.....	40
3 ALLOY DEVELOPMENT	50
Characterization of the NiTiPt SMA system	50
Bulk Compositional Analysis.....	50
Transformation Temperature.....	51
Microstructure	53
Alloy Selection : NiTiPt	55
Alloy Selection : NiTiPd	57
Alloy Selection Summary.....	60
4 RESULTS AND DISCUSSION.....	68
Heat Treatment Optimization	68
Characterization.....	70
Materials Characterization.....	70
Properties and Transformation Temperatures	70
Thermomechanical Testing	74
Isothermal Stress-Strain Behavior in Tension and Compression.....	74
Isothermal stress-strain behavior in tension and compression NiTiPd	75
Dynamic elastic modulus determination NiTiPd	82
Isothermal stress-strain behavior in tension and compression NiTiPt	83
Unconstrained Recovery Tests.....	86
Unconstrained recovery tests NiTiPd.....	86
Unconstrained recovery tests NiTiPt.....	89
Constant-Load, Strain-Temperature Tests and Work Output.....	90
Constant-load, strain-temperature tests and work output : NiTiPd.....	91
Constant-load, strain-temperature tests and work output:NiTiPt.....	96
5 SUMMARY AND CONCLUSIONS	116
Alloy Development.....	116
Characterization and Thermomechanical Testing	117
Conclusions Relevant to Alloy Design.....	120
Future Studies	121
APPENDIX	
A NiTiPd HTSMA MATERIAL DATA SHEET	123
Physical Properties.....	123
Electrical Resistivity.....	123
Thermal Coefficient of Resistivity	123

Coefficient of Thermal Expansion	123
Shape Memory Properties.....	123
Transformation Temperatures	123
Composition.....	123
B NiTiPt HTSMA MATERIAL DATA SHEET	124
Physical Properties.....	124
Electrical Resistivity.....	124
Thermal Coefficient of Resistivity	124
Coefficient of Thermal Expansion	124
Shape Memory Properties.....	124
Transformation Temperatures	124
Composition.....	124
C CHEMICAL ANALYSIS OF EXTRUDED MATERIALS	125
LIST OF REFERENCES.....	126
BIOGRAPHICAL SKETCH	130

LIST OF TABLES

<u>Table</u>	<u>page</u>
1-1 Several characteristics common to metallic thermal SMA.	13
3-2 Aim and measured compositions of all alloys investigated.	61
3-3 Transformation temperatures of alloy set.	62
3-4 Semi-quantitative EDS analysis of the various phases observed.	64

LIST OF FIGURES

<u>Figure</u>	<u>page</u>
1-1 Power-to-weight ratio versus weight diagram for common actuator types currently used in aeronautics.....	16
1-2 Idealized plot of a property change vs. temperature	17
1-3 Structure of the parent phase (austenite) and shear phases (B19 and B19' martensite).....	18
1-4 Thermoelastic transformation and twin accommodated transformation strain.....	19
1-5 Two-dimensional lattice schematic of monoclinic structures.....	19
1-6 TEM micrographs of twinned and untwined monoclinic martensite.....	19
1-7 Effects of thermal cycling through the hysteresis on the transformation temperatures of several NiTi based shape memory alloys.....	20
1-8 Deformation and shape recovery by detwinning (twins marked with arrows)	20
1-9 Isothermal stress strain behavior of a typical SMA strained in the fully martensitic state.....	21
1-10 Stress strain behavior showing the three main deformation regimes active in SMAs.....	21
2-1 Induction melted Ni _{19.5} Pd ₃₀ Ti _{50.5} cast ingot with attached hot top on a quarter inch grid.....	41
2-2 Heat treatment and processing temperature schedule.	42
2-3 Hot extrusion press schematic.....	42
2-4 Uniaxial sample (A) 5 X 10 mm compression sample (B) Threaded 17.4 mm long by 3.81 mm diameter gauge sample.....	43
2-5 Processing flow diagram of DSC, compression, and tensile samples.....	43
2-6 The ICP using an Echelle type polychrometer.....	44

2-7	Example of a DTA scan showing the exothermic and endothermic peaks characteristic of thermoelastic shape memory alloys.....	44
2-8	Four-point probe resistivity configuration	45
2-9	Raw (blue) and conditioned (yellow) voltage signals for resistivity measurements during inductive heating.....	45
2-10	Resistivity vs. temperature profile with regression analysis.....	46
2-11	High conductivity Pt wire resistivity vs. temperature relationship demonstrating the repeatability of the during heating and cooling.....	46
2-12	NIST (resistivity standard) resistivity vs. temperature profile comparison of NIST measurements and the measurements by the resistivity apparatus.....	47
2-13	Resistivity apparatus data flow diagram.	48
2-14	Materials Testing Systems (MTS) tensile frame fitted with high-temperature hot grips and induction heating configured for compressive testing.....	49
3-1	Ternary plot of the Ti-Ni-Pt compositions studied. The composition of all alloys was confirmed by spectrographic analysis.....	61
3-2	A. Effect of Pt on the M_s transformation temperatures for Ni _{50-x} Pt _x Ti ₅₀ alloys, including data from previous researchers B. Effect of Pt on all transformation temperatures for Ni _{50-x} Pt _x Ti ₅₀ alloys.....	62
3-3	SEM BSE micrographs of the non-stoichiometric alloys.	63
3-4	Phase diagrams (A) NiTi binary phase diagram from reference (B) TiPt binary phase diagram from reference	64
3-5	Effect of ternary alloying additions on the M_s (or M_p) temperature for NiTi-based high-temperature shape memory alloy systems	65
3-6	Comparison of the specific work output for several conventional NiTi alloys, SM495 NiTi, and the (Ni,Pt)Ti HITSMA.....	65
3-7	Phase diagram of TiPd±TiNi alloys.....	66
3-8	Shape memory properties NiTiPd (A) M_s temperature resulting from ternary alloy additions. (B) Average shape recovery in Ti ₅₀ (Ni _{50-x})Pd _x	66
3-9	Plots of martensitic transformation temperatures vs. composition for Ti _{50-x} Pd ₃₀ Ni _{20+x}	67

4-1	Stress Relief Heat Treatment Optimization by Analysis of Resistivity Temperature Profiles (note the resistivity curves are offset for convenience on the same resistivity scale).....	98
4-2	SEM BSE image of extruded Ni _{19.5} Ti _{50.5} Pd ₃₀	99
4-3	NiTiPt Resistivity and Dilatometry Test Results	99
4-4	NiTiPd Resistivity and Dilatometry Test Results	100
4-5	NiTiPd Force Strain Curve at 365°C.....	100
4-6	NiTiPd Alloy Uniaxial Isothermal Tensile Tests at RT, 200°C, 300°C and 400°C (a) Engineering Stress Strain Curve (b) True Stress Strain Curve including correction for non-uniform deformation of the 400C sample	101
4-7	NiTiPd Alloy Uniaxial Isothermal Compression Tests at RT, 200°C, 350°C, 365°C, 400°C and 500°C (a) Engineering Stress Strain Curve (b) True Stress Strain Curve.....	101
4-8	NiTiPd Alloy Uniaxial Isothermal Tensile Tests at 225°C, 245°C, 255°C and 272°C.....	102
4-9	NiTiPd Alloy Uniaxial Isothermal Compression Test at 255°C, 272°C and 300°C.....	102
4-10	Isothermal Uniaxial Stress Strain Curve with Resistivity Exhibiting a Stress Induced Transformations.....	103
4-11	NiTiPd Yield Stress vs. Temperature in tension and compression.....	103
4-12	Temperature Dependent Dynamic Elastic Modulus measured on heating	103
4-13	NiTiPt Alloy Uniaxial Isothermal Tensile Tests at 440°C, 470°C, 550°C and 600°C.....	104
4-14	NiTiPt Alloy Uniaxial Isothermal Compression Tests at 440°C, 470°C, 490°C, 550°C, and 600°C.....	105
4-15	NiTiPt Alloy Uniaxial Isothermal Tensile Tests at 200°C, 380°C, 400°C and 440°C.....	105
4-16	NiTiPt Alloy Uniaxial Isothermal Compression Tests at 200°C, 380°C, 400°C and 440°C.....	106
4-17	Stress Strain Curve at 500 Celsius at Low and High Strain Rates.....	106
4-18	Yield Stress vs. temperature for NiTiPt	107

4-19	Fracture Stress and Strain vs. temperature for NiTiPt	107
4-20	NiTiPd Unconstrained Recovery Test at 4 and 2 Percent Initial Strains.	108
4-21	Total Recovery Rate vs. Total Strain for NiTiPd.....	108
4-22	Load Free Recovery Individual Components of Total Recovery for NiTiPd.	109
4-23	Temperature Dependent Load Free Recovery Curve for Complete NiTiPt Test...109	
4-24	Load Free Recovery Individual Components of Total Recovery for NiTiPt.....	110
4-25	Load Bias in Tension (Specific Work Output) for NiTiPd	110
4-26	Load Bias in Compression (Specific Work Output) for NiTiPd.....	111
4-27	Load Bias in Tension (Specific Work Output) Complete Thermomechanical Path for NiTiPd	111
4-28	Specific Work vs. Biasing Load for NiTiPd	112
4-29	Transformation Strain (2 nd cycle martensite to austenite) vs. Biasing Load for NiTiPd	112
4-30	Open Loop Strain vs. Biasing Stress for NiTiPd	113
4-31	Load Bias in Compression (Specific Work Output) for NiTiPd.....	113
4-32	Transformation Strain (2 nd cycle martensite to austenite) vs. Biasing Load for NiTiPt.....	114
4-33	Specific Work vs. Biasing Load for NiTiPt	114
4-34	Open Loop Strain vs. Biasing Stress for NiTiPt	115

Abstract of Thesis Presented to the Graduate School
of the University of Florida in Partial Fulfillment of the
Requirements for the Degree of Master of Science

ADVANCED HIGH-TEMPERATURE SHAPE-MEMORY ALLOY DEVELOPMENT
AND THERMOMECHANICAL CHARACTERIZATION OF PLATINUM AND
PALLADIUM MODIFIED NiTi BASED SMAs

By

Orlando Rios

December 2006

Chair: Luisa Dempere

Major Department: Materials Science and Engineering

A series of Ti-Ni-Pt and Ti-Ni-Pd high temperature shape memory alloys (HTSMAs) have been examined in an effort to find alloys with a suitable balance of mechanical and physical properties for applications involving elevated temperature actuation. Initially, more than 20 Ti-Ni-Pt alloys were prepared by arc melting high purity materials followed by a homogenization heat treatment under vacuum. Each alloy was then characterized using optical and scanning electron microscopy and differential scanning calorimetry.

A strong link to stoichiometry and transformation temperatures was not evident which indicates that a very limited solubility for off stoichiometry compositions exist within the B2 and B19 structures. The results from this study combined with the results of an advanced thermomechanical processing study conducted by colleagues at the NASA Glenn Research Center were used to select the $\text{Ni}_{25}\text{Ti}_{30}\text{Pt}_{25}$ alloy for more

extensive investigations of their structure, property and processing relationships. For comparison, a Ti-Ni-Pd alloy, namely $Ti_{50}Ni_{30}Pd_{20}$, was selected from literature because it was found to have a maximum in the unconstrained recovery behavior. These materials were extruded characterized by advanced thermomechanical testing by measurement of the baseline mechanical properties and shape memory specific behaviors.

In both alloys the work output reached a maximum as a function of applied stress (biasing load) as did the transformation strain. Through thermomechanical testing it was evident that slip mechanisms were detrimental to the performance of these alloy's performance as actuator materials. In both alloys the resistance to slip under a biasing load in the temperature regions near the transformation temperatures prevented complete recovery thus limiting the work performance of these alloys. A link between the difference in yield strength between the austenite and martensite and the performance under a biasing load was confirmed which is a good indicator in further alloy selection.

CHAPTER 1 INTRODUCTION AND BACKGROUND

Significance

A number of metallic alloys have been shown to exhibit the shape memory effect. Wayman gives a broad definition of shape memory alloy (SMA) which encompasses the bulk of all thermal shape memory alloys. He defines a thermal shape memory alloy as an article that when deformed at a lower temperature will regain its original shape when heated to a higher temperature.¹

Shape memory alloys are used in multiple engineering applications². The most common commercial system is NiTi based SMAs. Applications thus far for NiTi alloys include electrical switches, eyeglass frames, brassiere underwires, cell phone antennas, appliance controllers, temperature sensitive valves, microactuators, and countless medical and dental devices.^{3, 4} In addition, the first large-scale commercial applications for shape memory alloys were made using NiFeTi and NiNbTi alloys with sub-room temperature transformation temperatures, for use as couplings for pipes, tubes, and electrical interconnects.⁵ These applications make use of NiTi alloys near room temperature. The main reason that commercial applications have been limited to near room temperature is that commercial NiTi SMAs have a maximum transformation temperature of about 100°C.

In addition, there are many control and actuation-type applications for materials exhibiting the shape memory effect at higher temperatures. High-temperature shape memory alloys (HTSMA) could be used in the aeronautic, automotive, power generation,

and chemical processing industries. While specific applications have been identified based on some form of a HTSMA, no suitable materials have been developed. As is common in the materials field the development of applications for advanced materials is slightly ahead of the materials development itself, and such is the case for the development of high-temperature shape memory alloys.

Integration of SMA actuators into aeronautic turbomachinery would result in several inherent benefits. Aeronautics clearly emphasizes weight reduction in all stages of engineering. Reduction in the net weight results in sizable gains in fuel efficiency. Additionally, SMA actuators decrease the number of subsystems as compared to standard pneumatic or more common hydraulic and motor-driven actuators, providing further reductions in weight and cost. Figure 1-1 shows the typical weight to power ratios of the more common commercial actuators currently used by the aerospace industry.⁶ Minimizing weight and maximizing power results in a performance index in which SMA actuators are clearly superior.

The design and development of actively controlled SMA devices requires in-depth characterization of the mechanical and shape memory specific properties. Past studies have accounted for compositional effects of transformation temperatures and, in some cases, load-free recovery, yet there is a complete lack of data required for the application of shape memory alloys particularly in actuator-related applications. This study attempts to characterize these properties and correlate them to material composition and microstructure, which in turn can be used to identify possible areas for further alloy and process development.

Background

General Shape Memory Alloy Behavior

SMA's are characterized by a set of temperatures at which a crystallographic structural change begins and ceases. The high-temperature austenite or parent phase is a high symmetry phase usually ordered while the lower temperature martensite phase is a lower symmetry structure which forms from the high symmetry parent phase by a diffusionless shear transformation. The various temperatures at which this transformation begins and ends on heating and cooling are defined as A_s , A_f , M_s and M_f . The austenite start temperature, A_s , is the temperature at which the transformation of the martensite to austenite phase begins on heating. A_f is the temperature at which the transformation is completed and the material is 100% austenite. The martensite start, M_s , and martensite finish, M_f , temperatures are the temperatures at which the transformation occurs on cooling.²

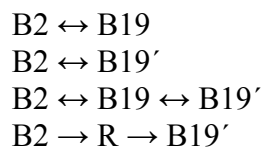
Figure 1-2 is a classical schematic presented by Wayman which shows a material property dependent change as a shape memory alloy is cycled through a thermal hysteresis.¹ A discontinuity in the material properties arises at the onset of the transformation on heating or cooling, which is characteristic of all SMA materials. Throughout the transformation the material exhibits a reversible structural change that results in a measurable change in material properties. This property may be for example specific volume, electrical resistivity, modulus, or other structurally dependent property. The most common test methods for the determination of the transformation temperatures are thermal methods (DSC and DTA) dilatometric methods, and resistive methods. The latter two result in similar hysteresis plots as exemplified in Figure 1-2. While this figure

is idealized it is representative of many of the relevant characteristics of thermal shape memory alloys.

SMA Structural Characteristics

Shape memory alloys exhibit both a thermodynamically and crystallographically reversible transformation. A crystallographically reversible transformation is most likely when the interface between the martensite and austenite is essentially coherent and the parent austenite phase is an ordered compound. The high-temperature austenite phase is a higher-symmetry structure, usually ordered cubic (B2 structure) as in the case of NiTi and NiTi modified alloys. The austenite phase transforms without appreciable long range diffusion into a lower symmetry martensite structure at some lower temperature. Simple cells schematically illustrating the structures common in NiTi above and below the transformation temperatures are shown in Figure 1-3.²

The cubic B2 parent phase in NiTi based SMAs transforms to a number of different martensitic structures. The final structure depends on alloying additions, impurities, and processing history^{7, 8}. The following transformation reactions have been identified.



Each reaction is crystallography reversible with the exception of the $\text{B2} \rightarrow \text{R}$ transformation. The R phase is attained by $\{100\}$ elongation of the B2 structure resulting in a rhombohedral structure.⁹ The B19 phase is an orthorhombic structure which is formed from the B2 parent crystal in several steps, which consist of elongation about the a, b and c axes and shearing of the basal plane in the c direction which is normal to the b direction. The B19' phase is a monoclinic structure formed by additional shearing of the

B19 non-basal plane, which is normal to the a direction in the c direction.¹⁰ The B19' phase is the primary shear structure which appears in binary NiTi leading to the shape memory effect.

The cubic parent phase in NiTi SMA is stable at high temperature (above the A_f). Multiple lattice variants of martensite can form from each parent austenite grain. Each variant will follow a perfectly reversible path back to the parent austenite phase due to the ordered nature of the alloy. If this did not occur, the material would undergo a diffusional transformation in the chemical ordering of the original parent phase's lattice.

In the Pt and Pd modified NiTi SMAs the B19 phase is of primary importance since alloying additions greater than about 10% results in the primary martensitic structure switching from the monoclinic B19' to the orthorhombic B19.¹¹ The B19 and B19' are shear structures of the B2 and therefore exhibit a lower symmetry, with the B19' having the lowest symmetry.¹² The symmetry of the structure is of importance as it is the underlying factor in the determination of the number of equivalent martensitic variants which may form from a parent B2 cubic structure. The B19 has 12 equivalent variants that may form from a parent crystal. This translates to 12 different ways to shear the B2 structure in the formation of the B19. Each equivalent B19 structure may then be sheared along the non-basal plane (001) in the positive and negative c directions to form a B19' martensite which results in 24 equivalent variants.¹³ In general when analyzing shear structures the number of equivalent variants increases as the symmetry of the shear structure decreases. This relationship will be examined in further detail as it relates to the deformation behavior and mechanisms in the shape memory alloys encompassed in this study.

The fundamental theory of martensite formation, which applies to both thermoelastic and thermoplastic transformations, relates a high symmetry parent structure to a variant of the shear structure. Although this theory is applicable to many shear phase transformations for descriptive purposes we will focus on the structures shown in Figure 1-3. Three major deformation steps are required to relate to structures by a purely shear transformation.¹⁴ (1) Primarily there is a Bain distortion which attains its name historically from the distortion observed in the thermoplastic transformation which forms the metastable tetragonal martensite. The Bain distortion is simply the elongation of the parent phase which is shown in Figure 1-3 as the elongations of the a, b and c axis. (2) Secondly a shear deformation must occur in order to preserve the lattice symmetry which combined with the Bain distortion forms the undistorted plane or habit plane. (3) Finally there is a rotation which brings the undistorted plane into the same orientation in both the parent and shear phase.

The accommodation of arbitrary shearing of the lattice (noted as step 2) is a decisive factor defining whether a shear transformation is thermoelastic or thermoplastic. Thermoplastic transformations such as those common in steels are non-reversible and the majority of the transformation shear associated with step 2 is accommodated plastically. That is, there is the formation of non-reversible defects, such as dislocation motion and generation. Thermoelastic transformations on the other hand accommodate the majority of the transformation shear elastically in combination with recoverable mechanisms.

There are three main ways the transformation shear may be accommodated, two of which are reversible. The active shear mechanism depends in part on the mechanical properties of the austenite and martensite as well as the magnitude of the transformation

shear. In both thermoelastic and thermoplastic transformations a significant amount of shear is accommodated elastically which is dependent on the yield strength of the martensite and austenite adjacent to the interface. If the transformation strain results in an interface stress state which exceeds its local yield strength transformation strains are accommodated irreversibly by plastic deformation or slip. Finally, if the shear stress at the interface required to initiate deformation twins is sufficiently low and higher than the yield strength the transformation strain is accommodated by twin formation.

Twin accommodated strain, which is the keystone of shape memory alloys, forms during the transformation along the twin planes in the shear (martensite) phase. It is important to note that the twinning plane is usually a low index plane that is not parallel to the habit plane. Figure 1-3 is a schematic of the nature of a thermoelastic transformation interface between parent and shear phases in which the transformation strain is accommodated by twin formation. The macroscopic shear plane, which separates the cubic and shear structures is dependent on the structural relationships between the martensite and austenite which include Bain shear and rotation. The twinning plane however is based on the symmetry of the shear structure as the deformation twin must only reorient the structure by a concerted movement of atoms uniformly distributed over the volume separated by the twinning plane. The transformation shear along the macroscopic shear plane is partially accommodated by the shear associated with twinning along the twin planes. In thermoelastic transformations the net transformation shear in the martensite is accommodated in part by the elastic deformation of the twinned and untwinned regions and partially by the formation of the deformation twins. If the deformation twins did not occur the stress due to the transformation strain would exceed

the yield strength of the material and thus be accommodated plastically. Twins that form during thermoelastic transformations, in order to accommodate the shear along the macroscopic shear plane, have a twin related crystallographic relationship to one another. As exemplified in Figure 1-4 the sense of the shear associated with a twin must alternate between twinned regions. This criterion for the accommodation of the transformation strain results in the formation of coupled pairs of twins referred to in the phenomenological theory of martensite formation as correspondent variant pairs.¹⁵⁻²⁰

Although many variant pairs may form from an austenite crystal each variant pair is equivalent, thus it is possible for the austenite to transform to a single correspondent variant pair which accommodates the transformation strain by twin formation. This however does not occur in an un-biased (no external stress) sample. What is observed is that austenite transforms into a more or less random orientation distribution of variant pairs. An additional mechanical constraint must be considered to examine the driving force for the observed distribution of variant pairs. The underlying mechanism driving such a distribution stems from the minimization of the macroscopic shape of the bulk material.¹⁵ The transformation product of the austenite in different regions of the crystal transforms in such a manner that there is no macroscopic shape change. This behavior is referred to as self accommodation. Self accommodation is an arrangement of martensitic variants such that the sum of their displacements within the boundary suffers no net displacement. It is possible to place a self accommodating arrangement within an austenitic matrix and not induce any macroscopic strains. Self accommodation is a fundamental characteristic of all thermoelastic transformations as it minimizes interface stresses assuring interface coherence and elastic accommodation of strains. In other

words, if self accommodation did not occur as the interface progresses the stress in the interface would continue to rise and quickly surpass its yield strength resulting in plastic deformation and a loss of coherency. Such is the case in twinned ferritic martensites, where although the twinning process is reversible, the arrangement of twins is such that the interface stresses result in plastic deformation and thus a non-recoverable transformation.

In shape memory alloys the thermoelastic transformation results in a twinned structure. Figure 1-5 shows a simplified representation of two equivalent monoclinic variants separated by a twin boundary. Although more strain could be accommodated by the additional translation associated with the formation of an incoherent twin the interfacial energy of a coherent twin boundary is on average an order of magnitude lower than the energy of an incoherent twin thus additional energy is required to form incoherent twins.¹⁶ As a result the formation of coherent twin interfaces between martensite variants is thermodynamically favorable and additional energy is required to form incoherent twins.

Figure 1-6 are TEM micrographs of a binary NiTi shape memory alloy.² This figure shows the differences between a twinless martensitic structure (6.a.) and a finely twinned structure (6.b.). Both structures are monoclinic differing only by the presence of a fine distribution of deformation twins that form during the phase transformation. The detwinned structure shown in micrograph 5.a. resulted from deformation by detwinning of the martensite. Another fundamental aspect of shape memory alloys is deformation of the martensitic structure through detwinning.

A completely reversible structural transformation requires that the parent-martensite interface be glissile in the forward and reverse directions. In addition the thermal hysteresis must be small. Ling and Owen have shown that sessile dislocation loops and other defects in the matrix facilitate the movement of the interface.¹⁷ Furthermore these sessile defects increase the plastic flow stress of the matrix hence making the accommodation of strain by slip more difficult. Mechanically the matrix is effectively strengthened and the energy required to move the parent martensite interface is lowered. This has been correlated to NiTi based SMAs as well as other SMA systems. The density of these defects increases with thermal cycling up to a limit resulting in a decrease in transformation temperatures with increased thermal cycles. Decreasing transformation temperatures with thermal cycling has been observed experimentally as shown in Figure 1-7.¹⁸

SMA Mechanical Behavior

Metals that exhibit a thermal shape memory effect deform through twin boundary motion. Recoverable deformation of the martensite by twinning reactions must occur at stresses lower than those for non-crystallographically reversible reactions. Non-crystallographically reversible reactions include dislocation generation and motion. Structurally, twins are formed in the martensite during the forward reaction separating equivalent variants. Multiple martensite variant formation is driven by the minimization of the net transformational stresses. Hence, twins are present in the microstructure after transformation; therefore, nucleation by an applied shear is not necessary in contrast to standard deformation twinning. Deformation occurs by the growth of variants most favorably aligned with the largest principle shear component or Schmidt factor at the expense of those with the lowest component. This mechanism is commonly referred to

as detwinning. Deformation by this mechanism decreases the number of twins in the alloy. This is schematically shown in Figure 1-8. The arrow indicates twin planes in this schematic. An aligned shear results in the twin boundary motion in the direction normal to the shear and the growth of a corresponding variant. Upon fully detwinning the alloy, the material theoretically exists as a single variant although the extent of detwinning depends on crystal structure and the associated number of equivalent variants as well as the existing variant distribution prior to deformation.

The typical macroscopic mechanical behavior of a shape memory alloy is represented in Figure 1-9. This figure is a schematic of the general stress strain curves exhibited in these systems below the M_f temperature. It should be noted that the alloy's composition, and mechanical and thermal history may change this curve. It is also possible to have multiple active deformation mechanisms, which will affect the work hardening rate during the detwinning region of this curve. This figure represents the ideal case for the shape memory effect.

The initial portion of the stress strain curve is attributed to elastic deformation of the undeformed martensite. Upon reaching a critical stress, detwinning of the martensite begins. The detwinning stress is independent of twin density and therefore a region in the stress strain curve exists in which the stress required to deform the material is independent of strain. A critical level is reached at the point where favorably oriented variants are most prevalent in the microstructure and thus reactants of the detwinning reactions that supply the growth of the favorably oriented twins are consumed. At this point twins with similar Schmidt factors may impede on each other. The result is an increase in stress-strain relationship that is attributed to elastically deforming the

detwinned martensite. A second yield point is evident at which the critical stress for slip is reached. Non-reversible deformation mechanisms are active in this region thus the strains are not recoverable by shape memory processes.

Figure 1-10 is a series of hypothetical stress-strain curves that graphically represent the three distinct deformation behaviors exemplified by SMAs and the temperatures at which they may be active.¹⁹ At temperatures above the A_f the shape memory alloy is austenitic and deformation occurs by elastic loading of the austenite followed by slip. Below the M_f temperature the shape memory alloy is fully martensitic and deformation occurs by the detwinning mechanisms described above. SMAs demonstrate an extraordinary superelastic effect which occurs when the material is deformed above the M_s temperature and below the M_d temperature (Figure 1-10). The M_d temperature is defined as the temperature at which mechanical stresses can induce a martensitic transformation. Subsequent removal of the external stress results in a non diffusional reversion to the thermodynamically stable parent phase. Elastic strains attainable in NiTi shape memory alloys are 20X those of carbon spring steels.

Thermoelastic Shear Transformations

The thermodynamics of shape memory alloys and the relevant shear transformations is a complex subject, which involves a competition between the chemical and non-chemical driving forces. We have stated that martensite forms from the parent phase by a purely diffusionless shear transformation. The transformation front progresses by shear atomic motions and the interface between the martensite and parent phase is coherent. Structurally the martensite results in a net shape change of each equivalent variant. As in the case of NiTi addressed previously a cubic structure transforms to a monoclinic or orthorhombic. This net shape change results in an accommodation strain.

The local strain around each variant can be accommodated plastically, elastically or as a mixture of both. This phenomena has been reviewed and the key thermodynamic parameters identified by Reed and Abbaschian.²⁰

Table 1 was compiled from publications [1,16,28]. The listed characteristics are common to SMA systems. The structural and mechanical characteristics already have been briefly addressed. In addition to and as a result of these structural characteristics a specific set of thermodynamic properties arise.

Table 1-1 Several characteristics common to metallic thermal SMAs.

Structural characteristics of SMAs¹

- Ordered parent -> ordered martensite
- Martensitic transformation is thermoelastic
- Martensite is crystallographically reversible

Thermodynamic characteristics defined by Dunne and Wayman²¹

- Small chemical driving force at Ms
- Small transformational volume and shape change
- High flow stress parent matrix

Additional mechanical characteristics defined by Ling and Owen¹⁶

- Parent-martensite interface must be glissile in both transformation directions
- Premartensite elastic softening

A fundamental condition for the shape memory effect is that the transformation must occur reversibly. Accommodation of the transformational strains adjacent to the interface could be plastic, elastic, or a mixture of both. In the case where the majority of the strain is accommodated elastically the interface is able to move in both directions referred to as a thermoelastic transformation. As a result the chemical driving force required to drive the reaction is small. This is the case in alloys exhibiting the shape memory effect, which are more precisely defined as thermoelastic transformations.

In thermoplastic transformations the transformation strain is accommodated plastically due to a low flow stress in the parent phase and a large transformational strain.

In this case, the transformations on the forward and reverse direction occur at much higher chemical driving forces through the nucleation and rapid growth of the martensite. Typically individual shear plates are nucleated at defects and grow irreversibly. Subsequent thermal cycles result in new plates nucleating rather than reversible interface movement. A classic instance of such a case is the martensitic transformation of carbon steels where the thermal hysteresis is large and most of the transformational strains are accommodated plastically.

Ortin and Planes elegantly treated the thermodynamics of thermoelastic effects and systematically defined conditions for a thermoelastic energy balance.²² Thermoelastic transformations are driven by the chemical free energy. At equilibrium it would be expected that the transformation occurs when the chemical free energy of the parent phase is a small amount larger than that of the shear phase. This however has been shown not to be the case. In actuality, the chemical driving force in thermoelastic transformations are opposed by non-chemical forces, thus the equilibrium transformation occurs when these forces are nearly equal. Following the notation and approach presented by Ortin and planes, thermodynamic equilibrium is represented by the following equation.

$$\Delta G_{p..m} = -\Delta G_{ch} + \Delta G_{nch} = 0$$

$G_{p..m}$ is the molar free energy of transformation, G_{ch} is the molar chemical free energy and G_{nch} is the molar non-chemical energy. At equilibrium the molar free energy of transformation is equal to zero thus the chemical contributions are equal to the non-chemical contributions.

The non-chemical contributions consist of several factors, the most prominent are the elastic free energy and work done against frictional forces.

$$\Delta G_{\text{nch}} = \Delta G_{\text{el}} + E_{\text{friction}}$$

$$\Delta G_{\text{ch}} = G_{\text{nch}}$$

$$\Delta G_{\text{ch}} = \Delta G_{\text{el}} + E_{\text{friction}}$$

The elastic and frictional terms consist of several components. It was stated that a condition for thermoelastic transformations is that the majority of the transformational strains are accommodated for elastically. Therefore adjacent to each interface we have a finite amount of stored elastic energy. In addition there exists an interfacial energy associated with the parent martensite interface as well as the interfaces between variants (twin boundaries). Both contributions are reversible therefore they have been grouped into the elastic term even though the interfacial energy is not truly an elastic contribution. This is in line with the convention set forth by Ortin and Planes.

Frictional energy losses are non-reversible losses primarily due to interface movement. This term may be treated as irreversible work done on the system. Three significant parts have been identified by Olsen and Cohen.^{23, 24} These include 1) frictional stresses required to move interfaces 2) irreversible free energy related to defects induced during the transformation 3) frictional stresses required to move interfaces.

It is important to note that if all or most of the accommodation occurs plastically the elastic term will be very small and the frictional energy loss term will be the main opposing energy to the chemical driving force. As a result a large non-reversible hysteresis will be evident as is the case in carbon steels as mentioned earlier.

The underlying mechanisms and thermodynamics which control general behavior of shape memory alloys have been reviewed. Principally the structural relationships

between the parent in shear phases result in thermomechanical properties unique to shape memory alloys. Additionally, driving forces and the relating thermodynamic for thermoelastic transformations have been briefly discussed and compared to thermoplastic transformations. A persistent problem that will be discussed in subsequent chapters points out that plastic accommodations by non-recoverable processes hinder the sought after characteristics of shape memory alloys, principally the materials ability to do work. Essentially under certain conditions these shape memory alloys start to behave more like thermoplastic materials where a significant portion of the transformation strain is accommodated plastically. The combination of structure, mechanical properties and thermodynamics are used as tools to understand deformation and propose possible deformation mechanisms while identify possible target area for future alloy improvement.

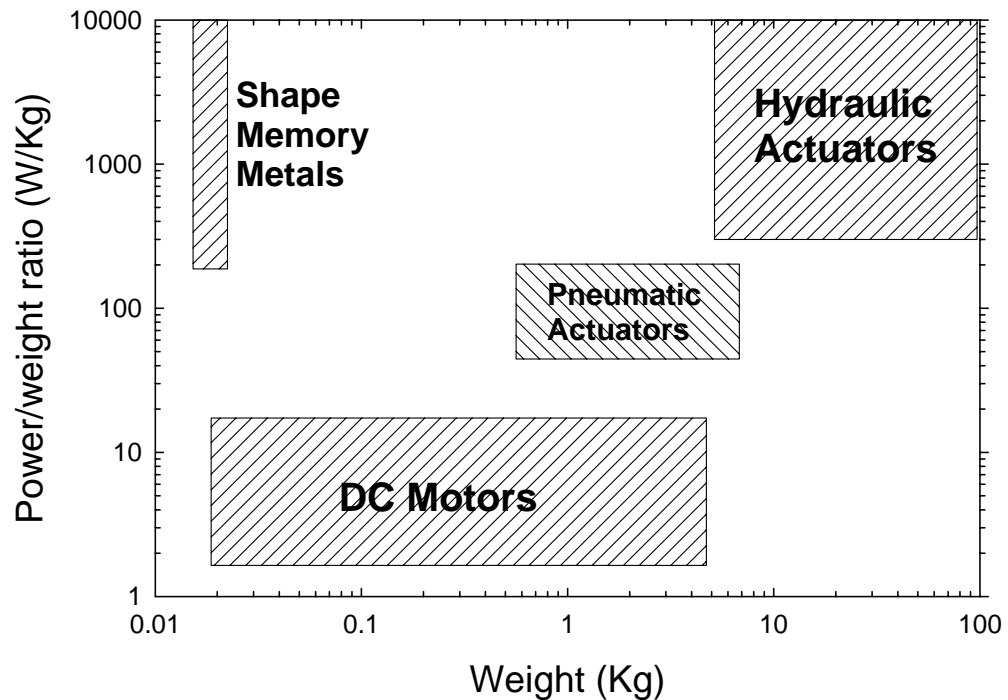


Figure 1-1 Power-to-weight ratio versus weight diagram for common actuator types currently used in aeronautics.⁶

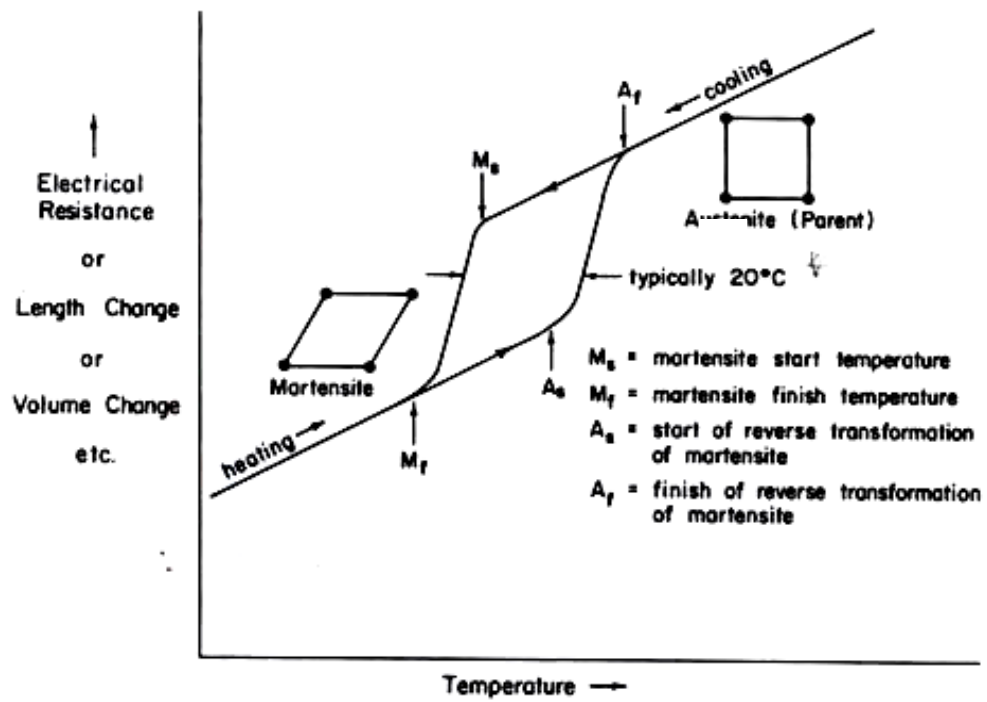


Figure 1-2 Idealized plot of a property change vs. temperature.¹

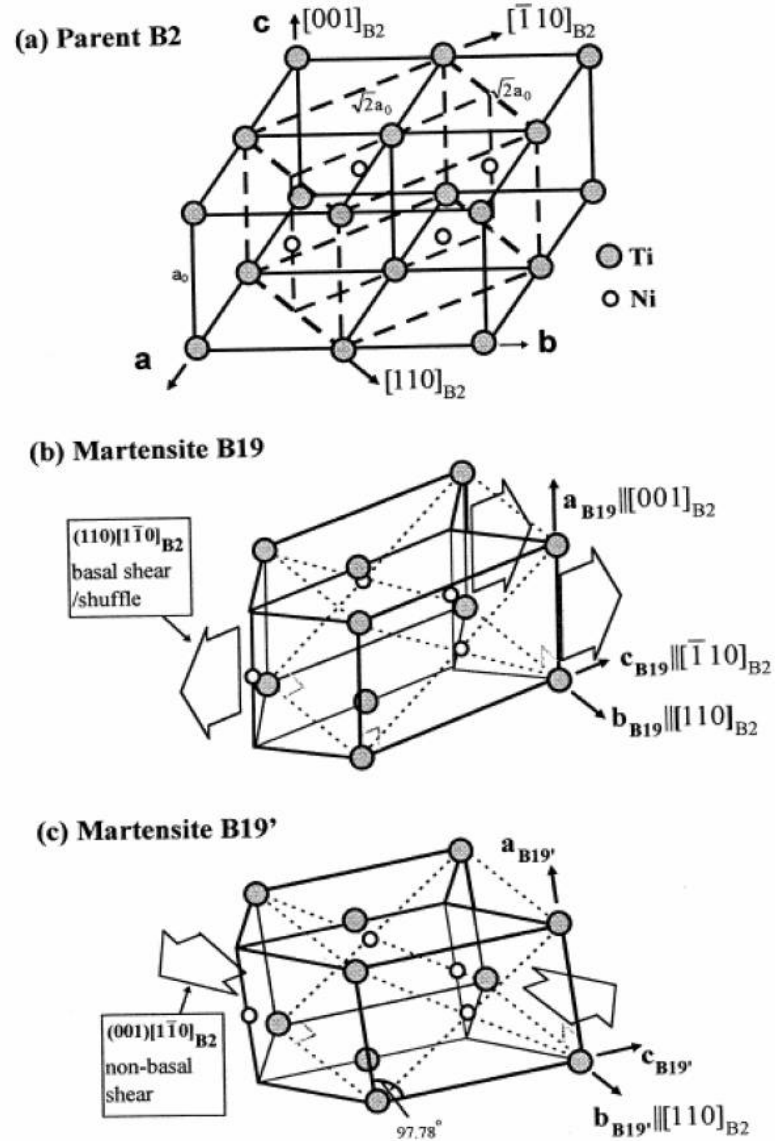


Figure 1-3 Structure of the parent phase (austenite) and shear phases (B19 and B19' martensite).²

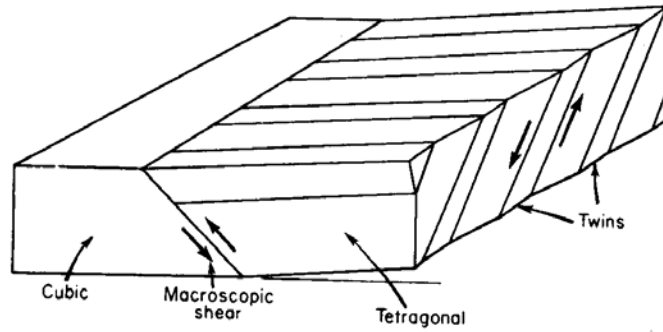


Figure 1-4 Thermoelastic transformation and twin accommodated transformation strain.¹⁴

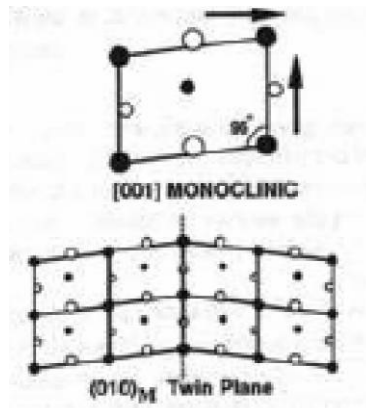


Figure 1-5 Two-dimensional lattice schematic of monoclinic structures³.

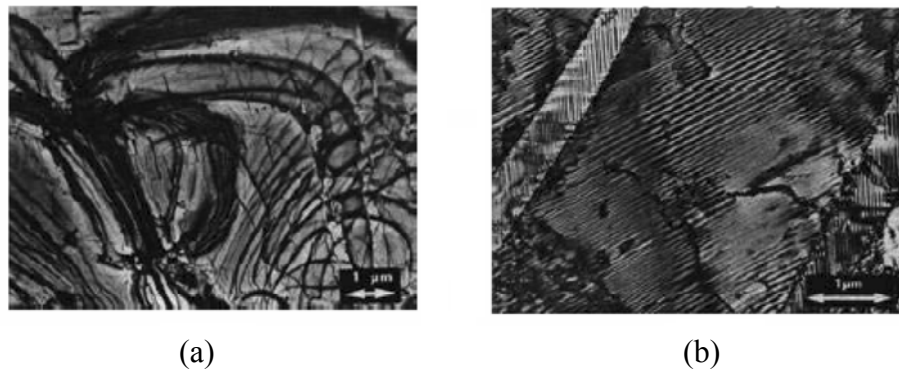


Figure 1-6 TEM micrographs of twinned and untwinned monoclinic martensite.³

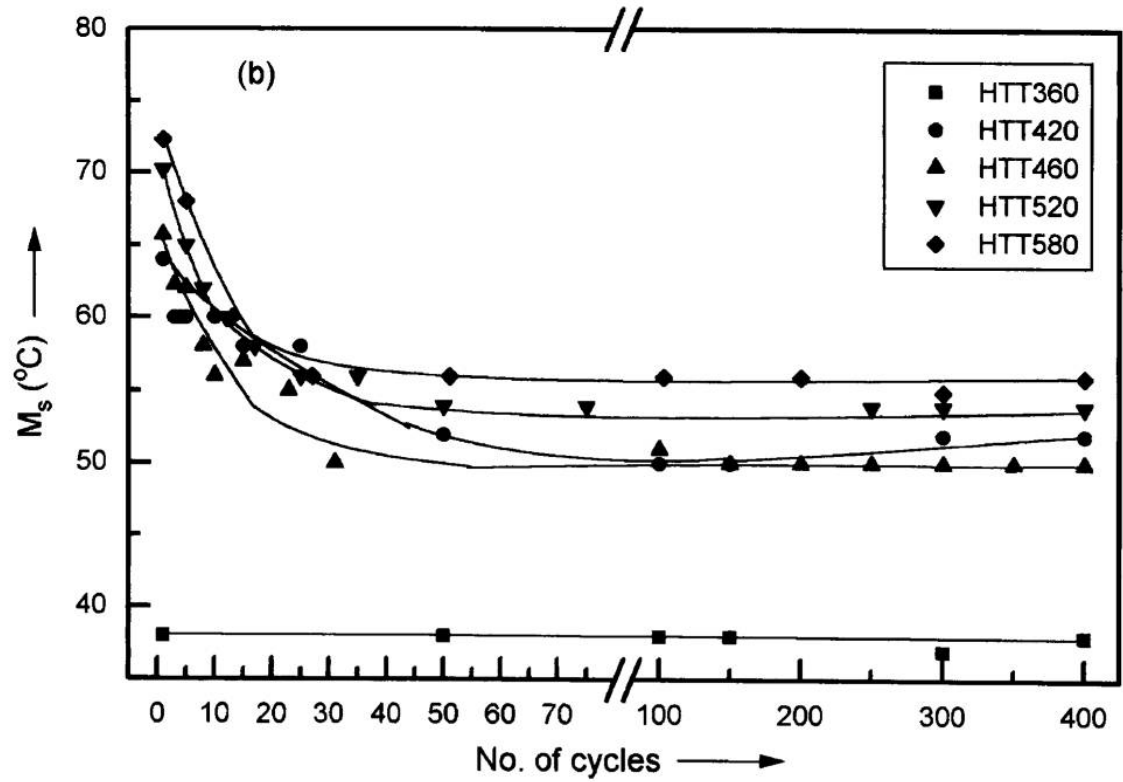


Figure 1-7 Effects of thermal cycling through the hysteresis on the transformation temperatures of several NiTi based shape memory alloys.¹⁸

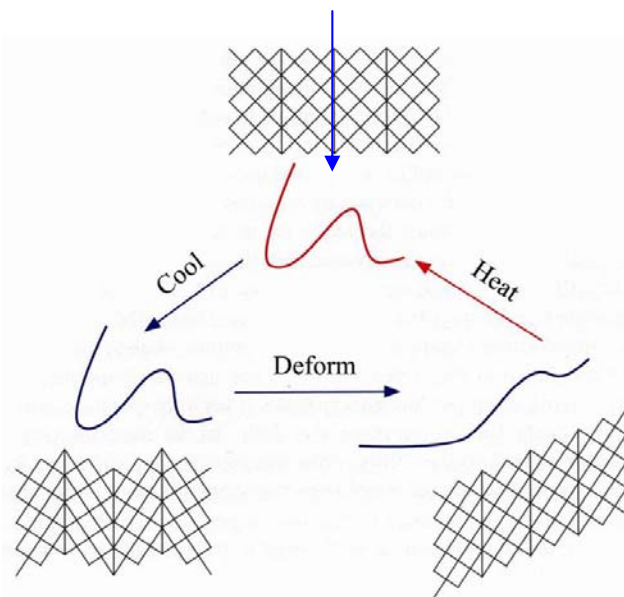


Figure 1-8 Deformation and shape recovery by detwinning (twins marked with arrows).¹⁵

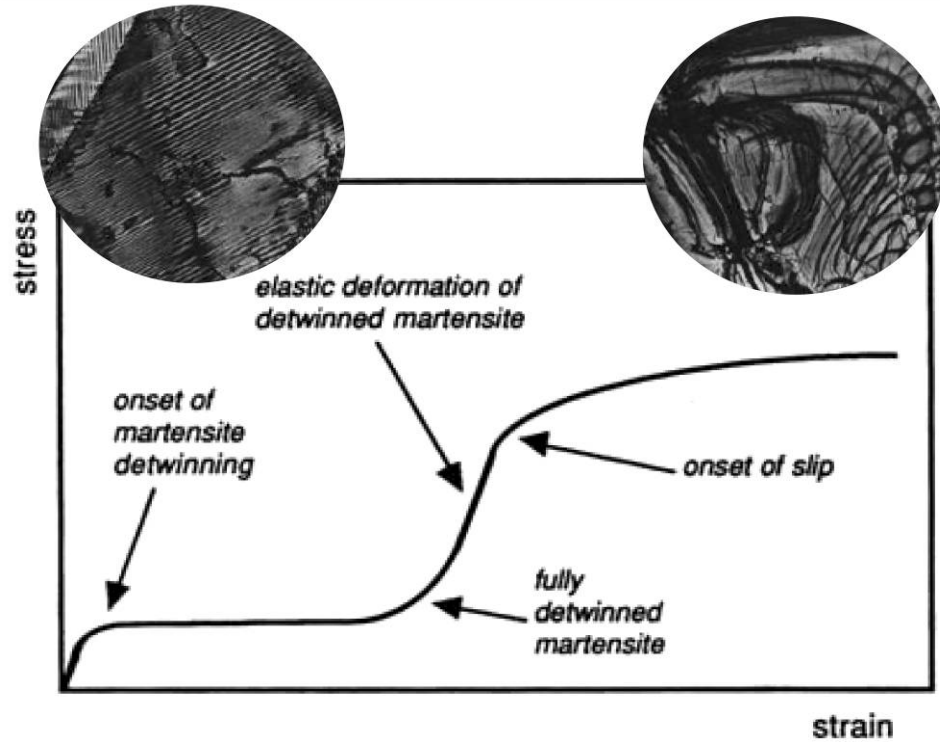


Figure 1-9 Isothermal stress strain behavior of a typical SMA strained in the fully martensitic state.³

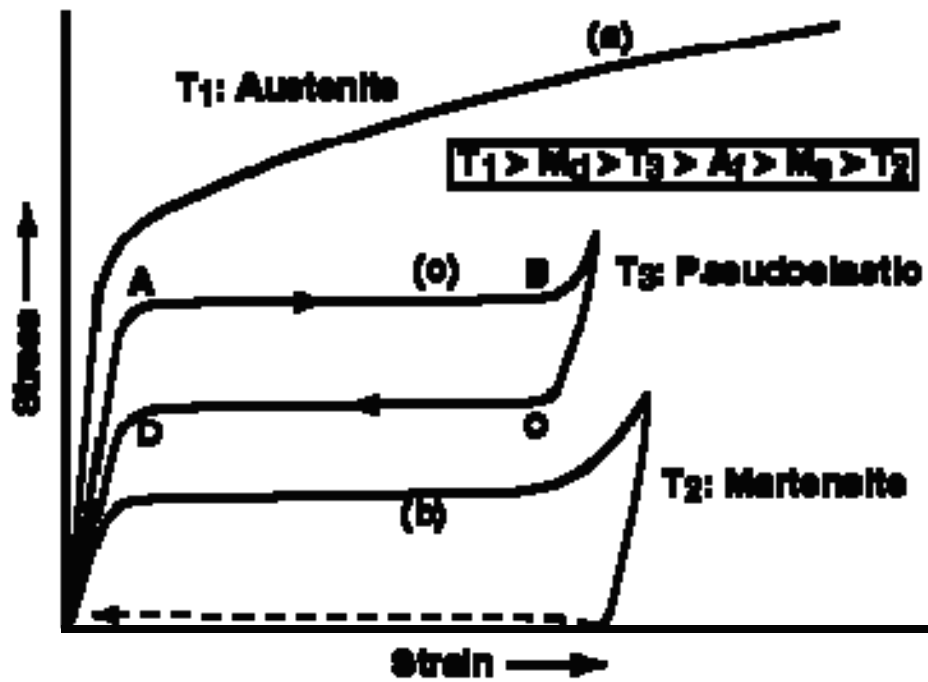


Figure 1-10 Stress strain behavior showing the three main deformation regimes active in SMAs.³¹

CHAPTER 2 MATERIALS PROCESSING AND PROCEDURES

Melting Procedures

Arc Melting

The experimental portion of the alloy development phase of this study was initiated with a cursory examination of a series of over twenty alloys along and on either side of a line of constant stoichiometry (constant Ti atomic fraction of 50%) between TiNi and TiPt in order to survey the basic properties of the Ni-Ti-Pt system in a region where the potential for shape memory behavior is likely. The experimental alloys were produced by non-consumable-arc melting of high purity starting components (99.95% purity Ti, 99.995% purity Pt, 99.98% purity Ni) using a water-cooled copper crucible in a high-purity argon atmosphere. Due to the substantial density differences and melting points between the starting materials, it was difficult to melt the platinum completely in one step. Consequently, the buttons were turned over and remelted 4-6 times in an attempt to insure homogeneity.

Arc Melt Machining

Sectioning for thermal, microstructural, and hardness measurements was performed by wire EDM (electrical discharge machining). For example, 10mm length by 5 mm diameter cylinders were EDM'd for thermal analysis from the center of the arc melted buttons. Planar specimens for microstructural and hardness were fabricated by transversely sectioning the arc-melted button followed by pressure mounting into phenolic bound thermosetting polymers mounts. The exposed planar section was then

ground using SiC papers and polished using diamond suspensions using standard metallographic preparation techniques, yielding a highly polished, low residual stress surface.

Induction Melting

The experimental alloy of a target composition of $\text{Ni}_{19.5}\text{Pd}_{30}\text{Ti}_{50.5}$ was produced by vacuum, induction melting of high purity starting components (99.95 Ti, 99.995Pd, 99.98Ni) in a graphite crucible, which is tilt poured into a 25.4 mm diameter by 102 mm in length copper mold. The mass of each ingot is approximately 450 grams including the hot top, which feeds the casting during the shrinking associated with solidification (Figure 2-1). Induction melting was chosen over arc melting in order to circumvent problems inherent to arc melting materials with large density difference as in the case of Ti 4.506 g/cm^3 and Pd 12.023 g/cm^3 or Ni 8.908 g/cm^3 . Induction melting also induces a mixing action in the melt which assures a homogenous melt. Graphite does introduce a limited amount (approximately 0.5 at.%) of carbon during the melting process resulting in the formation of carbides with the excess off-stoichiometry Ti.

Homogenization

Each induction melted ingot or arc melted button was simultaneously sealed in a vacuum furnace and homogenized at $1050 \text{ }^\circ\text{C}$ for 72 h. This was followed by a furnace cool as shown graphically in step 1 of

Figure 2-2. This figure summarized the thermal history of the extruded material. The arc melted material is homogenized (step 1) and as it is not extruded or mechanically machined a stress relief heat treatment is not required and stabilization of the transformation temperatures is accomplished by multiple thermal cycles during hysteresis measurements. The homogenization heat treatment is employed in order to remove fine

atomic segregation and insure full reaction to form the ordered structures with a minimum amount of ordering defect and resulting point defects. Uniformity in the hot zone is assured through multiple thermocouples and independent zone control through several calibrated temperature controllers and gradual temperature ramp rates.

Extrusion

After homogenization the ingots were individually sealed in steel extrusion cans. The ingot was placed into the extrusion can and a vacuum cap was sealed by tungsten inert welding. The vacuum cap specifies a cylindrical cap with a fitted mild steel vacuum tube. Through this tube the sealed cavity was evacuated following by a crimping and spot welding operation. At this point the canned ingot is ready for extrusion. Following the canning operation the sealed ingots were extruded with a 7:1 reduction ratio at 900°C in a hydraulic press. A schematic of the extrusion operation is given in Figure 2-3. Prior work at the NASA Glenn Research Center has demonstrated the feasibility of this technique and determined these are optimal conditions for the thermo-mechanical processing of comparable HTSMAs.

The extrusions were X-rayed in order to have an accurate determination of the location of SMA core's start and finish position in the steel covered rod and the excess ends of the extrusion removed by abrasive cutting. The extrusion rods were then cut into various lengths.

Compressive samples were fabricated by wire EDM methods and centerless grinding, yielding 5 mm diameter by 10 long samples (Figure 2-4). Additionally 1 X 4 mm rectangular samples, x mm in length were sectioned by wire EDM from the core of the extruded bars for resistivity measurements. Finally, a section of the extrusion is

removed for ICPS (spell out) by which the bulk alloy composition was measured and documented.

Tensile samples were fabricated by turning, using a computer controlled lathe (C&C). The canned extrusion was sectioned by EDM into 50.80 mm sections, which were individually center punched. The cut sections were loaded with the extrusion can still lining the sample into the C&C lathe. The entire machining procedure was performed in a cutting mode which completely excludes costly grinding operations. Successive cutting passes were made to yield threaded 17.4 mm long by 3.81 mm diameter gauge sections (Figure 2-4). A summary of all the sample preparation steps and methods are graphically represented in the flow diagram shown in Figure 2-5.

Stress Relief Heat Treatment

To complete the sample preparation phase, all samples are given a stress relief heat treatment at the A_f plus 200 °C for 1 hour followed by a furnace cool. The function of this heat treatment is to relieve any residual stresses on the surface of the samples resulting from the extensive machining operations during the fabrication stage. Structurally this heat treatment is performed in the austenite phase thus allowing for recovery in the high symmetry phase. This heat treatment was optimized based temperature resistivity measurements.

Characterization Procedures

Dynamic Modulus

A dynamic modulus testing apparatus facilitated the determination of the modulus of elasticity as a function of temperature for each phase. A 34 mm bar was machined and fixed with an electrodynamic vibrator at one end a piezoelectric transducer at the other end. By locating the resonance frequency as a function of temperature it was possible to

calculate the dynamic modulus as a function of temperature during heating. The sample was heated at 10 °C/min in a convection furnace to a maximum temperature of 800 °C.

A detailed description of the melting, heat treatments, extrusion, and final machining of thermo-mechanical Ni_{19.5}Pd₃₀Ti_{50.5} samples is outlined here. As these alloys behave in a similar manner and in order to allow for direct comparison between the Pt and Pd modified alloys, the processing scheme was intentionally followed as closely for both materials. The Pt modified alloy Ni_{24.5}Pt₂₅Ti_{50.5} selected for this study was processed in parallel following a comparable processing scheme as the Pd modified alloy described above and as outlined in Figure 2-5. The only significant differences is that since the austenite has a lower flow stress in the Pd modified alloy the extrusion pressure is slightly lower. All melting and processing steps are comparable.

Compositional Analysis

The bulk alloy compositions were determined by inductively coupled plasma spectroscopy and the interstitial impurity concentrations were determined using standard LECO O/N and C/S determinators. For this analysis, samples were prepared by first cutting buttons into smaller sections of approximately 100mg followed by a petroleum ether rinse in order to remove any surface contamination. These sections were then air dried, reweighed and placed in a Teflon digestion vessel. 3 mL HCl, 1 mL HNO₃, and 1 mL HF (all concentrated and trace metal grade) were added to the vessel which was then placed in a block digester at 100-130 °C until dissolution was complete (generally 1-2 hours). Finally, the dissolved sample was transferred to a 100 mL volumetric flask for ICP analysis.

The ICP solutions were analyzed for alloying elements and impurities using the Varian Vista-Pro Inductively Coupled Plasma (ICP) Emission Spectrometer. The composition of the ingots was measured by inductively coupled plasma spectroscopy post heat treatment and thermo-mechanical processing to insure measurement of any additional contamination that may have been picked up during these procedures. A schematic of the instrument is shown in

Figure 2-6.³² In this process, the solution is injected by capillary action into an argon plasma. The sample is ionized and excited by the plasma, which results in each element emitting a characteristic wavelength. The emitted photons are allowed to pass into the system through the entrance slit and are diffracted by a fixed grating Echelle polychromator, and finally the intensity of each wavelength is measured using a CCD (charge coupled device) detector. The detector is capable of simultaneously detecting up to 73 different elements in the range of 167 - 785 nm.

Several emission lines are selected for quantitative analysis of each element by extrapolation of measurements using calibrated NIST-traceable solution standards. The emission intensity at each wavelength is proportional to the concentration of the element present in the solution, which is determined from extrapolation of the calibration curves. The mean intensity over several peaks is used in calculating the reported concentration of each element.

Nitrogen, Oxygen, Carbon and Sulfur Analysis

Again, samples of approximately 100mg were analyzed for oxygen and nitrogen using the Leco TC-436 Nitrogen/Oxygen Determinator. In this technique, a graphite crucible is baked out by a high current in order to expel any gas trapped within the crucible. The sample is then placed into the crucible and the chamber is evacuated.

Resistive heating raises the crucible and sample temperature thus causing the sample to expel any nitrogen and oxygen. A gas solid reaction occurs between the oxygen and the carbon crucible which yields CO. Subsequently the CO is passed through a rare earth copper oxide reactant producing CO₂ which is measured by an IR cell. The CO₂ is separated from the remaining gas by ascarite absorption which is a powerful CO₂ absorber. Finally, nitrogen is measured by a thermal conductivity cell which measures the temperature difference between a heat source and a thermocouple which is protected from radiative heating.

Samples parallel to those used for O/N analysis were analyzed for carbon and sulfur using the Leco CS-444LS Carbon/Sulfur Determinator by the combustion instrumental method. In this method, the sample is combusted in the presence of oxygen yielding carbon dioxide and sulfur dioxide. The amounts of CO₂ and SO₂ are determined by measuring the absorption of specific IR wavelengths, which are proportional to the partial pressures of these gasses.

Thermal Analysis

Transformation temperatures were determined by differential scanning calorimetry (DSC) for low to intermediate temperature analyses and differential thermal analysis (DTA) was used for intermediate to high temperature transformations. DSC Data analysis was performed using the TA Universal Analysis 2000 Software package. Each alloy was cycled through two full thermal hysteresis cycles (approximately Af +100 °C to Ms-100 °C) assuring the reproducibility of the thermoelastic transformations. It was experimentally determined that in these arc melted and homogenized samples, the transformation temperatures stabilize after two cycles and therefore remain constant with

subsequent cycles. The acquired data is formatted as the temperature dependent heat flow as exemplified in Figure 2-7. A combination of techniques was employed in order to circumvent temperature limitations of each instrument by maintaining the measurements within the designed temperature intervals thus assuring high precision measurements. For both techniques, a heating and cooling rate of 10 °C per min was used.

DSC and DTA are common techniques used in determining the thermal properties of materials with a high degree of precision. Although both are differential methods, the DSC in contrast to the DTA calculates heat flow directly during heating, cooling or isothermal holds by measuring the amount of energy required to maintain the specified temperature, while the DTA measures differences in temperature between a sample and a reference while heating both at a constant rate. Therefore, the main differences between the data acquired from a DTA and that of the DSC is that the determination of heat flow requires calculations from standards of known heat capacities similar to the unknown sample and the sample heating rate is not as precisely controlled.

As a consequence of these differences, it is generally considered difficult to directly compare the thermodynamic properties measured without stringent calibration. The application of the DSC and DTA in the current SMA study is solely for the determination of the transformation temperatures without focusing on the heat capacities or the magnitude of the transformation enthalpy.

Characterization of the transformation temperatures through DSC and DTA measurements were made by the extrapolated onset method by which the transformation temperatures are recorded as the intersection of the base line and the best fit of the linear

portions of the increasing and decreasing regions of the exothermic or endothermic peaks in the lambda type curve.³³ A characteristic of the extrapolated onset method is that the relative amplitudes of the heats of transformation as a function of temperature determines the transformation start and stop temperatures independent of the absolute or actual transformation enthalpy, facilitating the comparison of transformation temperature measurements made on a DSC and DTA.

Thermoelastic transformations, which are characteristic of metallic shape memory alloys, involve displacive shear transformations. This type of transformation exhibits a strong temperature and stress dependence and relatively fast transformation kinetics. Fast transformation kinetics result in the reaction reaching its temperature and stress-dependent equilibrium rapidly in contrast to diffusional transformations, which require extended times. As a result, thermoelastic transformation temperatures are not highly time or more specifically heating rate dependent unlike diffusional transformations. Consequently, although the heating or cooling rate of a thermoelastic sample might vary slightly in a DTA where only the hot zone's temperature is precisely controlled, the kinetics of the reaction are so fast that the dependence of the transformation temperature on these slight variations are insignificant. Therefore it is feasible to compare the transformation temperature measurements of thermoelastic transformations in a DSC and DTA.

Microstructural and Semi-Quantitative Compositional Analysis

The sectioned and polished alloys were examined using a JEOL 6400 scanning electron microscope (SEM) using backscattered electron (BSE) mode. An annular detector was used in order to maximize the signal. The sample surfaces were kept normal to the 15 KeV beam and parallel to the detector's exposed face. This configuration

maximizes phase contrast and minimizes any topographical effects by measuring the sum of the back scattered electrons around a 360° ring perpendicular to the electron beam and normal to the sample's surface. All comparable imaging was done at the same magnification in order to allow for simple comparisons. Semi-quantitative ZAF corrected EDS analysis of the various phases was performed using the $\text{NiK}\alpha$, $\text{TiK}\alpha$, and $\text{PtM}\alpha$ lines.

Dilatometry Measurements

The transformation temperatures were also determined by measuring the strain-temperature response of the material under essentially zero load (stress free condition) using a differential thermal dilatometer. This instrument compares the measured change in length of a test specimen to that of a standard as a function of temperature thus allowing for correction for any thermal expansion in the apparatus itself. In this measurement, the furnace heating rate is controlled at 10°C per minute and the sample temperature is measured directly by thermocouple contact. A differential thermal dilatometer is used to measure the transformation strain in the longitudinal direction. Several cycles through the transformation hysteresis are performed until the transformation strain vs. temperature relationship stabilizes. This technique is used to determine the transformation strains associated with the SMA reaction as well as the thermal expansion coefficient of the parent and austenite phases.

Resistivity Measurements

Sample instrumentation

1 X 4 X 20 mm rectangular samples were sectioned by wire EDM from the extruded bars described in a previous section and prepared for electrical resistivity measurements. The surface was cleaned by light polishing prior to the stress relief heat

treatment. The sample was instrumented with a four point probe and a K-type thermocouple as shown schematically in Figure 2-8. Two pairs of Pt or Ni drawn wires were spot welded to the sample functioning as the voltage sensing and current excitation leads. The current excitation leads were spot welded near the ends of the sample while the voltage sensing leads were spot welded further in from the ends between the two current excitation leads. The sample dimensions (cross-sectional area) and distance between the voltage sensing leads was measured using a vernier caliper.

Resistivity apparatus

Test specimens were heated through a thermal hysteresis in an ATS 3200 series split tube furnace at 10 °C/min followed by a subsequent furnace cool in an ambient atmosphere. Furnace control was achieved via a Eurotherm programmable PID (proportional integrating differentiating) temperature controller. Thermal cycling through a thermal hysteresis was achieved by running a 3 leg program consisting of a ramp of 10°C/min to the final temperature followed by a step command which turns off the power to the furnace until the minimum specified temperature was attained and finally an end command which signals the end of a thermal cycle. The independent programmable control loop in the resistivity apparatus is the call for power from the furnace controller. Alternatively the resistivity apparatus is capable of sending control commands to the furnace controller allowing for external furnace control and integration with moving hot zone cyclic furnaces.

The stress-dependent transformation temperatures and resulting electrical properties of a material were determined by high-resolution resistivity measurements. A virtual digital instrument that acquires high-resolution, real time, temperature versus

resistance profiles of materials was developed for this purpose. Additional integration of this instrument with an MTS uniaxial testing apparatus facilitated the direct measurement of stress-induced transformations and the effects of external stresses on transformation temperatures. Two operational modes, level crossing acquisition or timed acquisition, depending on the function of the measurement (cyclic thermal measurements or stress, strain, resistivity profiles) were employed. This instrument was designed to be automated such that, once configured, it would allow for the unattended measurement of many cycles.

The components of the measurement apparatus include a PC, National Instrument DAQ (data acquisition card) and a NI SCXI (signal conditioning) chassis fitted with an analog signal amplification and filtering card. Current excitation was supplied by an Agilent power supply with internal shunt resistors while the calibrated National Instruments DAQ system and analog signal conditioner were used to measure voltage signals and linearize the thermocouple. The digitized signals were used to calculate real time resistance values for each specimen, which in turn allows for the calculation of the samples resistivity, based on sample dimensions. In addition, external calibrated devices have been integrated facilitating the calibration of the apparatus and the documentation of calibration prior to each measurement. In principle, it was required by design criteria that the system measure accurate absolute values of resistivity as well as resolve transformation temperatures thus necessitating external calibrations. Finally, external digital and analog channels have been programmed into the instrument so that it could function as the controller for a cyclic furnace or comparable device.

Due to the high conductivity of the SMA alloys, the resulting voltages measured across the sample were on the order of fractions of a mV. Signals of this magnitude are very susceptible to noise thus necessitating several signal conditioning processes. Hardware and software low pass filters have been employed in this system in order to allow for measurements to take place while the sample was under an inductive load as well as filtering out cyclic noises above 4 Hz which may enter the signal via the extensive connecting wires or at the sample itself. Figure 2-9 shows the in-situ filter response for a sample that was heated by an inductive field. The signal in this type of instrument may be separated into two main components. The primary component is the DC signal of interest which results from the interaction of the material with the excitation source and a superimposed AC component which is caused by induction heating of other external sources. The lower blue graph shows the unfiltered signal as measured by a documenting oscilloscope while the upper curve shows the filtered response which demonstrated the efficiency of the filter system at isolating the DC component of the signal..

A secondary benefit of using a powerful precession external power supply is the capability of resistively heating samples by driving high current densities along their length. Such an experiment may be used to monitor the power requirements of SMAs and SMA actuators. Routines for monitoring these parameters have been written into the instrument. The processed data is sample temperature, power, current, voltage across the sample and resistance. Again, these are all monitored real time so that this data can be used to characterize the power requirements of SMAs in several geometries. It is possible to use this routine to characterize model and real SMA actuators.

As mentioned previously, the instrument was designed to be automated and acquire data in two modes (level crossing acquisition or timed acquisition). The level acquisition mode is used for the generation of resistivity vs. temperature profiles. Level acquisition refers to the monitoring of a trigger signal and acquiring a new set of data points or data object when the trigger is crossed. In the case of the resistivity apparatus, the temperature signal is defined as the trigger which implies that when the absolute value of the difference between the transient or trigger temperature and the previous trigger value, is greater than a specified amount a new data point (temperature and resistance) is recorded. Additionally, detection of a complete thermal hysteresis is required in order to allow the separation of data into groups forming a complete hysteresis defined as a heat and cool cycle. This again was accomplished by level crossing triggers where the algorithm finds a maximum followed by a minimum temperature before triggering a new hysteresis command, which records the data and clears the dynamic memory. Timed acquisition implemented in the integration of stress, strain, and resistivity measurements records data objects at predefined clock intervals.

Post processing measurements of the transformation start and finish temperatures for the forward and reverse shape memory reactions was also automated, thus facilitating the measurement of many cycles in a typical high cycle test. The temperature dependence of the resistivity of the material determined under zero load conditions is shown in Figure 2-10 as a representation of the method for determining transformation temperatures via resistive measurements. The transformation temperatures are determined from this data by the construction of linear, polynomial curve best fits through the low temperature, intermediate temperature, and high temperature portions of

the heating and cooling curves, respectively. In the intermediate temperature range where a mixture of the parent and martensite phases exist, the best linear fit is found by scanning a window of a specified temperature width through the entire intermediate temperature range. An array of linear best fits and associated R values is constructed. The series of linear regressions are then ranked by R values and the best fitting regression is used. Through the utilization of the equations for these best fits, start and finish temperatures were determined by interrogating the intersection points. Figure 2-10 exemplifies why resistance measurements are a prominent characterization technique in the study of shape memory alloys as there is a substantial difference in the electrical resistivity between the parent B2 and martensite phases. A summary of the complete algorithm is summarized in the data flow diagram shown in Figure 2-13.

The timed acquisition mode was employed when a continuous acquisition of data was required. There are two main functions for this mode. Timed acquisition may be used to optimize heat treatment times and temperatures as a result of the effects of internal stresses, dislocation structure, grain size and precipitate-matrix interactions and their respective kinetics. In the current study, the timed acquisition mode was developed for integration of thermo-mechanical testing methods with in-situ resistivity measurements. For this purpose, an external communication channel was developed, which continuously sends a signal to the MTS servo hydraulic controller proportional to the measured resistivity values thus allowing for a resistivity record on the same system that is acquiring thermo-mechanical data. This allows for a point by point correlation between the measurements ultimately leading to the simultaneous documentation of resistivity, stress, strain, and temperature.

Experiments were conducted on a Pt wire (Figure 2-11) and a NIST steel resistivity (Figure 2-12) standard³⁴ in order to determine the accuracy of the instrument and calibration. The resistivity vs. temperature relationships for both materials are shown in the figures below. For the platinum wire, the resistivity vs. temperature relationship should be linear in the temperature range of RT to 900 °C. The measurement shown in Figure 2-11 which confirms the linearity of this relationship indicating the accuracy of the resistivity apparatus in both heating and cooling modes. The NIST steel resistivity standard was measured in order to verify the calibration of the absolute values of resistivity as a function of temperature. These results are shown in Figure 2-12 and confirm a high degree of accuracy between these resistivity measurements and the measurements made by NIST. Figure 2-12 compares NIST measurements with our results via level crossing acquisition in a sample configured with a 4 point probe and spot welded thermocouple. A low and high range exist in analog amplifiers which allow for higher precision measurements in lower resistivity samples. Figure 2-12 includes measurements for the low and high range both of which are within the margin of error specified by NIST for the resistivity standard.

Thermomechanical Testing

Thermomechanical instrumentation

Mechanical testing was performed on an MTS servo-hydraulic test frame equipped with an MTS 484 controller and MTS software. MTS 646.10B hydraulic collet grips with a modified 680 LCF grip set were used to grip the threaded specimens. A 20 kip load cell was used and strain measurements in tension were taken with an MTS Model 632.51B-04 extensometer using a 12.7 mm gage length. This extensometer is equipped with 85mm long quartz probes with a v-chisel edge having a maximum range of

+20/-10% strain. Strain measurements during compression testing were acquired using a laser extensometer. Specimens were induction heated using an Ameritherm Novastar 7.5 power supply.

Resistivity measurements were integrated with the uniaxial mechanical tests, facilitating measurement of transformation temperature, determination of the matrix phase as well as determine if a phase change occurred during the test while simultaneously determining mechanical properties. Additionally this test technique was used to verify the materials phase fractions. The tensile or compressive sample was instrumented with a four point probe and a K-type thermocouple. A four point probe configuration was again chosen in order to eliminate the effects of contact resistance. Nickel wires were spot welded to the sample functioning as the voltage sensing leads. Current excitation was supplied through the hot grips. This instrument has been developed at the NASA Glenn Research Center advanced metallics branch. Figure 2-14 with key components labeled shows this working configuration on a Materials Testing Systems (MTS) tensile frame fitted with high temperature hot grips and induction heating.

K thermocouples were spot welded to the sample. Temperature gradients across the gauge were to within +/-0.5% of the test temperature by calibration on a control sample fitted with three thermocouples while actual test samples contain a single centrally located thermocouple. A problem inherent to spot welding is the formation of stress raisers during the rapid melting and solidification of a narrow region adjacent to the spot weld base and the wire (weld nugget). The radius of the nugget is a critical factor in determining the stress concentration at the weld and impacts the fracture stress and strain

of a sample. During a spot weld a predefined amount of energy is stored in a capacitive system and subsequently discharged through a welding probe following the path of least resistance. As the discharge passes from the wire to the sample or base metal a small region melts first. This event leads to the contact resistance in this very narrow region dropping significantly which results in the remaining discharge to focus through this path. The result is a very sharp defect on the sample's surface. This problem was minimized by using a multistep spot-welding procedure. Initially multiple low energy spot welds are made at closely spaced distinct locations, which assures numerous wide wire to sample contact points. Although these wide contact points are not mechanically strong enough to withstand the stress during sample handling, loading, and deformation they provide multiple wide low resistance interfaces. Step two consists of a second pulse that is approximately 10X greater in discharge energy than those employed in step one. The secondary pulse forms a strong weld nugget with a wide radius thus reducing the stress concentration at the weld.

Uniaxial isothermal mechanical tests

Tensile specimens were strained to failure in strain control at a rate of $1 \times 10^{-4} \text{ sec}^{-1}$. If a specimen reached the 20% limit of the extensometer, the sample was unloaded under strain rate control until reaching a 0N trigger after which the control mode was switched to load control. The specimen was then allowed to cool and then unloaded. Compression tests were run in displacement rate control at approximately the same strain rate. Use of displacement control was necessary due to limitations in the maximum scan rate of the extensometer and the acquisition rate required by the MTS controller for proper and safe PID (proportional integrating differentiating) control. Analysis of the stress strain curves

and determination of the proportional limit was facilitated by proprietary NASA Glenn Research Center Advanced Structures Division software.

Load free strain recovery tests

In the unconstrained or load free strain recovery tests, tensile specimens were deformed in strain rate control. The maximum strain level trigger was set, which upon crossing reverses the strain rate to a compressive $1 \times 10^{-4} \text{ sec}^{-1}$ until the sample is fully unloaded. When the load reached 0 N the controller was switched to load control. Load was held at 0 N while the specimens were thermally cycled to a temperature in the range of 400 °C. Heating rates were maintained at 10 °C/min after which the samples were allowed to air cool to well below the M_f before further loading. The recovery rate was determined by monitoring the sample's strain during the thermal cycling.

Load bias test

Load bias testing measures an SMA's ability to perform work. This is accomplished by measuring strain under a constant load. Three modes of load bias test were employed in this study. The primary tensile load bias tests were run in a series of progressive loads on the same sample. Specimens were deformed in strain rate control (of $1 \times 10^{-4} \text{ sec}^{-1}$) near room temperature to the predefined holding load. At this point the controller was switched to load control holding a constant load. Specimens were finally thermally cycled twice from room temperature to about 100 °C above the austenite finish temperature. Heating rates were maintained at 10 °C/min followed by air cooling. An auxiliary fan was turned on after the sample temperature dropped below the M_f , providing additional cooling. In this test specimens were unloaded at near room temperature and then strained again to the next higher load level. This procedure was repeated for each load. The work output was calculated by measuring the resultant

change in strain during the martensite-to-austenite transformation during the second heating cycle and multiplying by the applied stress. Additionally a series of tests were run on samples with an identical procedure except that the samples were unloaded hot while austenitic or above the A_f . Compression load bias tests were run in a parallel procedure in displacement rate control rather than strain rate control with near room temperature unloading.

In summary several test modes are utilized each targeting the measurement of specific material and shape memory properties. Resistivity measurements targeted determination and stability of the no load transformation temperatures as well as quantify the temperature dependence of the resistivity of the austenite and martensite phases. Isothermal uniaxial tests combined with data from dynamic modulus tests were used to determine the baseline mechanical properties of each phase as well as the mechanical behavior of the alloys near the transformation temperatures. Furthermore, load free recovery experiments measured the effectiveness of the alloys in recovering elastic and plastic strains while the load bias testing was used to determine the alloys specific work output. Finally the cool at load test measured the stress dependence of the transformation temperatures as well as the transformational strains under load.



Figure 2-1 Induction melted $\text{Ni}_{19.5}\text{Pd}_{30}\text{Ti}_{50.5}$ cast ingot with attached hot top on a quarter inch grid.

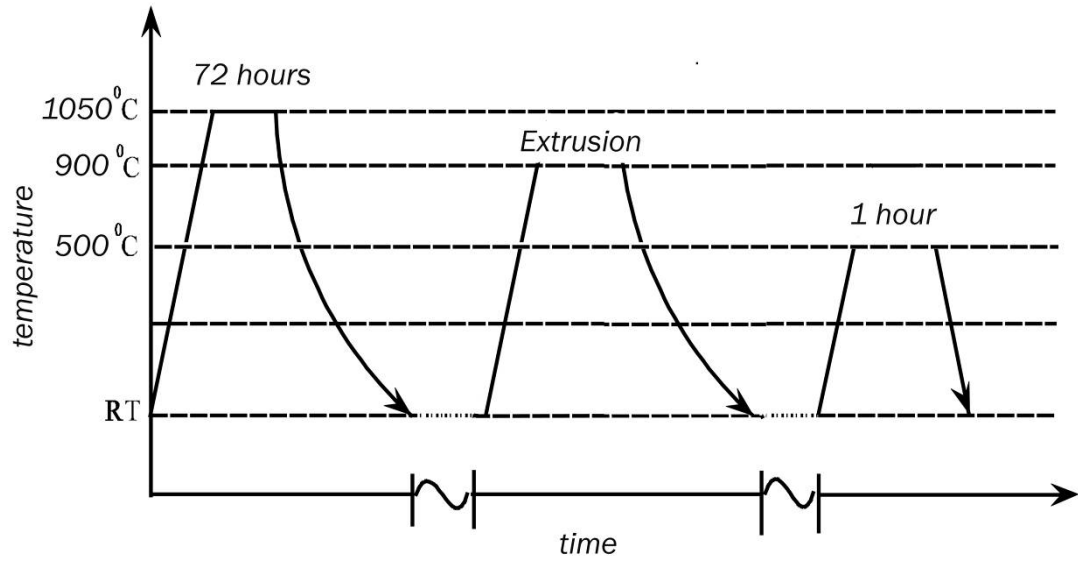


Figure 2-2 Heat treatment and processing temperature schedule.

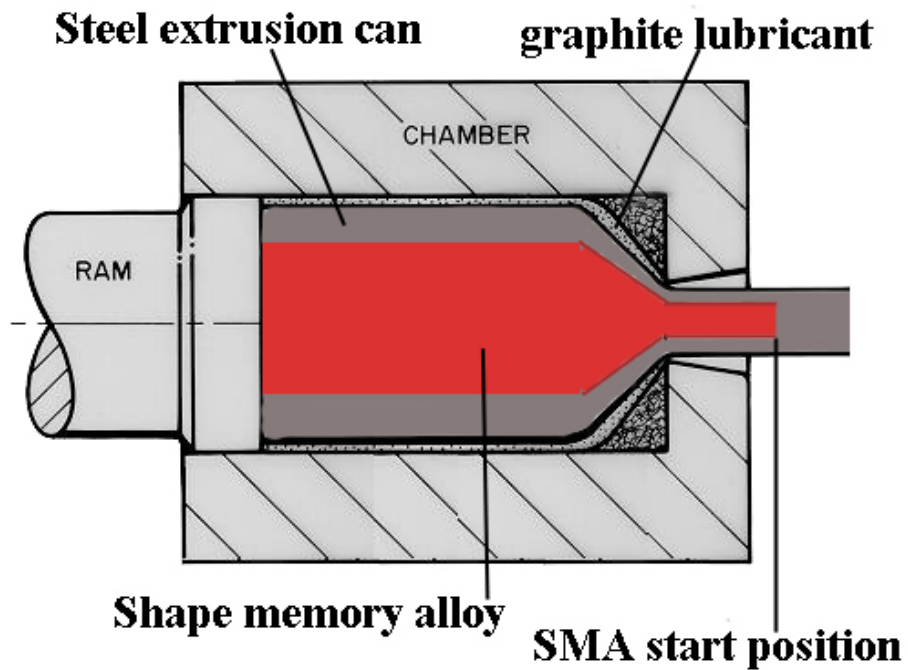


Figure 2-3 Hot extrusion press schematic

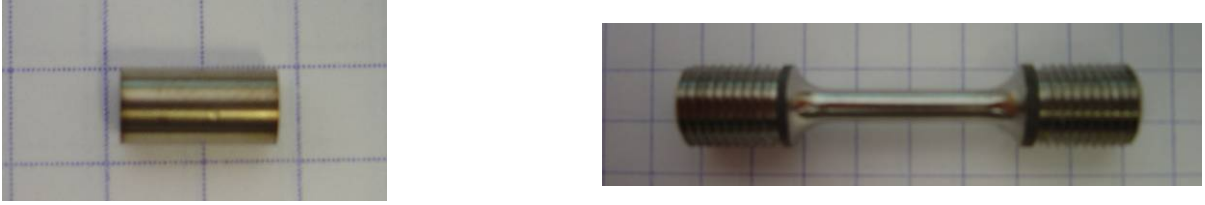


Figure 2-4 Uniaxial sample (A) 5 X 10 mm compression sample (B) Threaded 17.4 mm long by 3.81 mm diameter gauge sample.

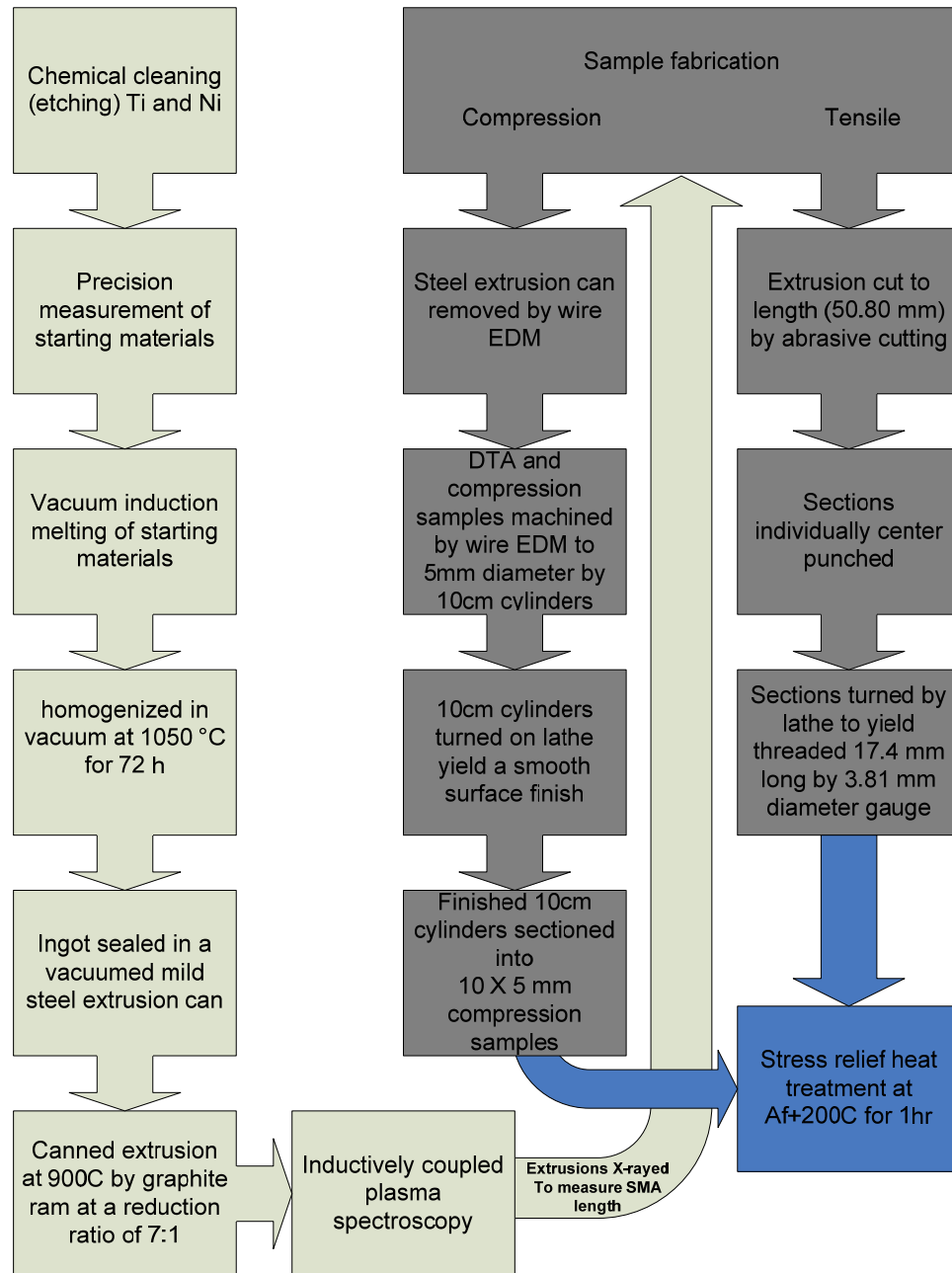


Figure 2-5 Processing flow diagram of DSC, compression, and tensile samples.

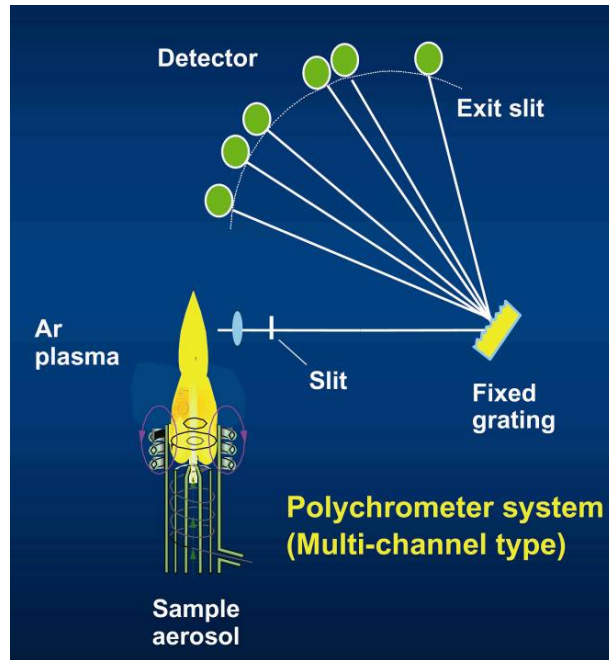


Figure 2-6 The ICP using an Echelle type polychromometer³²

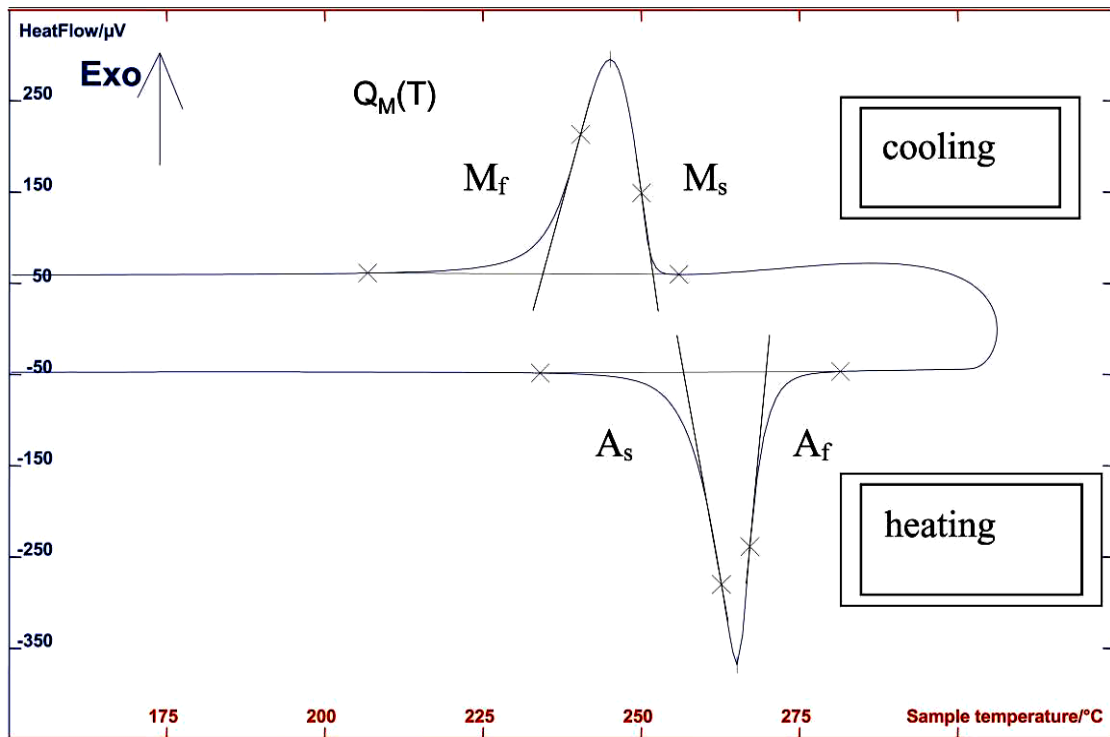


Figure 2-7 Example of a DTA scan showing the exothermic and endothermic peaks characteristic of thermoelastic shape memory alloys

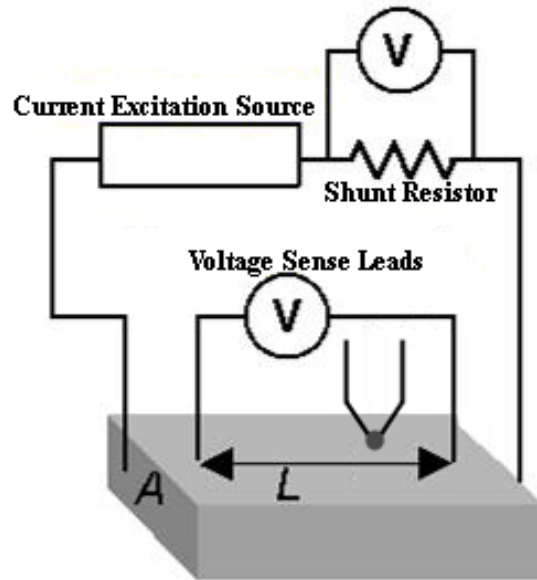


Figure 2-8 Four-point probe resistivity configuration

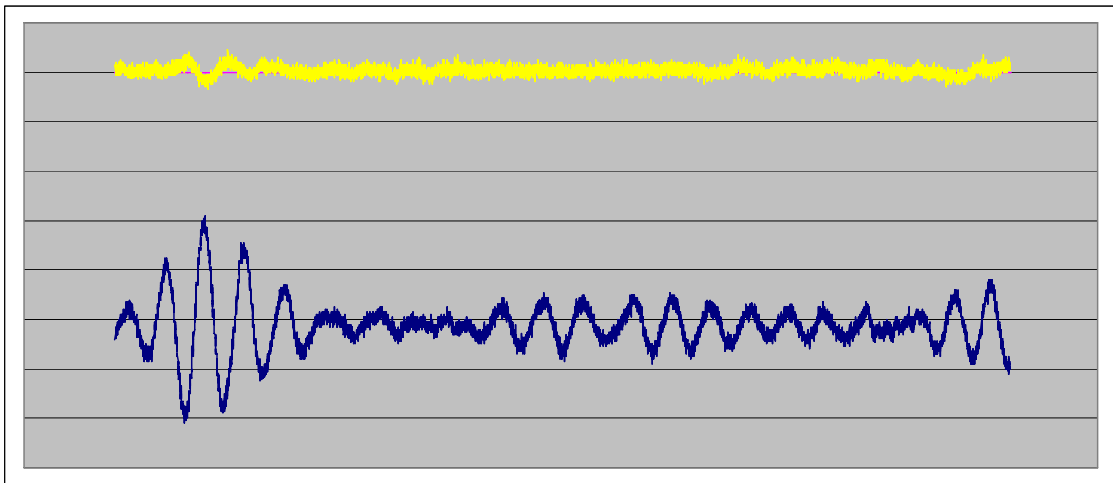


Figure 2-9 Raw (blue) and conditioned (yellow) voltage signals for resistivity measurements during inductive heating

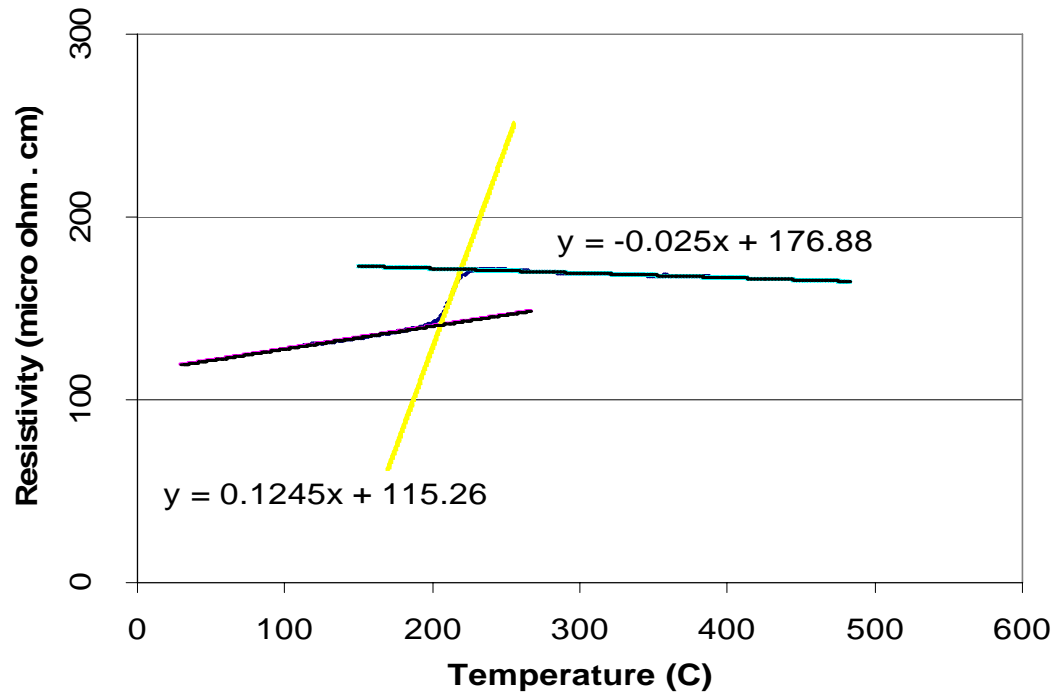


Figure 2-10 Resistivity vs. temperature profile with regression analysis

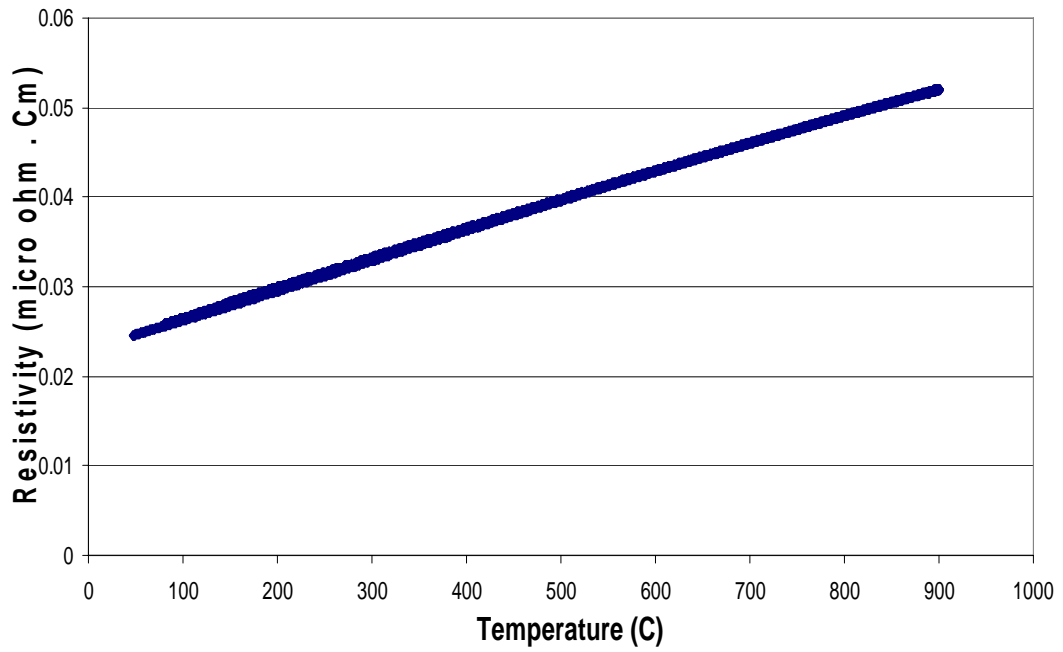


Figure 2-11 High conductivity Pt wire resistivity vs. temperature relationship demonstrating the repeatability of the during heating and cooling

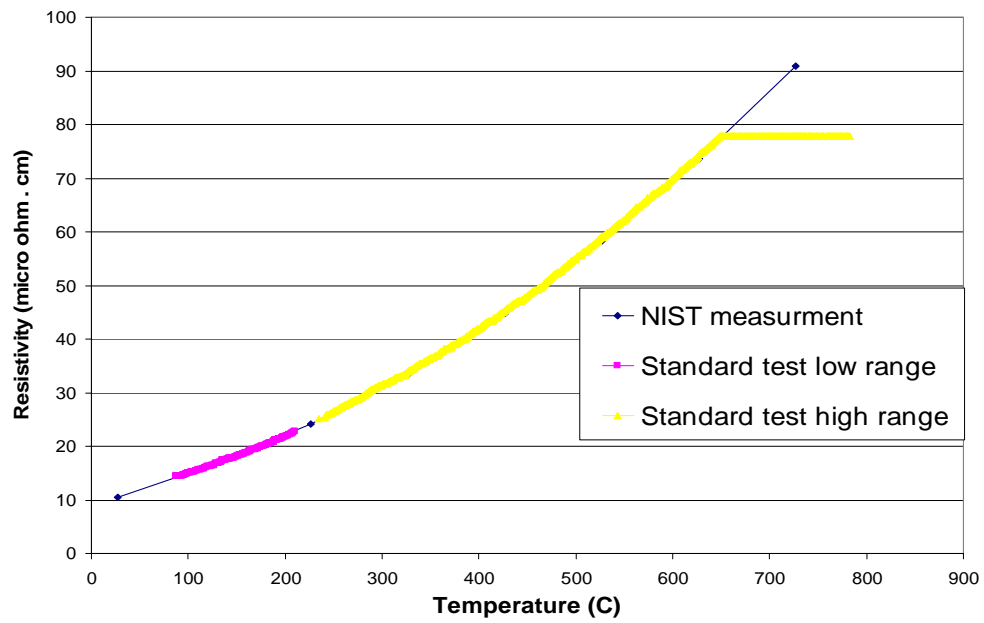


Figure 2-12 NIST (resistivity standard) resistivity vs. temperature profile comparison of NIST measurements and the measurements by the resistivity apparatus.

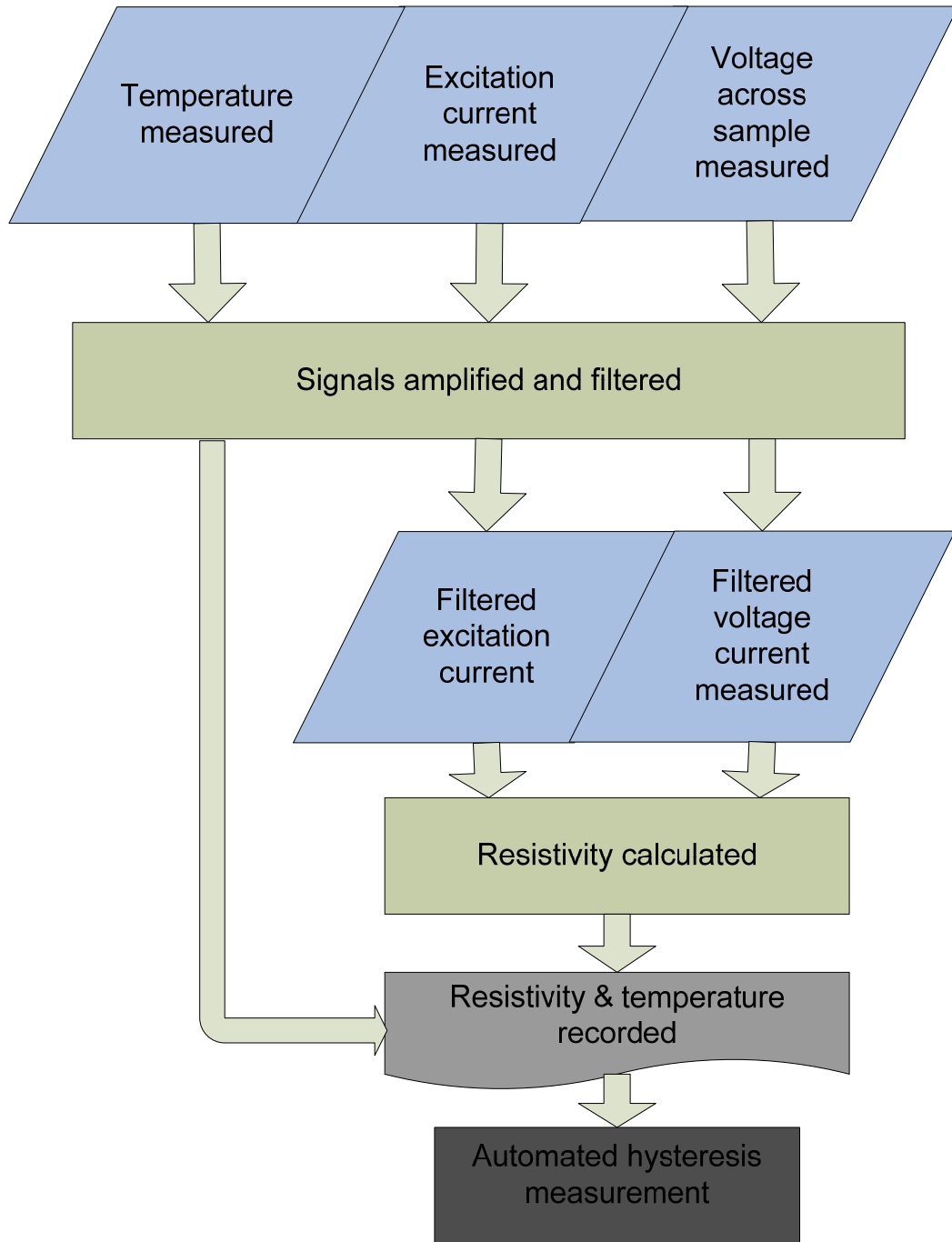


Figure 2-13 Resistivity apparatus data flow diagram.

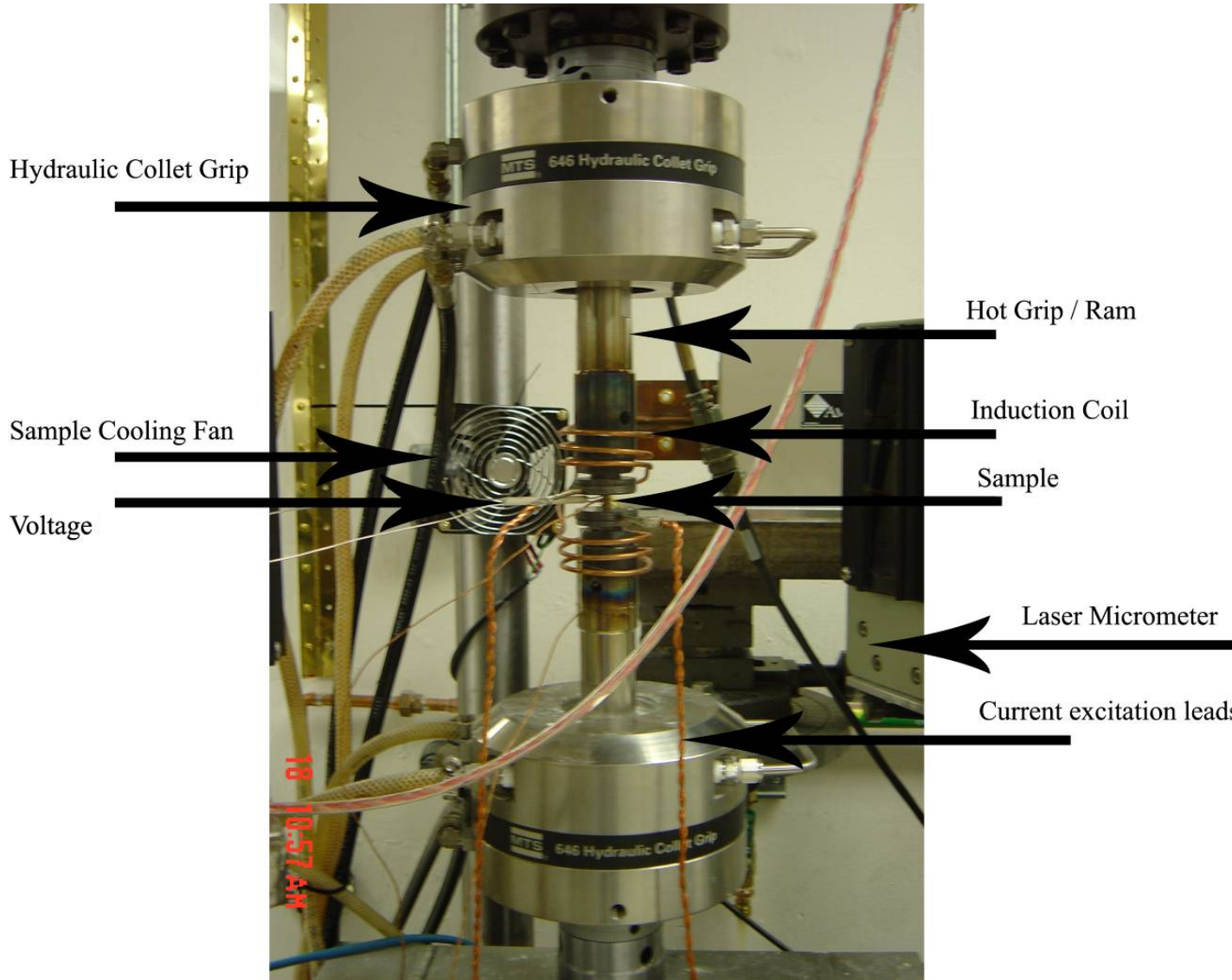


Figure 2-14 Materials Testing Systems (MTS) tensile frame fitted with high-temperature hot grips and induction heating configured for compressive testing.

CHAPTER 3 ALLOY DEVELOPMENT

The alloy development section of this study consists of two parts addressing the selection of the Pt and Pd modified NiTi alloys studied in detail in Chapter 4. The NiTiPt alloy was selected based on the results from the study of over 20 NiTiPt alloys, which focused on elevated transformation temperatures, effects of stoichiometry on microstructure, and the results of prior baseline thermo-mechanical studies showing good work output. The NiTiPd alloy was selected based on studies others have performed, which have focused on transformation temperatures and no-load recovery tests.

In Chapter 4, the thermomechanical properties of the chosen baseline $\text{Ni}_{19.5}\text{Pd}_{30}\text{Ti}_{50.5}$ alloy will be presented. The majority of the thermo-mechanical tests performed on the Pd modified alloy were also performed in a parallel effort on the chosen Pt-modified $\text{Ni}_{24.5}\text{Pt}_{25}\text{Ti}_{50.5}$ alloy. Data from investigations on the Pt alloy will be drawn upon for comparison to the Pd alloy, which exhibits similar structural transformations yet has quite different mechanical properties and shape memory performance. The underlying motivation of such a study is to compare the mechanical properties and materials performance of the two HTSMA systems, thus allowing for the identification of areas where further alloy development may improve the materials performance.

Characterization of the NiTiPt SMA system

Bulk Compositional Analysis

Selection of a baseline Pt-modified alloy was accomplished by a cursory study of the effect of near stoichiometric Pt alloying additions on transformation temperatures and

microstructure of NiTi alloys. Stoichiometric alloys refers to alloys which lie approximately along the $\text{Ni}_{50-x}\text{Pt}_x\text{Ti}_{50}$ iso-stoichiometric line between the binary NiTi and NiPt intermetallics. This term will be used throughout for the NiTiPt and NiTiPd ($\text{Ni}_{50-x}\text{Pd}_x\text{Ti}_{50}$) alloy. Prior studies have shown that ternary Pt additions produce elevated transformation temperatures well above the transformation temperatures of NiTi. Thus one would expect to find potential high-temperature shape memory behavior in this system. As a matter of fact, Pt additions are superior to all other current alloying modifications to NiTi at increasing transformation temperatures, even so, this system has received little attention in the form of characterization studies or alloy development. Three groups of alloys were chosen for characterization: stoichiometric alloys, Ti rich alloys in which the fraction of Ti in the alloy is greater than 50 at.% and Ti deficient alloys which have atomic fractions of Ti less than 50 at.%.

A ternary compositional plot of the experimental compositions selected for this alloy development study is shown in Figure 3-1. The stoichiometric alloys are denoted with a E#### designation and Ti rich and deficient alloys are designated with an F#### designation. Subsequent to this study two stoichiometric alloys of 20 and 30 at% Pt denoted as baseline alloys as designated in Figure 3-1 were selected for detailed thermomechanical testing and characterization.³⁵

Transformation Temperature

Transformation temperatures as determined by DSC or DTA are given in an inclusive list tabulated in Table 3-3. It was determined that the transformation temperatures in $\text{Ni}_{50-x}\text{Pt}_x\text{Ti}_{50}$ alloy system are strongly dependent on Pt content along the $\text{Ni}_{50-x}\text{Pt}_x\text{Ti}_{50}$ iso-stoichiometric line between the binary NiTi and TiPt intermetallics. The transformation temperatures in the alloys of stoichiometric compositions designated with

an E prefix are in good agreement with several other reported values.³⁶⁻³⁸ Figure 3-2 (A) compares several reported values of the M_s temperature as a function of Pt for Ni stoichiometric alloy additions while the complete set of transformation temperatures are documented in this study are presented in Figure 3-2 (B). Minor alloying additions of Pt resulted in a depression in transformation temperatures up to approximately 10 at% Pt after which further alloy additions resulted in a potent increase in transformation temperature with additional Pt content.

A slight discrepancy exists between the transformation temperature measurements taken by Lindquist and Wayman and the results of the current study. This discrepancy is evident primarily in the compositional region where the transformation temperatures are depressed by alloying additions. The current study and the measurements found in (37,38) determine the transformation temperatures by calorimetric methods (DSC or DTA) while Lindquist and Wayman employed electrical resistivity measurements to determine the transformation temperatures. As described previously, transformation temperature analyses by thermal methods are based on the extrapolated onset method where the baseline is forced to have a nearly flat slope. Resistivity measurements, on the other hand, rely on deviations in the slope of the ρ vs. T curves determination of transformation temperatures the base line is formed by the temperature dependence of the samples resistivity. Therefore resistive analysis is dependent on the slope of the baseline and the slope of the transition region. It is possible that the differences between the thermal and resistive account for this discrepancy. Another possibility is that differences in thermomechanical processing, heat-treatments and or minor deviations from stoichiometry may account for slight discrepancies.

It is known for binary NiTi and the NiTiPd systems that the transformation temperatures are highly dependent on stoichiometry. Particularly, in some NiTi based shape memory alloy slight deviations which make Ni rich NiTi alloys and Ni+Pd rich NiTiPd alloys results in a strong depression in the transformation temperatures. The NiTiPt alloys however differ from these systems in the amount of suppression by casting Ti deficient alloys. A comparison of E430 and F311 alloys (Table 3-3) which both have 25% Pt contents reveals the a 3% deficiency in Ti decrease the transformation temperatures from only 29 degrees Celsius. Contrasting this to a comparable 3% Ti deficiency in the NiTiPd alloys which results in a decrease of transformation temperatures of over 220 degrees Celsius, it is evident that the stoichiometric effects on transformation temperatures are not as pronounced in the NiTiPt shape memory alloys. The details of the effects of stoichiometry on NiTiPd shape memory alloy system are discussed in its alloy development section later in this chapter.

Microstructure

As expected, all the stoichiometric alloys were essentially single phase. Micrographs of these alloys were omitted as they did not provide any useful information other than essentially confirming the single phase nature of the microstructure. Focusing on the deviations from stoichiometry alloys with excess or deficient Ti ratios did not exhibit an increase in transformation temperatures but rather a suppression of the transformation occurred in non-stoichiometric alloys.

Conversely, most of the non-stoichiometric alloys, designated by the prefix F, were found to contain a second phase. Figure 3-3 is a summary of SEM back scattered electron micrographs of the microstructures for all the F-series alloys. Samples F303 and F304 are essentially single-phase non-stoichiometric alloys, in that they do not contain a

second intermetallic phase. The spherical dark phase in these alloys is probably TiO_2 , which is common to all the alloys. The microstructure for these two alloys is similar to that observed in the E-designated alloys. F303 is comparable to the microstructure of the lower Pt E-series alloys where the martensite is finely distributed and F304 is similar to the higher Pt E-series alloys with a coarser martensitic distribution.

Most of the alloys contain second phases including alloys close to the line of constant stoichiometry which indicates that the solubility of excess alloying additions on either side of this line is very narrow. Only two non-stoichiometric alloys that did not contain a second intermetallic phase were observed on the Ti rich side of this line of constant stoichiometry. Both of these alloys contained Ti-rich interstitial containing phases probably oxides. Therefore, any excess Ti could be tied up as TiO_2 and the bulk matrix phase was probably very close to a stoichiometric composition. Consequently this signals that there is probably little solubility for excess solute on either side of stoichiometry.

Both phase diagrams are recent assessments of the respective binary system. Based on the compositional analysis and basic morphology of the microstructures shown in Figure 3-3, there are basically two types of second phases observed in the non-stoichiometric alloys. All the (Ni+Pt)-rich alloys contain a lath like structure with a 2:3 Ti:(Ni+Pt) ratio. Given the nature of this phase, it would appear that it forms by nucleation in the solid state. An intermetallic phase with the stoichiometry of $\text{Ti}_2(\text{Ni,Pt})_3$ does not appear in either binary phase diagram, however, Ti_2Ni_3 is a metastable phase that is observed in binary NiTi alloys.³⁹ Consequently, the Pt could stabilize this phase. Or it is possible that it is a new phase, unique to the ternary phase diagram. It will take

additional quantitative x-ray diffraction or TEM analysis to determine the specific structure of this phase.

The non-stoichiometric alloys on the Ti-rich side of the line of constant stoichiometry have a phase that is more spherical or elliptical in morphology and usually located along the grain boundaries. This would indicate that it is possibly a low melting point phase that was last to form during solidification. This and the fact that the composition has a 2:1 Ti:(Ni,Pt) ratio, would indicate that it could be $Ti_2(Ni,Pt)$, which is isostructural to Ti_2Ni and has been previously identified by Garg.³⁹ A small percentage of other phases may also appear in these alloys.

Alloy Selection : NiTiPt

The results of the characterization of the ternary NiTiPt high-temperature shape memory alloy system are summarized above and were presented and published in a relevant conference proceeding.⁴⁰ The alloy design phase was intended to build a relationship between the compositional dependence of the transformation temperatures and microstructure in the NiTiPt system. This system was chosen for a detailed alloy study primarily due to evidence that Pt modified NiTi alloys exhibit the highest reported transformation temperatures of any NiTi based alloy as well as the fact that there is a very limited data available in the literature for this alloy system.²

The alloys were single or two phase and all contained a limited volume fraction of interstitial containing phases. The formation of a second phase was evident even with minor deviation in stoichiometry, therefore the solubility for excess components outside of the iso-stoichiometric line between NiTi and TiPt is limited. The formation of interstitial containing phases ties up Ti thus depleting the matrix by an amount which depends on the bulk interstitial concentration. There for in order to insure that both the

alloys are not Ti deficient the Ti concentration should be increased slightly above the expected interstitial impurity concentration.

Two alloys were selected for detailed thermomechanical testing from the NiTiPt and NiTiPd alloy systems. Focusing on the selection of a composition in the Pt modified NiTi alloy, the position along the stoichiometric line between NiTi and PtTi was selected based on a compromise between elevated transformation temperatures and good mechanical properties. As previously mentioned two baseline alloys ($\text{Ni}_{50-x}\text{Pt}_x\text{Ti}_{50}$ containing 20 and 30 at% Pt) along with a binary NiTi alloy (SM495 NiTi) supplied by Nitinol were selected for detailed thermomechanical testing by colleagues at the NASA Glenn research center.³⁵

The alloys were prepared in a manner similar to that described in Chapter 2. The materials were prepared by melting, extrusion, and subsequent machining of tensile dog bone test specimens. Along with isothermal uniaxial tensile testing, load bias testing was conducted on the 20 and 30 at% Pt extrusions along side the binary NiTi. Load bias testing or constant-load, strain-temperature tests measure a materials ability to do work against a constant biasing load which is a key design parameter in the development of shape memory actuated devices³⁵ and therefore must be considered in combination with a high transformation temperatures in the selection of HTSMAs. Figure 3-6 shows the results of a load bias examination in conjunction with results from a comparable test documented in a characterization study of binary NiTi alloys.⁴¹

The applied tensile stress is related to a volume specific work output or work density. SM495 NiTi followed by the stoichiometric and the Ti rich NiTi show the highest specific work output yet the transformation temperatures are near room

temperature. The 20 and 30 at% Pt modified alloys however have much higher transformation temperatures (262C and 560 °C Ms temperatures respectively) but the work output is lower. In the 20 at% Pt modified alloy the work output was marginally lower than that of the binary alloys at much higher transformation temperatures. In contrast the 30 at% alloy exhibited the highest transformation temperature of all the alloys encompassed in this study yet did not perform work under any biasing load. Therefore, although this material exhibited high transformation temperatures, it is not directly useful in application requiring actuation forces of any level.

Based on the findings of this study and those in reference [35] a new baseline composition of $\text{Ni}_{24.5}\text{Pt}_{25}\text{Ti}_{50.5}$ was selected for investigation in this study based on a compromise between elevated transformation temperatures potential work output. Although this alloy was not included in the NASA NiTiPt baseline alloy advanced mechanical characterization study³⁵ it lies within the compositional bounds of the $\text{Ni}_{20}\text{Pt}_{30}\text{Ti}_{50}$ and $\text{Ni}_{20}\text{Pt}_{30}\text{Ti}_{50}$ alloys. The transformation temperatures in the 30 at% Pt alloy was high but the alloy exhibited no evident capacity for producing work while the 20 at% alloy exhibited a high work output at a much lower transformation temperature. The $\text{Ni}_{24.5}\text{Pt}_{25}\text{Ti}_{50.5}$ alloy lies halfway between these tests and therefore by extrapolation it was assumed that this alloy would demonstrate some capacity for performing work at with transformation temperatures centered around 450C.

Alloy Selection : NiTiPd

NiTi and PdTi, like the NiTiPt system, also form a continuous solid solution with a high-temperature B2 phase that transforms to a B19 (orthorhombic) or B19' (monoclinic) low-temperature martensite phase with transformation temperatures between those of the

binary alloys.⁴² Figure 3-7 is a map of the thermodynamically stable thermoelastic transformation reactions as a function of composition and temperature for the NiTiPd alloys.⁴³ The Pt and Pd modified NiTi both follow similar transformation reactions at similar alloying additions but with differing effectiveness of the ternary alloying additions at increasing the transformation temperatures. Figure 3-8 (A) illustrates the relationship between transformation temperature and alloying additions in both systems.¹⁶ As shown in this diagram it has been confirmed that the martensitic transformations over the entire range of ternary Ni-Pd-Ti compositions are thermoelastic in nature and that the alloys exhibited aspects of shape memory behavior similar to binary NiTi alloys.^{44, 45}

The level of Pt in the NiTiPt alloy was chosen on the basis of transformation temperatures and the work output. To the best of the author's knowledge, in the NiTiPd shape memory alloy system no such tests results (load bias) are available in the literature. However, measurements of the alloy's stress free strain recovery have been examined in prior studies.¹¹ Through dilatometry and uniaxial ambient temperature tests the compositional dependence of the shape recovery at specific initial strain intervals was examined. The findings of this study are summarized in Figure 3-8 (b) where the recovery strain is plotted as a function of alloy composition and initial plastic strain. For all strain increments the maximum shape recovery is approximately at 30 at% Pd. Additionally it has been shown that the shape memory behavior of NiTi-30Pd (at.%) alloys can be quite good under unconstrained conditions with samples loaded to 2-4% total strain levels in the martensitic condition recovering 100% of the strain while those loaded up to 6% recovering 90% of the strain.^{36, 46, 47} Similar shape memory behavior has been observed for samples deformed in compression⁴⁸ and torsion.⁴⁹ Alloys containing

40 at.% or more Pd including the TiPd binary alloy could only recover about 0.5% strain in tension to various strain levels.^{36, 49} This poor shape memory performance has been attributed to a low critical stress for slip (which is an irreversible process), such that the majority of the deformation is accommodated by slip rather than the more typical twin boundary motion or martensite reorientation (also referred to as detwinning).⁴⁹

As a result of the findings listed above a base composition of $\text{Ni}_{19.5}\text{Ti}_{50.5}\text{Pd}_{30}$ was selected for the Pd modified alloy. The alloy is developed with a slightly Ti (approximately .5 at%) rich composition in order to ensure high transformation temperatures. Transformation temperatures are highly linked stoichiometry following the relationship $\text{Ni}_{50-x}\text{Pd}_x\text{Ti}_{50}$. Compositional deviations veering into the Ti lean side of the iso-stoichiometric line between TiNi and TiPd ($\text{Ni}_{50-x}\text{Pd}_x\text{Ti}_{50}$) strongly decreases transformation temperatures in contrast to Ti rich compositions which have little effect on the transformation temperatures. Figure 10 confirms the compositional dependence of the transformation temperatures for off-stoichiometric alloys at fixed Pd fractions ($\text{Ni}_{20+x}\text{Pd}_{20}\text{Ti}_{50-x}$). The effects of stoichiometry on the transformation temperatures in the ($\text{Ni}_{20+x}\text{Pd}_{20}\text{Ti}_{50-x}$) alloy is similar to those exhibited by binary NiTi ($\text{Ti}_{50-x}\text{Ni}_{50}$) where compositions crossing into the Ti deficient iso-stoichiometric line results in a sharp decrease in transformation temperatures.⁵⁰

It is a well known fact that Ti has a high interstitial affinity. In the system under study, the main interstitial impurity elements are C and O which enter the melts as impurities during the alloy melting process. These interstitial elements react with Ti to form titanium oxides and carbides thus depleting titanium from the alloy by tying it up in interstitial compounds. By forcing the alloy to be Ti rich by a fraction greater than the

impurity concentrations results in a final alloy composition which remains Ti rich by an amount proportional to the excess Ti not consumed in the formation of oxides. The goal is to keep the overall matrix composition stoichiometric or slightly Ti-rich, thus guaranteeing a high transformation temperature. Additionally Ti rich compositions yield a fraction of the intermetallic phase $Ti_2(Ni,Pd)$ which is isostructural to Ti_2Ni .³⁹ $Ti_2(Ni,Pd)$ is an interstitial stabilized phase which has a high solubility for interstitial oxygen.⁵¹ The presence of this phase allows for further removal of interstitials from the martensite or austenite matrix which has a lower interstitial solubility. This alloying approach has been employed in previous studies of the Pt modified NiTi SMAs.³⁵

Alloy Selection Summary

The NiTiPt alloy was selected based on the results from our study on elevated transformation temperatures, effects of stoichiometry and the results of prior baseline thermo-mechanical studies measuring work output. In the Pd modified NiTi no such advanced thermo-mechanical studies existed thus the alloy selection was centered around existing studies which demonstrated a composition dependent maximum in the unconstrained or no load shape recovery. Consequently, the final selection of alloys for this study are $Ni_{19.5}Pd_{30}Ti_{50.5}$ for advanced thermo-mechanical testing in parallel to the $Ni_{24.5}Pt_{25}Ti_{50.5}$ for comparison of mechanical and thermoelastic properties. Each alloy is developed with a slightly Ti (approximately .5 at%) rich composition to prevent Ti-loss from the matrix resulting in a Ti-poor alloy with lower transformation temperatures.

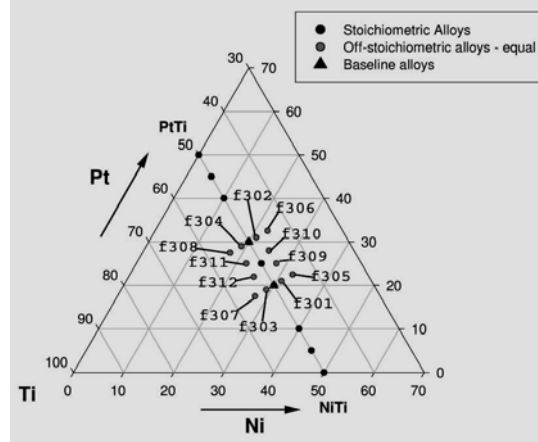


Figure 3-1 Ternary plot of the Ti-Ni-Pt compositions studied. The composition of all alloys was confirmed by spectrographic analysis

Table 3-2 Aim and measured compositions of all alloys investigated.

sample designation	Aim Composition (at.%)			Measured Compositions (at.%)					
	Ti	Ni	Pt	Ti	Ni	Pt	C	N	O
E426	50	50	0	49.96	49.73	0	0.05	0.01	0.18
E427	50	45	5	49.86	45.13	4.58	0.08	0.01	0.26
E428	50	40	10	50.02	40.01	9.66	0.06	0.02	0.17
E429	50	30	20	49.43	29.52	20.64	0.07	0.02	0.25
E430	50	25	25	49.88	25.25	24.48	0.07	0.02	0.22
E431	50	20	30	49.77	20.03	29.81	0.08	0.03	0.21
E432	50	10	40	49.83	9.78	39.94	0.07	0.02	0.24
E433	50	5	45	49.94	5.04	44.53	0.11	0.03	0.23
E434	50	0	50	49.9	0	49.48	0.08	0.04	0.3
F301	48	31	21	48.02	31.01	20.45	0.12	0.08	0.28
F302	48	21	31	47.79	20.79	30.79	0.11	0.12	0.36
F303	52	29	19	52.03	29.01	18.5	0.09	0.07	0.23
F304	52	19	29	51.58	19.38	28.52	0.13	0.09	0.25
F305	45	32.5	22.5	45	32.27	22.35	0.05	0.05	0.25
F306	45	22.5	32.5	44.84	22.76	31.87	0.076	0.05	0.3
F307	55	27.5	17.5	54.02	28.26	17.16	0.08	0.08	0.37
F308	55	17.5	27.5	54.46	18.23	26.73	0.1	0.108	0.23
F309	47	28	25	46.81	27.89	24.77	0.11	0.09	0.27
F310	47	25	28	47.05	25	27.43	0.11	0.08	0.25
F311	53	22	25	52.58	22.35	24.49	0.13	0.1	0.29
F312	53	25	22	52.59	25.08	21.68	0.12	0.09	0.38
F313	48	21	31	38.79	25.24	35.54	0.09	0.07	0.2

Table 3-3 Transformation temperatures of alloy set

Sample designation	A _s (°C)	A _f (°C)	M _s (°C)	M _f (°C)
E426	60	86	57	35
E427	51	65	46	25
E428	86	94	87	76
E429	313	322	312	296
E430	449	484	436	394
E431	600	653	591	527
E432	838	917	811	751
E433	963	998	917	869
E434	1044	1069	1018	996
F301	284	352	307	239
F302	666	780	605	552
F303	268	302	259	212
F304	526	560	492	424
F305	444	511	459	379
F306	no peaks			
F308	486	519	470	423
F309	449	507	446	382
F310	552	617	523	468
F311	420	453	402	363
F312	342	374	286	330

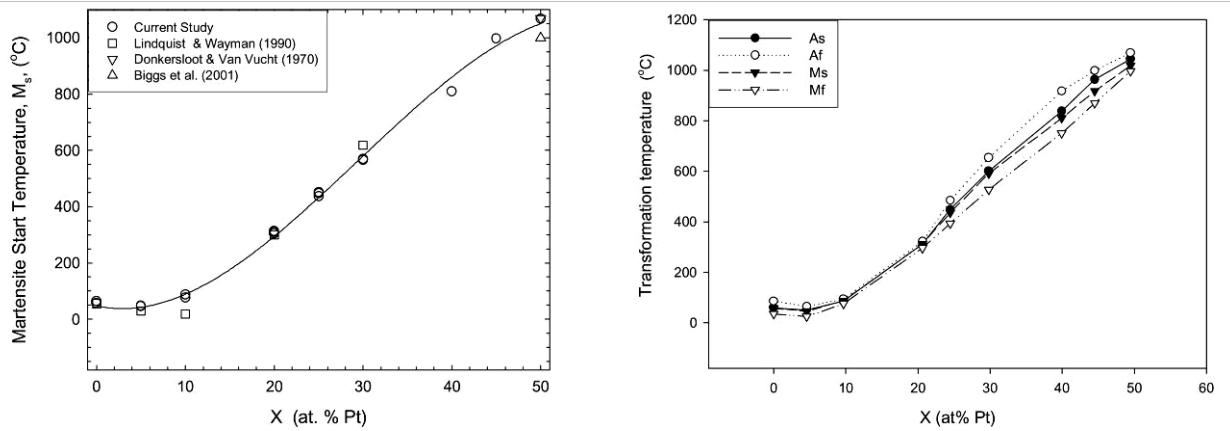


Figure 3-2 A. Effect of Pt on the M_s transformation temperatures for Ni_{50-x}PtTi₅₀ alloys, including data from previous researchers B. Effect of Pt on all transformation temperatures for Ni_{50-x}PtTi₅₀ alloys

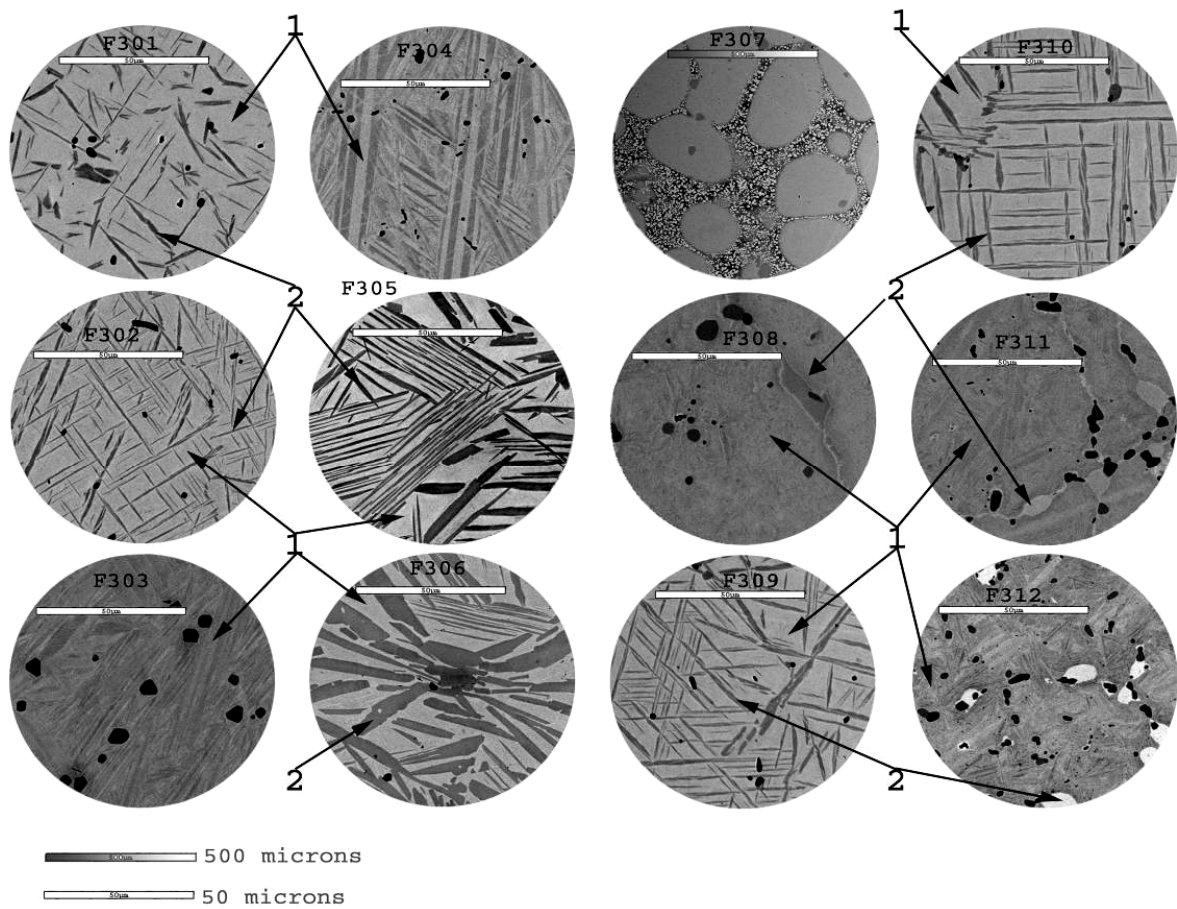


Figure 3-3 SEM BSE micrographs of the non-stoichiometric alloys.

Table 3-4 Semi-quantitative EDS analysis of the various phases observed.

Sample ID	Bulk Composition (at.%)			Region 1 (martensite) (at.%)			Region 2 (second phase particle) (at.%)		
	Ti	Ni	Pt	Ti	Ni	Pt	Ti	Ni	Pt
F301	48	31	20	46	29	25	39	39	22
F302	48	21	31	47	18	36	39	29	31
F303	52	29	19	49	28	22			
F304	52	19	29	48	18	33			
F305	45	32	22	47	23	30	39	35	26
F306	45	23	32	46	15	39	38	27	34
F308	55	18	27	47	22	31	63	9	28
F309	47	28	25	45	25	29	44	28	28
F310	47	25	27	46	21	33	45	24	31
F311	53	22	25	50	21	29	67	2	32
F312	53	25	21	49	27	24	67	2	30

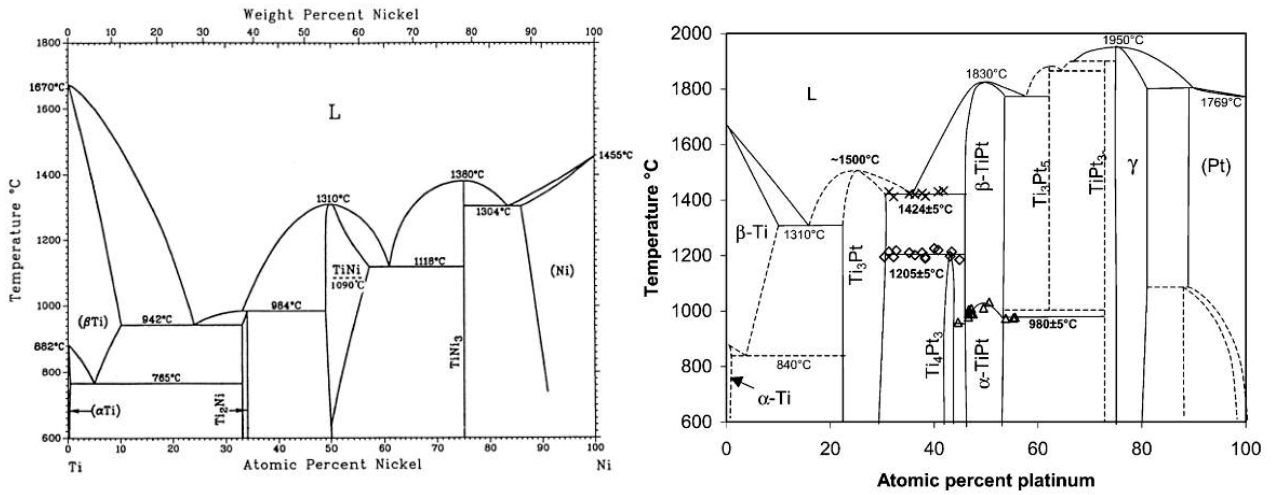


Figure 3-4 Phase diagrams (A) NiTi binary phase diagram from reference³⁷ (B) TiPt binary phase diagram from reference³⁸

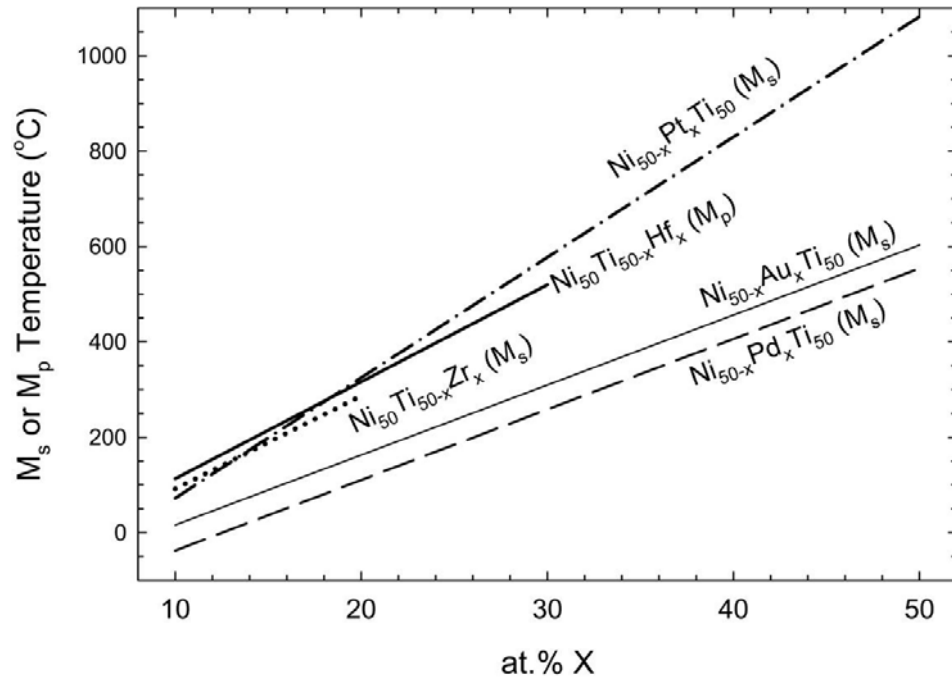


Figure 3-5 Effect of ternary alloying additions on the M_s (or M_p) temperature for NiTi-based high-temperature shape memory alloy systems.²

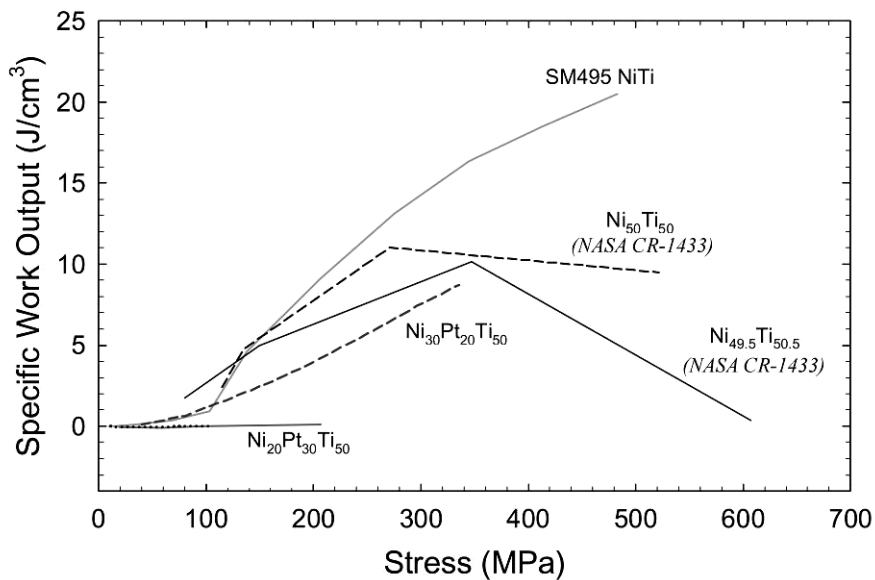


Figure 3-6 Comparison of the specific work output for several conventional NiTi alloys, SM495 NiTi, and the (Ni,Pt)Ti HITSMA³⁵

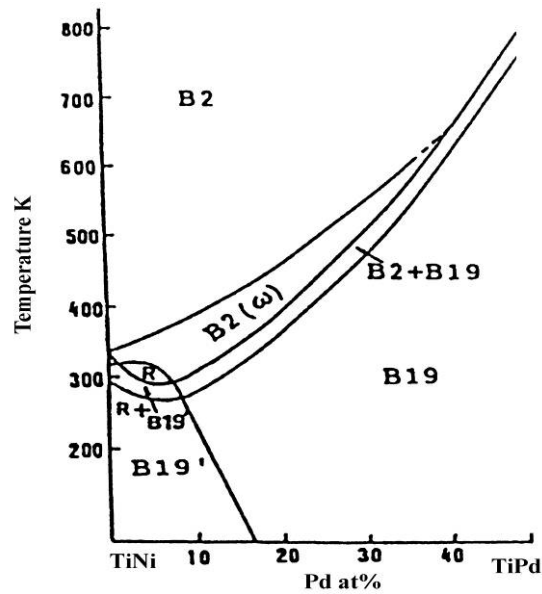


Figure 3-7 Phase diagram of $\text{TiPd} \pm \text{TiNi}$ alloys.⁴⁴

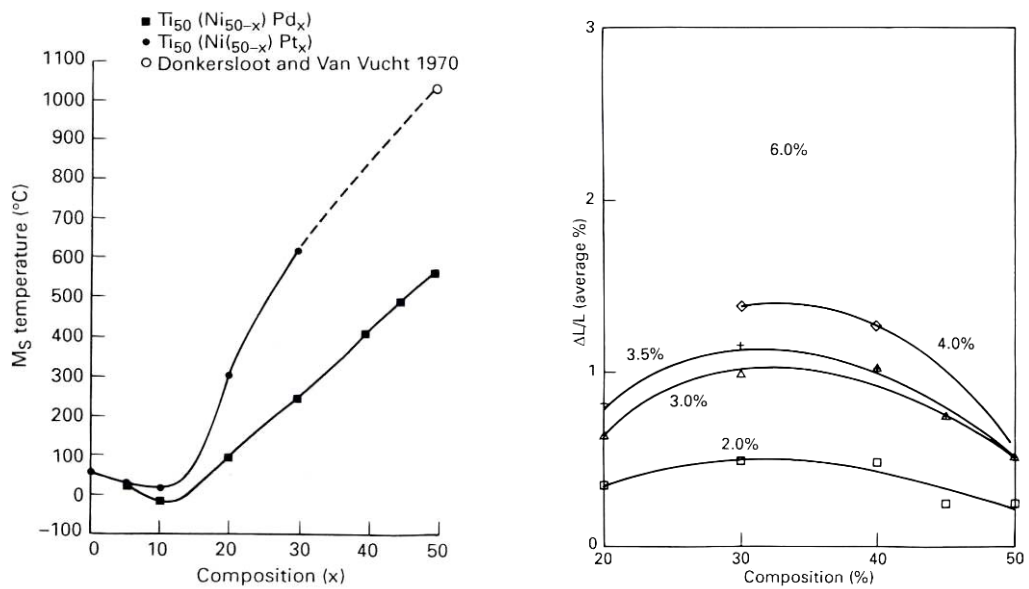


Figure 3-8 Shape memory properties NiTiPd (A) Ms temperature resulting from ternary alloy additions.¹¹ (B) Average shape recovery in $\text{Ti}_{50}(\text{Ni}_{50-x}\text{Pd}_x)$.¹¹

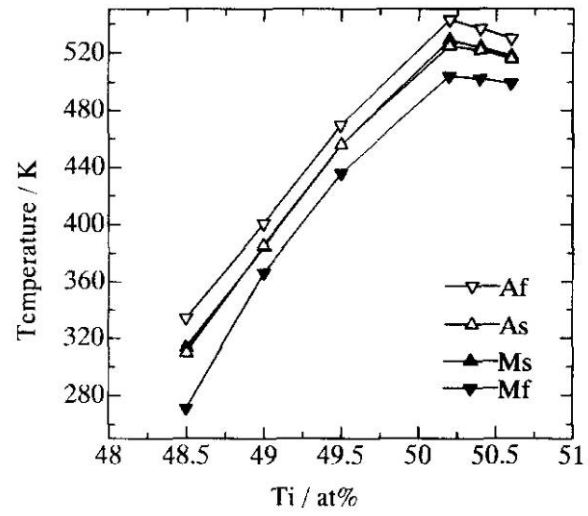


Figure 3-9 Plots of martensitic transformation temperatures vs. composition for $\text{Ti}_{50-x}\text{Pd}_{30}\text{Ni}_{20+x}$.⁴⁷

CHAPTER 4 RESULTS AND DISCUSSION

Shape memory alloys have unique properties and related mechanical behaviors. Principally, they have the ability act as a solid state device which performs mechanical work against a biasing load. In order to examine this extraordinary behavior an in-depth thermomechanical study of these two alloys is conducted. A comparison between the two systems is carried throughout this chapter with the main focus on the $\text{Ni}_{19.5}\text{Ti}_{50.5}\text{Pd}_{30}$ high temperature shape memory alloy in comparison to the $\text{Ni}_{24.5}\text{Ti}_{50.5}\text{Pt}_{25}$ alloy.

Heat Treatment Optimization

Before testing the baseline $\text{Ni}_{19.5}\text{Ti}_{50.5}\text{Pd}_{20}$ and NiTiPt alloys, it was necessary to determine an optimum heat treatment for the annealing of the as-machined samples to eliminate any residual effects due to the machining process that could affect the transformation temperature or thermomechanical performance of the alloy. The martensite phase in particular is susceptible to twinning/detwinning and or plastic deformation of the near surface layers of the alloy. The function of the stress relief heat treatment is to relieve any residual stresses in the samples due to the high speed machining and the thermal expansion mismatch between the mild steel extrusion can and the SMA. At elevated temperature interactions between dislocations generated during the machining process allow for the formation of low energy structures by dislocation movement.⁵² As an indicator of the residual stresses in the material resistive measurements are employed.

Resistivity is a stress sensitive property among other variables. A classic example of this effect is the increase in resistivity as a function of maximum precipitation hardening in aluminum 7XXX series alloys where the increase in resistivity is linked to an increase in the materials internal stresses due to precipitate matrix interactions⁵⁴. Additionally a materials stress state affects the relationship between temperature and resistivity or the slope of the resistivity temperature curve. The combination of these effects is the keystone for optimizing our stress relief heat treatments. For the purpose of these measurements it was assumed that the linearity of the resistivity vs. temperature curves is a function of the stress distribution in the sample. The underlying reasoning behind this was that if a non uniform stress distribution exists within the material a position dependent resistivity distribution will also exist. As the material is heated or cooled through a thermal hysteresis a fraction of these stresses are relieved resulting in an irregular resistivity temperature curve. A material which has been almost fully recovered on the other hand will exhibit a linear resistivity temperature curve due to the absence of the relief of residual stresses. Figure 4-10 shows the results of a heat treatment optimization for the 25 at% Pt modified alloy. In this examination the samples were heat treated for 1 hr at 500 °C and 600°C and heated through a thermal hysteresis with in-situ resistivity measurements post heat treatment along side a no heat treatment sample for comparison. The sample that did not have a heat treatment results in a resistivity temperature curve which is highly irregular due to the irregular transient stress distribution within the sample. The sample which was heat treated for 1hr at 500 °C (near A_f) showed a slightly more regular relationship due the partial stress relief during the heat treatment. Finally the sample which was heat treated at 600 °C showed a smooth

resistivity temperature curve which is indicative of a stable stress distribution within the material which may be linked to a fully recovered material.

Characterization

Materials Characterization

Each alloy was developed with a slightly Ti (approximately .5 at%) rich composition in order to maintain a stoichiometric or slightly Ti-rich matrix composition after formation of various interstitial containing phases. The alloying technique has been employed in previous studies of the Pt modified NiTi SMAs.³⁵ The resulting chemical compositions of the extruded materials are Ni 19.5, Pd 30.0, Ti balance, O 0.30, C 0.50 and Ni 24.419, Pt 24.428, Ti balance, O 0.28, C 0.43. Detailed compositional analysis of each extrusion is given in appendix C. SEM micrographs exhibit the phase contrast of the resulting alloy is shown in Figure 4-11 revealing a small volume fraction of possible carbide and oxide phases in a relatively homogeneous Ti Ni Pd and Ti Ni Pt matrix void of macro cracks and porosity.

Properties and Transformation Temperatures

The no-load transformation strain of the undeformed material was measured by dilatometric techniques. This technique measures macroscopic structural shape change or uniaxial transformation strain of the extruded material as a function of temperature. The thermal expansion coefficients of each phase (austenite and martensite) were determined from the slope of the linear portions of the temperature vs. strain relationships shown in Figure 4-12 and Figure 4-13. The samples were thermally cycled through several hysteresis in order to allow the transformation temperatures and strains to stabilize thus becoming reproducible on subsequent cycles. The forward and reverse reaction in the undeformed material exhibited equal magnitude transformational strains

under no load conditions. The thermal expansion coefficient of each phase within each alloy was approximately equal with the martensite having a slightly greater thermal expansion than that of the austenite with the NiTiPd alloy exhibiting the greater thermal expansion. These thermal physical properties are tabulated in appendix A.

Resistance measurement is a prominent characterization technique in the study of SMAs due to the substantial differences in the electrical properties between the parent and shear phases. This technique has been successfully applied to SMAs as a method of determining transition temperatures in-situ to operating conditions. In addition, the application design of SMA actuated active flow control devices requires an understanding of the temperature dependence of the electrical resistance. Researchers working on the Nitinol characterization study NASA CR-1433 utilized the resistance vs. temperature behavior of unconstrained NiTi in a scheme to quantify the shape memory performance of the material.⁵³ In the current study this technique was exploited for the determination of the transformation temperatures as well as the temperature dependent electrical properties of the SMA under study in the stress free state.

The temperature dependence of the resistivity is plotted in Figure 4-12 and Figure 4-13 including marked isothermal test temperatures. As mentioned in the experimental section the transformation temperatures are determined by constructing a tangent line to the linear portion resistivity temperature plot of each phase and a tangent line for the transformation intermediate region. The intersection of the tangent lines is determined as the transformation start and finish temperatures.

A slight discrepancy exists between the transformation temperatures measured by dilatometric and resistive methods. This slight discrepancy was linked to the methods used

to instrument the samples with a thermocouple. In the dilatometer the thermocouple was located a small distance from sample therefore this technique actually measures an average temperature between the region of the furnace adjacent to the sample and the sample. The transformation in the forward and reverse directions are highly exothermic and endothermic therefore during the transformation the difference in temperature between the sample and the furnace increases. This effect causes a slight error in the temperature reading at the thermocouple. The resistive measurement on the other hand circumvents this problem by having the thermocouple spot welded directly to the sample and therefore is a more accurate measurement of the transformation temperatures. A summary of the recorded transformation temperatures measured by resistive methods are tabulated in appendix B.

Similarly to the thermal expansion results the temperature dependence of the thermal resistivity coefficient of the martensite phase is greater than that of the austenite phase. The resistivity of the austenite is greater than that of the martensite at all temperatures within the experimental bounds. A metals resistivity is a stress and structure sensitive property thus a greater resistivity could be an indicator of a higher internal energy or stress state of a particular phase, which in this case is the austenitic phase. Ti vs. Ni, Pt or Pd have a significant mismatch in atomic radii, and thus the arrangement of these atoms into ordered B2 lattice results in internal lattice strains as atoms are forced to reside at slight distances from their minimum energy distance. The shear lattice on the other hand has greater distances between lattice positions resulting in a more relaxed structure and thus a lower resistivity.

In the Pd modified alloy there is a small but significant peak in the resistivity for the reverse reaction (martensite transforming to austenite). This peak occurs when a very small volume fraction of martensite remains in an austenite matrix. Focusing on the martensite/austenite interface and criteria for thermoelastic transformations which states that this interface must be coherent and the majority of the transformation strain between the phases must be accommodated elastically a correlation to a parallel well developed system is made. A comparison of such an arrangement to the mechanism for precipitation hardening which also initially has strains partially accommodated elastically due to lattice mismatch can be made. It is feasible to imply that there could be a significant elastic interaction in the Pd-containing SMA when very small fractions of martensite reside in an austenite matrix. Precipitation hardened materials exhibit an increase in resistivity as hardening resulting from elastic interactions between phases increases.⁵⁴ The evidence of this is the small peak in the resistivity curve and the implication that elastic interactions between the austenite matrix and martensite produces an increase in resistivity above that of the fully austenitic material. Comparing the mean correspondent variant pair size of the Pt and Pd modified alloys it is evident that the distribution is much coarser in the Pt than on the Pd alloy (Figure 4-11). As a result, it is expected that this coarse distribution near the end of martensite to austenite transformation results in widely spaced martensite packets which can not effectively harden the remaining austenite or globally effect its electrical resistivity thus Pt alloy does not exhibit the a resistivity peak.

Thermomechanical Testing

Isothermal Stress-Strain Behavior in Tension and Compression

To directly compare mechanical properties in tension and compression all the isothermal curves are calculated in true stress and strain. The representative true stress strain curves for tension and compression have been combined in to two sets of curves for each material in each loading orientation making a total of eight multi-experiment plots (Figure 4-6-Figure 4-18 and Figure 4-22-Figure 4-25). For each material, there is a plot combining (Figure 4-6-Figure 4-18 for NiTiPd and Figure 4-22-Figure 4-25 for NiTiPt) the stress strain relationship of the austenite and martensite well above or below transformation temperatures. Tension and compression behavior for the NiTiPd alloy is shown, respectively, in Figure 4-6 and Figure 4-7 for temperatures well away from the transformation temperatures while Figure 4-17 and Figure 4-18 contain the results of tensile and compressive isothermal tests near the transformation temperatures. The NiTiPt alloy tested at isothermal temperatures well above or below the transformation temperatures are shown in Figure 4-22 and Figure 4-23 while Figure 4-24 and Figure 4-25 include the mechanical properties near the transformation temperatures.

The elastic loading region of each uniaxial compression test was analyzed for linearity. Significant deviations from linearity in the elastic region are a good indicator of slightly non-parallel loading surfaces which result from a combination of machining imperfections, imperfect load bearing plenum faces and loading the sample slightly off axis. An example this effect is shown in Figure 4-14 where the elastic loading region below 3% engineering strain exhibits an experimentally induced deviation from linearity. If analysis revealed such a deviation from linearity the uniaxial compression test was

corrected by extrapolation of a regression analysis of the well behaved (linear) portion of the elastic loading region.

Although each isothermal compression test was carried out to over 30% engineering strain the results are presented only to 20% strain. Analysis of the force displacement curves revealed that friction between the load bearing plenums and the sample induced barreling. During a constant strain rate isothermal compression test an increase the slope of the force or engineering stress Vs displacement curve is indicative of significant frictional forces and the onset non-uniform deformation. This effect is exemplified by the monotonic compression test shown in Figure 4-14 at approximately the 22% strain level. Beyond the 22% strain in this example the slope of the force strain curve increases due to friction induced effects.

Isothermal stress-strain behavior in tension and compression NiTiPd

In the NiTiPd alloy well below the transformation temperatures in tension (Figure 4-6) the classical behavior of a thermal elastic shape memory is exhibited. The stress strain curve of the martensite at room temperature and at 200C exhibits three identifiable regions in the stress strain curve. These regions are (1) elastic deformation at lower stresses up until the lower yield stress or in the case of the martensite the detwinning stress (2) further loading results in an almost linear inelastic deformation resulting from detwinning of the martensite with continues until the variants with favorable orientations are reoriented resulting in pseudo stress strain plateau (3) the work hardening rate again increases, initially due to further elastic deformation of the re-ordered variant structure followed subsequently by further deformation of the martensite resulting in a more typical region of plastic deformation where the curve has a parabolic appearance.

In tension the pseudo stress strain plateau (region 2) differs from the stress strain plateau exhibited by classical SMA (NiTi) in that deformation does not occur at a near constant stress. The positive slope in this region indicates that a mechanism is requiring an increasing stress to continue deformation. Several mechanisms could produce such a result in an SMA. As described earlier in the alloy development section, one of the limitations of high temperature shape memory alloys is a low critical resolved stress for the onset of non-recoverable slip processes at least relative to the detwinning stress. Slip and the associated deformation motion and generation result in work hardening; thus could explain why the combination of slip and detwinning requires a progressively greater stress as the true strain increases. Although this is an important mechanism examination of the no-load recovery tests results examined discussed a later section show that it is not the dominant cause of the work hardening.

Another more plausible mechanism proposed here is based on the fact that there exists an orientation distribution of correspondent variant pairs. As mentioned earlier, the critical stress for detwinning, noted as the lower yield stress, is significantly lower than the actual yield stress for macroscopic yielding of the martensite primarily through dislocation motion (classical yield stress). Considering that in a typical multi-variant martensitic structure, certain variants are oriented favorably for detwinning which means the applied stress results in a maximum resolved shear stress. Variants which are oriented such that the resolved shear is a maximum will detwin first at the lowest applied uniaxial stress resulting in the bulk material exhibiting a yield stress. Variants which are misaligned are simultaneously deformed elastically as the resolved shear stress is smaller than the critical resolved shear stress for detwinning. As deformation increases at

increasingly greater stresses, more variants in other orientations are activated as the applied stress produces a progressively increasing resolved shear stress. Thus although detwinning is the main deformation mechanism in the pseudo stress-strain plateau the orientation distribution of these variants requires different applied uniaxial stresses for detwinning. However more work is necessary to fully confirm this mechanism.

In contrast, the isothermal deformation of polycrystalline martensite in a classical SMA, such as NiTi, occurs at a constant or near constant stress. Here, similarly to the NiTiPd extruded material, we also have a variant distribution which results in a comparable situation yet the classic SMAs do not exhibit this behavior. A likely explanation for this stems from the number of equivalent variants that can form from a single parent austenite crystal. Recall that the martensite phase in the NiTi SMA has a monoclinic structure in contrast the NiTiPd and NiTiPt alloys both of which transform from a B2 to the orthorhombic structure. The orthorhombic structure is a higher symmetry structure than the monoclinic. As a matter of fact a monoclinic structure in SMAs is related to the orthorhombic structure by an additional non-basal shear. This additional shear increases the number of equivalent variants by a factor of two which may form from a given austenite crystal. Thus, any particular variant has twice as many equivalent variants it can shear to under load. As a result, there is less of an orientation dependence of the shear stress for detwinning in the monoclinic structure as there are many more variants for a particular variant in a particular orientation to shear to thus in SMAs with a monoclinic martensite exhibit detwinning at constant or near constant uniaxial stress.

The mechanical properties of the NiTiPd martensite in compression (Figure 4-7) are comparable up to the initial yield stress. Beyond the yield stress, however (Figure 4-6) the deformation of the martensite does not exhibit a clear distinction between the deformation mechanisms of detwinning and non-reversible slip processes. Deformation of the martensite in compression after the yield stress results in a high work hardening rate to strains of about 10%. Further deformation again results in a decreasing work hardening rate similar to what is observed for a single phase alloy. The lower slope is linked to deformation via non-recoverable slip processes and is comparable in both tensile and compressive loading orientations. However, the isothermal behavior in tension and compression deviates substantially beyond the yield stress of the martensite phase. The tensile behavior exhibits a pseudo-stress plateau or low hardening rate at stress levels starting at about 250 MPa which is linked to favored martensite variants growing at the expense of the other martensite variants in contrast to the stress-strain relationship for compression which does not show a clear stress strain plateau. This indicates that the orientation of preferred variants requires an increasing stress suggesting a low mobility interface and thus a deformation mechanism which is different from the deformation mechanism in the stress plateau evident in the tensile loading mode.

Deformation by detwinning mechanisms is polar in nature, in contrast to slip behavior, such that a reversal in the shear direction will not produce twin movement in variants favorably aligned for operation in the forward direction.^{55, 56} In other words, twins aligned favorably for operation in compression will not operate under a tensile stress and vice versa. For monotonic testing of the martensite phase, the sample microstructure was set prior to testing. Apparently the manner in which the material was

processed (extrusion in this case) resulted in a more favorable variant structure for twinning/detwinning in tension than compression. Particularly if the variant orientation distribution is such that the variants which predominate the microstructure are already in the orientation at which the Schmid factor is at a maximum, deformation through detwinning assisted variant reorientation is not possible since there are fewer variants to shear over and join the growing variant. The evolution of a microstructure of such a variant distribution results in a material which is essentially partially detwinned as the product of the detwinning reaction is the formation of variants which already predominate the microstructure.

Well above the transformation temperature the mechanical properties of the austenite were comparable in tension and compression. The austenite exhibits a small linear elastic stress strain region up until the yield stress of the material. After the yield stress, the material exhibited a low work hardening rate which decreased with increasing isothermal test temperature as evident in comparison of the 300 °C and 400 °C tensile tests (Figure 4-15) and the 350 °C, 365 °C, 400 °C and 500 °C compression test (Figure 4-16).

The 400 °C tensile test sample exhibited a maximum in the engineering stress strain curve followed by a parabolically decreasing stress strain relationship. This is indicative of non-uniform deformation of the gauge length. Optical comparator measurements of the tensile sample confirmed that extensive necking occurred during deformation process which led to the formation of a slightly diffuse neck. In this sample uniform deformation reduced the cross-sectional diameter of the gauge length 4.72% from 3.81 mm to 3.63 mm while the neck region exhibited a 40.2% reduction and a minimum diameter of 2.28

mm. The true stress and true strain up to the point of necking was calculated from the engineering stress and strain using the constant volume approximation. The true fracture stress (1522 MPa) and strain (102%) were calculated from the minimum cross-sectional area of the necked region. The 400 °C curve combines the true stress and strain calculated from the engineering values and an extrapolation between the value at the onset of necking and the true fracture stress strain.

For the test results shown in Figure 4-17 and Figure 4-18, the samples were heated to well above the austenite finish temperature (A_f) and allowed to cool back to the test temperature before loading the sample. The process of heating significantly beyond the A_f and subsequently cooling back to the desired test temperature ensured that the resulting stable phase was that of austenite. In-situ resistivity measurements and the occurrence of a well defined stress plateau, indicate that upon loading, a stress induced martensite results. This behavior can be seen in detail in Figure 4-19, which is a superimposed plot of resistivity, determined in-situ during tensile testing at 255 °C with the stress - strain curve. Both in tension and compression the relative amounts of stress induced martensite as well as the stress at which the transformation occurred were comparable. Finally, a ductility minimum was observed in the region where the stress induced martensite occurred, similar to the behavior reported in NiTiPt high temperature shape memory alloys.³⁵

The combination isothermal stress strain resistivity curve shown in Figure 4-19 exhibits a clearly visible stress strain plateau which results from the parent austenite phase isothermally transforming under stress to the martensitic shear structure. The deformation mechanism in this case is not detwinning nor dislocation motion, rather

deformation occurs by the transformational shear strain associated with the thermoelastic transformation. Initial deformation correlates an increase in resistivity with the elastic loading of the austenite, after which a stress induced transformation begins. Recalling the no-load resistivity hysteresis measurements (Figure 4-12) it was shown the resistivity of the martensite is much lower than that of the austenite. Therefore as the austenite transforms to martensite indicated by the stress plateau, the resistivity decreases with increasing fractions of martensite. With continued strain elastic then plastic deformation of the stress induced martensite and remaining austenite occurs and as expected results in an increase in resistivity. A final change in the work hardening rate is accompanied by a subsequent change in the slope resistivity strain relationship.

Another interesting feature of the stress strain plot (Figure 4-20) for stress induced transformations in compression is that the stress at which the austenite is forced to transform increases with increasing deviations from the no-load transformation temperatures. This can be correlated to the fact the chemical driving force opposing the non-chemical driving generated by the applied stress is greater at increasing deviation the load free transformation temperatures. Additionally the extent of the stress induced transformation and the resulting amount of strain generated by it decreases with increasing deviation from the no-load transformation temperature. At temperatures much higher than the no-load transformation temperature ($T \gg M_d$) it is not possible to form stress induced martensite as the stress required for this to occur is higher than the yield stress of the austenite which results in deformation by non-recoverable slip processes.

The temperature dependence of the yield stress in compression and tension shown in Figure 4-20 is determined from the proportional limit from the above series of

isothermal stress strain curves. Generally, the yield stresses in tension and compression were similar at a given temperature. The yield stress of the martensite decreased with increasing temperature and reached a minimum at the transformation temperature where the formation of stress induced martensite was possible. Beyond this minimum the alloy was partially or fully austenitic and the yield strength increased significantly with increasing temperature until a peak near 350 °C. At temperatures above 400 °C the austenite weakened and the onset of slip occurred at lower stresses.

Dynamic elastic modulus determination NiTiPd

In order to have an accurate representation of the instantaneous, load free, elastic modulus of these materials as a function of temperature, a dynamic modulus test was conducted for the NiTiPd alloy. The temperature-modulus relationship is plotted in Figure 4-21, which has three main approximately linear regions corresponding to the fully martensitic or austenitic phase or a combination of both in the intermediate temperature range bound by the reaction start and finish points. The dynamic modulus of the martensite is about 10 GPa higher than that of the austenite. The martensite as the sample temperature has an inverse relationship to elastic modulus. Converse to this relationship the modulus increases with temperature for the fully austenitic material suggesting that the internal energy resulting from atomic interactions of this phase is increasing with increasing temperature up to 800 °C. The region bound by the transformation temperature exhibits a stronger temperature dependence than does either of the single phases which is proportional the reaction progression terminating at a minimum at the transformation finish temperature. At this point the material is fully austenitic and modulus value is that of the austenite at the transformation temperature. An important characteristic of thermoelastic transformations is pre-martensitic elastic

softening. This effect is clearly exhibited by the NiTiPd alloy as evident in the elastic modulus increasing with increasing temperature. Pre-martensitic elastic softening allows for local transformation strains adjacent to the interface to be accommodated elastically at a lower stress.

Isothermal stress-strain behavior in tension and compression NiTiPt

The NiTiPt alloy martensitic stress strain curves deformed isothermally well below the transformation temperatures in tension and compression did not exhibit any of the clearly distinguishable characteristics of a “typical” shape memory alloy. This alloy does not exhibit a defined stress plateau. Initial loading both in tension (Figure 4-24) and compression (Figure 4-25) resulted in a linear region as the alloy is elastically loaded (linear elastic region). Similarly, upon loading in tension or compression past the yield stress there is a change in the slope of the stress-strain curve. However, the tensile samples fracture shortly after the yield stress. From no-load recovery experiments detailed in a subsequent section on this alloy, we know that partial detwinning along with slip is occurring at strains past the yield stress therefore, the second region will be denoted as the detwinning region, following the nomenclature for conventional SMAs. The ductility in tension at the test temperatures averages at about 2.5% while in compression the samples either fractured slightly before 20% strains or were unloaded when excessive bulging became evident. Similarly to the NiTiPd alloy in compression, this alloy exhibited a second change in the work hardening rate in the 10% strain range. Although a clear correlation to the deformation mechanism has not been determined it is possible that changes in sample geometry from uniform deformation to sample bulging in addition to slip result in such a change in slope.

As in the NiTiPd alloy, a ductility minimum was evident in tension at temperatures in the range of the transformation temperatures. Furthermore the all the martensitic alloys failed in a brittle manner without any visible necking. Most of the fractures seemed to initiate at a surface defect (spot weld sites) or macroscopic inclusions visible to the naked eye. Further microstructural characterization is required to fully characterize the fracture mechanism in this alloy. Analysis of the fracture stress and fracture strain at each isothermal test temperature (Figure 4-28) reveals two distinct regions. Starting at 200°C as the temperature is increased the fracture stress and fracture strain decrease until a minimum is reached. Above this point all the samples tested are fully austenitic and as the isothermal test temperature is increased further the fracture stress decreased at a slightly less negative rate while the fracture strain sharply increases. The fracture stress in the austenitic phase decreases with increasing temperature due to dynamic recovery becoming more prevalent while the fracture strain possibly increases due to the high strain rate sensitivity of this phase as previously explored in Figure 4-26.

Isothermal tests for well above the transformation temperatures in the fully austenitic state in tension (Figure 4-22) and compression (Figure 4-23) have similar characteristics to the stress strain curves of NiTiPd alloy. Primarily there was elastic loading of the austenite up to the yield stress followed by plastic deformation. At higher temperatures dynamic recovery in the martensite was clearly evident. In order to explore the effects of dynamic recovery two tests were conducted in tension at 550C, one test was run at the standard strain rate while the second test was run at a strain rate increased by a factor of 10, the results are shown in Figure 4-26. This test confirmed that dynamic recovery was in fact a dominate mechanism affecting the mechanical properties of the

austenite and furthermore the austenite was quite strain rate sensitive although further testing is required to quantify the strain rate sensitivity. This is important for subsequent studies on the advanced thermomechanical processing of these alloys for actuation applications.

The yield strength in both tension and compression in this alloy also overlap quite well as shown in Figure 4-18. This indicates that the onset of the combination of detwinning and yielding are similar in both tension and compression. Similar to the NiTiPd alloy the yield strength drops at temperatures in the range of the transformation temperatures followed by a sharp increase. A sharp decrease in the yield strength of the austenite occurs at temperatures above the A_f in which the yield strength of the austenite drops over $\frac{1}{4}$ its initial value. This is due to thermal energy helping overcome the activation energy for dislocation motion. Contrasting to the yield strength vs. temperature relationship of the NiTiPd SMA in this alloy the yield strength of the martensite is less than 100MPa of the austenitic yield strength while in the NiTiPd alloy this difference in strength is over 200MPa.

An important characteristic of viable SMA materials for actuation applications has been linked to mechanical properties of the austenite vs. those of the martensite. Primarily, experience has shown that for an SMA material to be a good candidate for actuation applications the alloy the austenitic phase should be mechanically stronger than the martensite in order to avoid non-reversible slip in the austenitic phase. This is clearly the case in the NiTiPd alloy yet the strength of the martensite is comparable to the strength of the austenite in the NiTiPt alloy. Furthermore, stress induced transformations did not occur in this alloy at any temperature tested as confirmed by in-situ resistivity

measurements which is thought to be primarily because of the high shear strength of the martensite.

Unconstrained Recovery Tests

Unconstrained recovery tests are used to characterize the ability of a shape memory alloy to recover twinning-induced deformation that is introduced at temperatures below the martensite finish temperature (M_f) by heating the material through its transformation temperature. The shape recovery is commonly determined by measuring the amount of strain introduced into a sample during deformation below the M_f , heating and cooling the sample through a full hysteresis back to room temperature.^{47-51, 59-62}

Unconstrained recovery tests NiTiPd

The final dimensions of the sample are measured and compared to the initial dimensions to calculate the amount of strain recovered. However in monitoring the strain changes continuously during this process as shown in Figure 4-29, it is clearly evident that a number of different mechanisms are acting to contribute to the overall strain recovery of NiTiPd alloys as first reported by Lindquist.¹¹ For comparison to prior work, the total recovery of this alloy is plotted vs. initial plastic strain in Figure 4-30 Total Recovery. The various contributions to the load free strain response of an alloy heated from 100°C to 400°C then finally cooled back down to 100°C is shown in Figure 4-29. Upon unloading the sample partially recovers a portion of the strain elastically often termed the elastic spring back; however, although this region of the recovery curve is often included in the analysis of an SMA's total recovery it in itself is not a true SMA characteristic as the underlying mechanism is not a consequent of a thermoelastic transformation. The strain recovery processes for the load free material occurs in three distinct reactions. 1.) The thermal expansion coefficient of the deformed martensite

shown originally in Figure 4-12 was smaller than that of the undeformed martensite.

Continuous shape recovery begins on heating up to the A_s temperature and the amount of recovery is estimated from the differences in the slope (thermal expansion coefficient) of the deformed and undeformed martensite expansion curves. The mechanism behind this difference may be that due to the rearrangement of twins during detwinning as the material is deformed. Consequently, the expansion characteristics along this one direction may no longer be the same as measured in an undeformed sample with a more randomly oriented martensite (Figure 4-12). Further microstructural and experimental work is needed to confirm this mechanism.

2.) The majority of the strain is recovered in a stepwise reaction which occurs during heating from the A_s to the A_f temperatures. The strain response in this region is attributed to two competing mechanisms. First and foremost is the recovery of strain by the transformation of the detwinned martensite to austenite. Opposing this is the transformation strain associated with transformation from martensite to austenite (depicted in Figure 4-12) which is measured along the deformation axis.

3.) There is a small amount of strain recovered as the sample is cooled between the M_s and M_f . This strain is linked to the austenite to martensite transformational strain however it is not equal to this transformation strain. As shown in Figure 4-29 this portion of the recovery is dependent on the initial strain applied to the martensite. A possible mechanism proposed here is based on nucleation of a preferred orientation of martensite on cooling due to the dislocation structure which forms during deformation. Initially the martensite is strained to low levels and the majority of the deformation is accommodated by detwinning which is reversible. As the amount of strain in the martensite is increased there is an increasing amount of plastic deformation along with detwinning. Since at lower

strain levels the martensite is detwinned with little plastic deformation the majority of the strain is recovered in the martensite to austenite reaction. Upon cooling through the austenite to martensite reaction a small amount of strain is recovered due to the formation of a random distribution of correspondent variant pairs (CVP). When strain levels are sufficiently large to produce significant amounts of plastic deformation, detwinning is recovered during the martensite to austenite reaction yet plastic deformation associated with dislocation motion is not recovered and is carried over into the austenitic structure. This remnant dislocation network could affect the distribution of correspondent variant pair such that particular orientations are preferred resulting in a lower amount of recovery in comparison to a structure with a lower dislocation density and a more random distribution of CVP. Further microstructural examinations of samples thermally cycled after varying amounts of strain could possibly confirm this mechanism.

The unconstrained recovery tests were conducted at several strain levels and the recovery levels were analyzed. A summary of the results are plotted in Figure 4-30 Total Recovery and Figure 4-31. The relative amount of recovery for the individual steps in the process are plotted vs. the total initial plastic strain which is defined as the amount of strain remaining after the load is removed. Four curves are shown in Figure 4-31 representing the three shape memory recovery components described above as well as the percent total recovery which is calculated from the initial plastic strain and the strain after cycling through a complete hysteresis. The values of recovery strain used in the calculations are corrected for thermal expansion data attained by dilatometric methods.

The conventional shape memory performance in this alloy is average. This material exhibits full recovery up to total strains of 2% and 98% recovery at 3% initial

strain which drops off linearly to 86% recovery at 5% total strain (Figure 4-30).

Although it is useful to analyze the total recovery in order to characterize an alloy's shape recovery, several contributing mechanisms are active. Therefore, in this study, an analysis of the temperature-dependent recovery was of interest. Analysis of these results shown in Figure 4-31 reveals that for low initial plastic strain, the alloy exhibits complete recovery (curve A) with a significant portion of the recovery occurring during the cooling reaction, evident in curve C, in addition to thermal recovery during the heating of the martensite (curve D). As the initial plastic strain is increased, the total recovery decreased (curve A) as does the recovery from the cooling reaction (curve C). The thermal recovery and recovery during the austenite to martensite reaction shown in curve C and D respectively both exhibit an inverse relationship to the initial plastic strain, which may be linked to increasing amounts of non-recoverable slip. This relationship (curve C) indicates that the randomness in variant orientations is decreasing with increasing strains, providing evidence of a preferred orientation resulting from the formation of dislocation networks. This effect in part contributes to the training of shape memory alloys where the generation of sessile dislocation networks causes the formation of a preferred martensitic variant orientation in the austenite to martensite reaction.

Unconstrained recovery tests NiTiPt

The NiTiPt alloy behaved similarly to the Pd-modified alloy in unconstrained recovery tests. The overall performance in shape recovery is comparable to that of the Pd alloy at lower strains and is slightly lower as initial strain levels increase. Again, there are three main identifiable regions attributed to several mechanisms contributing to the total shape recovery as shown in Figure 4-33. One distinguishable difference in this alloy is the sharpness of the phase transformation. The NiTiPd alloy, like traditional shape

memory alloy have a narrow hysteresis (Figure 4-32) in contrast to the NiTiPt alloy in which the recovery attributed with the forward and reverse shear phase transformations occurs over approximately 100 degrees Celsius. An interesting behavior in this alloy is that at low initial strains there is no recovery associated with the martensite to austenite transformation yet the material totally recovers after a full hysteresis.

Approximately 80% of shape recovery is attained during the austenite to martensite transformation which is significantly greater than that in the Pd alloy. Similarly to the Pd modified alloy this effect quickly drops off as slip becomes more prevalent. What makes this result interesting is that, although it is known that at low strain levels the martensite is being deformed completely by detwinning as is evident in the total recovery observed, there is no significant recovery associated with the martensite to austenite reaction. A qualitative explanation proposed here links this effect to the simultaneous recovery of the detwinned martensite which is counteracted by the transformation strain which was measured by dilatometric techniques.

Constant-Load, Strain-Temperature Tests and Work Output

A significant amount of research has been performed on unconstrained shape recovery of NiTi-30Pd alloys, yet no investigations on the materials ability to perform work have been reported. This shape memory alloy specific material property is a fundamental design parameter in actuation applications. The primary application identified for high-temperature shape memory alloys such as NiTiPd and NiTiPt would be for use as solid state actuator materials where work output (or the ability of the material to recover strain against some biasing force) is the primary consideration. Therefore, characterization of the work output is required for these alloys to advance from the development stage to real world applications. Consequently, load bias testing

was performed on the NiTiPd and NiTiPt alloys in order to quantify the work output as a function of the applied stress.

Constant-load, strain-temperature tests and work output : NiTiPd

Load bias testing was applied to the NiTiPd alloy as a method of measuring its specific work output as a function of the applied stress and mode of application (uniaxial tension or compression). A series of constant load tests were conducted in tension (Figure 4-34) and compression (Figure 4-35). Strains are plotted as a function of temperature for each applied stress. During each test, the resistivity of the sample was continuously monitored and recorded although these results will not be included here as analysis revealed that this portion of the measurement provided no additional information during load bias testing. Essentially, the temperature vs. resistivity relationship paralleled the temperature vs. strain relationship.

Measurements of the transformation strain used to calculate the work output are taken from the second thermal cycle through a complete hysteresis under load, due to the formation of a preferred orientation distribution of correspondent variant pairs that forms. In order to describe this effect and why measurements are taken on the second cycle the details of Figure 4-36 are described here, which is representative of all the high temperature shape memory alloys included in this study.

Figure 4-36 shows the temperature vs. strain relationship for the entire thermomechanical path which includes loading, the first two thermal cycles and, finally, unloading. Initially, the sample was loaded to the test stress at room temperature which is identified as region 1 in Figure 4-36. During this phase of the experiment the martensite material is composed of a nearly random orientation distribution of correspondent variant pairs and deformation is accommodated by detwinning the

martensite. The sample was then heated under load marked as region 2. During the first heating cycle, as the alloy transforms from martensite to austenite there is a small increase in strain. After reaching the maximum test temperature the sample is allowed to cool through the transformation temperatures (region 3). During cooling through the transformation temperatures (austenite to martensite) a large transformation strain occurs which mostly results from the formation of a highly directional distribution of correspondent variant pairs under the applied stress. This is an important mechanism because the orientation distribution in the martensite is not the same as the distribution in the undeformed material. Under the applied stress, the variants orient themselves such that their alignment increases the transformation strain. This is comparable to the product of detwinning a random martensite distribution where the applied stress causes certain variants to be favorable over others. The material is essentially detwinned with one significant difference. Principally, the stress required to produce a detwinned structure is much lower when transforming the material under load than by deforming the martensite isothermally. This is clearly evident by comparing the amount of deformation attained during the isothermal loading of the martensite denoted by region 1 to the amount of strain which results during the phase transformation under load. During the first thermal cycle, the strain in the sample due to the initial applied load at room temperature was smaller than when the sample was cooled through the martensite temperature to room temperature under load.

During the second heating cycle (marked as region 4), the martensite is transformed to austenite which results in the recovery of a significant portion of the transformation strain which occurs during the forward reaction (region 3). It is important to note that the

transformation strain during the second heating cycle (region 4) is significantly greater than the same reaction on the first heating cycle (region 2). As the martensite transforms to austenite the material exhibits a change in strain against the biasing load, therefore, work is performed and the strain measured on the second heating cycle is used to calculate the transformation strain.

Additionally, these alloys do not exhibit full recovery of the transformation strain as evident from comparison of the change in strain marked in regions 3 and 4. The difference in strain is termed the open loop strain. This is due to non-recoverable slip processes which occur alongside the shear transformation. Referring back to the isothermal uniaxial thermal mechanical test (Figure 4-20), it was clear that the martensitic yield stress exhibits a minimum in the vicinity of the transformation temperatures. Apparently, the martensite is deforming partially by slip during the austenite to martensite transformation as evident in the differences in transformation strain. One possible reason as to why these alloys seem to slip during the transformations stems from the fact that the martensite austenite interface contains a high interfacial stress resulting from the shear transformation. Adjacent to the interface, the material exists at a higher stress, therefore, application of external stresses can cause this interface to surpass the stress level required to initiate plastic deformation and the material slips. During thermoelastic recovery, the plastic deformation is not recovered and is carried over to the next cycle.

Referring back to Figure 4-34 and Figure 4-35, the biasing load and specific work output are given next to their respective temperature strain plot recorded during the second heating and cooling cycle. Note that the engineering strain values are offset in

order to include the entire data set on a single strain axis. Generally, the transformation strain is a function of the biasing stress. Additionally, the thermodynamics thermoelastic transformations force the equilibrium transformation temperatures to change with applied stress which is evident in both figures. In compression at stresses greater than about 400MPa, thermally activated slip becomes more prominent and the material deforms continuously at temperatures past the A_f which is exemplified in Figure 4-35 at 687MPa.

A plot of the biasing stress dependent specific work output and transformation strain are shown in Figure 4-37 and Figure 4-38. The work outputs in tension and compression as a function of stress were similar. The specific work output increased with increasing stress level, with a maximum work output of about 12 J/cm^3 attained by interpolation at approximately 500 MPa, and then began to decrease with further increases in stress. This peak is evident from the compression data since the tensile data reached a maximum just before the peak but was actually limited by fracture of the sample during testing. The stress dependent behavior of the specific work output stems from the transformation strain which also initially increased with increasing applied stress up to a maximum before decreasing. The transformation of high symmetry cubic phase to a lower symmetry orthorhombic phase has the freedom to produce many possible equivalent variants whereas the detwinning of martensite can occur through a limited number of detwinning reactions producing fewer equivalent variants⁶¹. Thus, whereas the detwinning of martensite is strongly isotropic, the formation of equivalent martensite variants from the austenite phase is dependent on the applied external stresses. The applied stresses has a distinct effect on the distribution of variant orientations that form during the austenite to martensite reaction. Tests conducted in tension contained a

variant structure that was optimized during the phase transformation for tensile loading while tests conducted in compression contained a structure optimized for compressive loading.

The work output stress behavior of the NiTiPd was similar to that observed in conventional NiTi alloys. Conventional NiTi alloys also exhibit a peak in the work output stress behavior with maximum values of 10 - 20 J/cm³.^{41, 46} This peak in work output is due to competing factors. Primarily, as the applied stress increase it prevents complete recovery of the transformation strain during the martensite to austenite reaction which causes the transformation strain to reach a maximum. Therefore, even though the applied stress is increasing, the transformation strain during the heating cycle begins to decrease. The product of the applied stress and transformation strain is work output which reaches a maximum at a particular stress level.

The mechanism as to why the transformation strain reaches a maximum has not been clearly identified yet two significant contributions have been found. Initially, as the biasing stress increases it forces the transforming austenite to form a less random distribution of variants and thus the transformation strain increases. Second, as the biasing stress further increases, it also causes non-reversible slip to occur during the forward and reverse transformations. During the austenite to martensite transformation slip occurs which results in an increasing amount of strain during the transformation. Similarly, in the reverse reaction (martensite to austenite) the oriented martensite variants transform to the parent austenitic phase which results in the decrease in the total sample strain. As this transformation occurs, the alloy may simultaneously slip which results in a decrease in the transformation strain against the biasing load. Both slip processes

contribute to the total open loop strain by increasing the transformation strain associated with the austenite to martensite reaction and decreasing the recovery strain associated with the austenite to martensite reaction. A summary plot of the open loop strain as a function of applied biasing stress is given in Figure 4-39 and confirms these observations. The open loop strain increases with increasing load thus causing the transformation strain and thus the work output to reach a maximum.

Constant-load, strain-temperature tests and work output: NiTiPt

Load bias testing was also performed in compression on the NiTiPt alloy shown in Figure 4-40. Compression was chosen since the results for the NiTiPd load biasing tests in tension and compression showed that the work output in both loading schemes was comparable. This alloy behaved similarly to the NiTiPd alloy, with the exception that the work output was significantly lower at all biasing stresses. In line with the results for the NiTiPd alloy the NiTiPt alloy exhibited a maximum in the transformation strain and stress which are shown in Figure 4-41 and Figure 4-42, respectively, which implies that similar deformation mechanisms occur in the NiTiPt alloy. The applied stresses which correlate to the maximum transformation strain and work output closely match the stress at which the maximums were observed in the NiTiPd alloy.

In contrast to the NiTiPd alloy at very high stresses the transformation strain and work output essentially drop to zero. Although we know the transformation is not completely suppressed by the applied stress which was determined by resistive measurements and by monitoring the power required to maintain a constant heating rate through the endothermic transformation, there was no significant recovery strain during the forward and reverse reactions. A plot of the open loop strain is shown in Figure 4-43 which is similar to the NiTiPd alloy at low stresses. Further increases in the load biasing

stress causes the open loop strain to decrease signaling that the material has work hardened sufficiently such that the majority of the stress is being carried by sessile dislocation networks and not elastically by the martensite or austenite. Further experimental work is required to confirm this implication which is based on the following argument. A shape memory alloy which is loaded below the stress required to initiate slip carries most of the load elastically. Even if the material is detwinned the majority stress is carried elastically. As the material shears from one structure to another there is a strain change associated with the orientation and displacement of the new structure. Now, if the alloy is loaded well above the yield strength where a significant amount of plastic deformation has resulted in work hardening, the load is being carried mostly by dislocation interactions. Microstructural studies have shown that dislocations remain sessile in the parent and shear phases in thermoelastic transformations. Therefore, since there is little dislocation movement during the transformation a transformation strain is not observed.

Prior studies have shown for a shape memory alloy to perform with a high work output under a biasing load, the strength of the austenite should be significantly lower than the detwinning stress of the martensite as measured by isothermal uniaxial testing methods³⁵. The current study confirms this result by the comparison of two alloys in similar alloy systems. In the NiTiPd alloy which performed better under a biasing load, the difference in strength between the martensite and austenite is greater than in the NiTiPt alloy. Comparing the alloy explored here with a Ni₂₀Ti₅₀Pt₃₀ alloy also subjected to load biasing in a prior study, the strength of the martensite was greater than that of the

austenite and the material exhibited no capacity to perform work. This is an important confirmation of a critical observation in the advancement of shape memory alloy design.

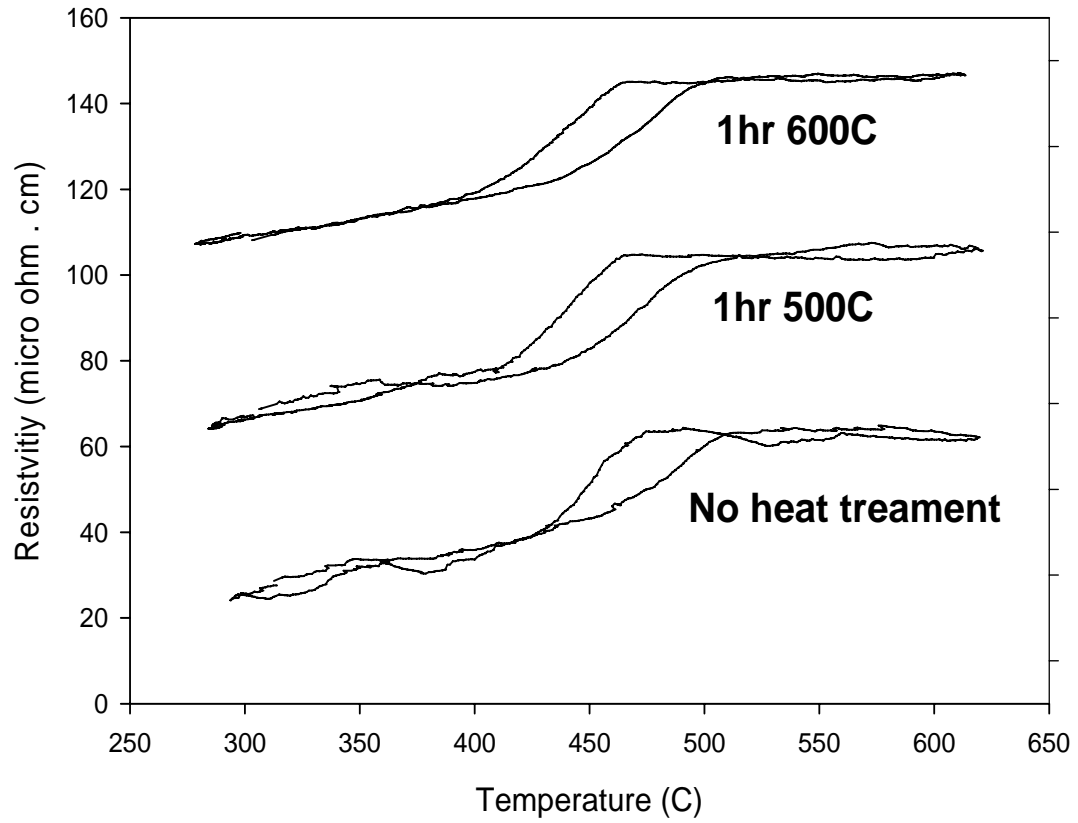


Figure 4-10 Stress Relief Heat Treatment Optimization by Analysis of Resistivity Temperature Profiles (note the resistivity curves are offset for convenience on the same resistivity scale).

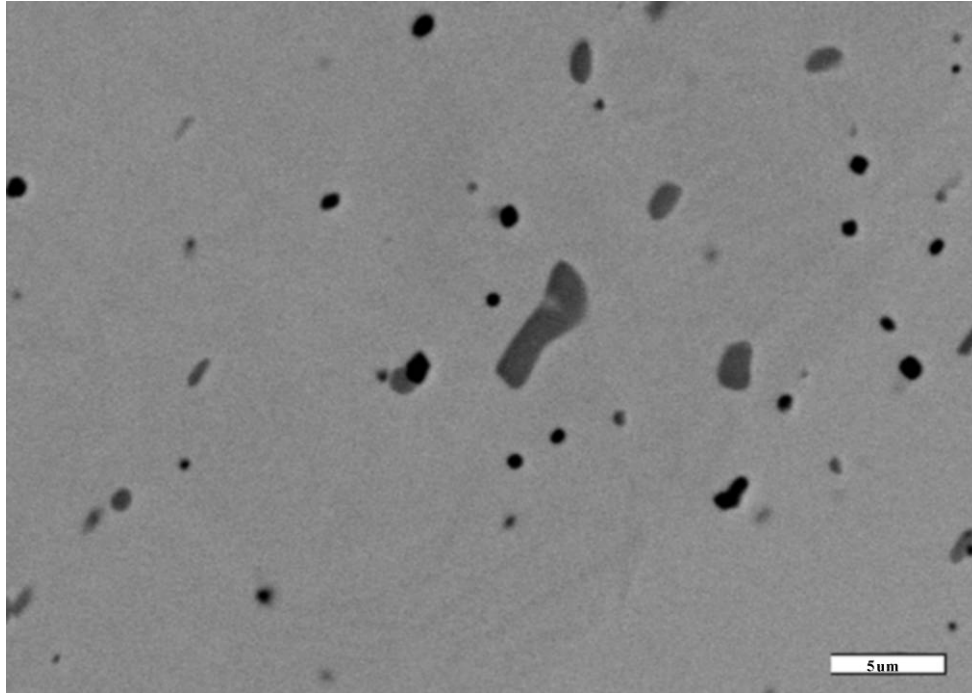


Figure 4-11 SEM BSE image of extruded $\text{Ni}_{19.5}\text{Ti}_{50.5}\text{Pd}_{30}$

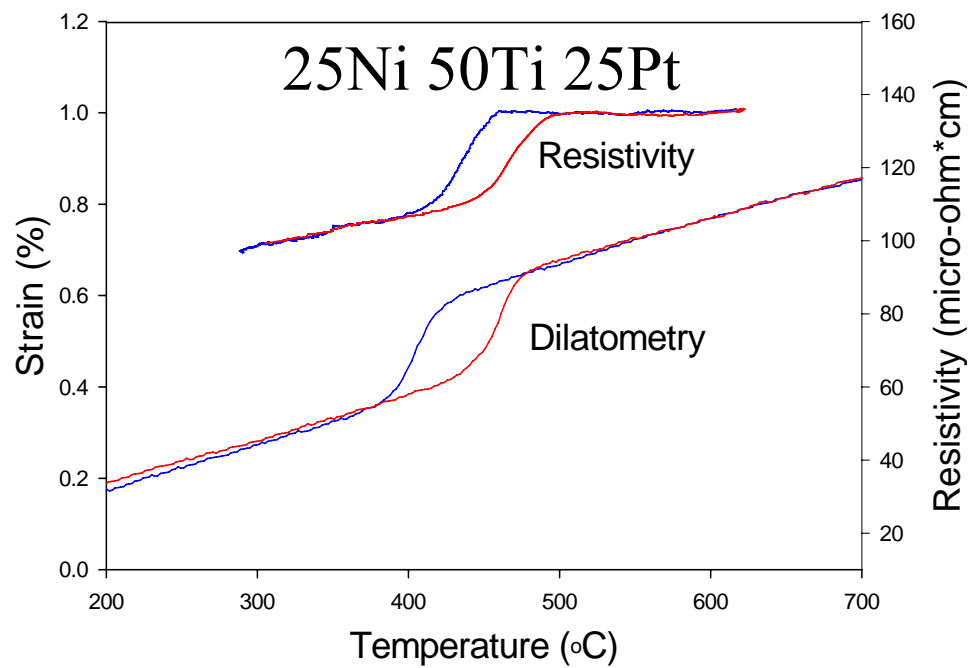


Figure 4-12 NiTiPt Resistivity and Dilatometry Test Results

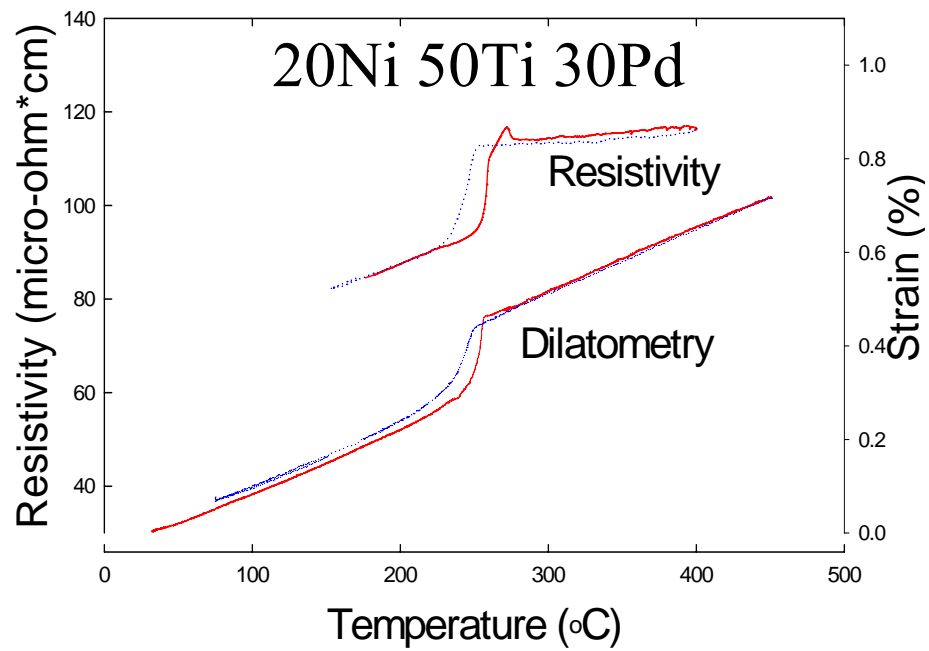


Figure 4-13 NiTiPd Resistivity and Dilatometry Test Results

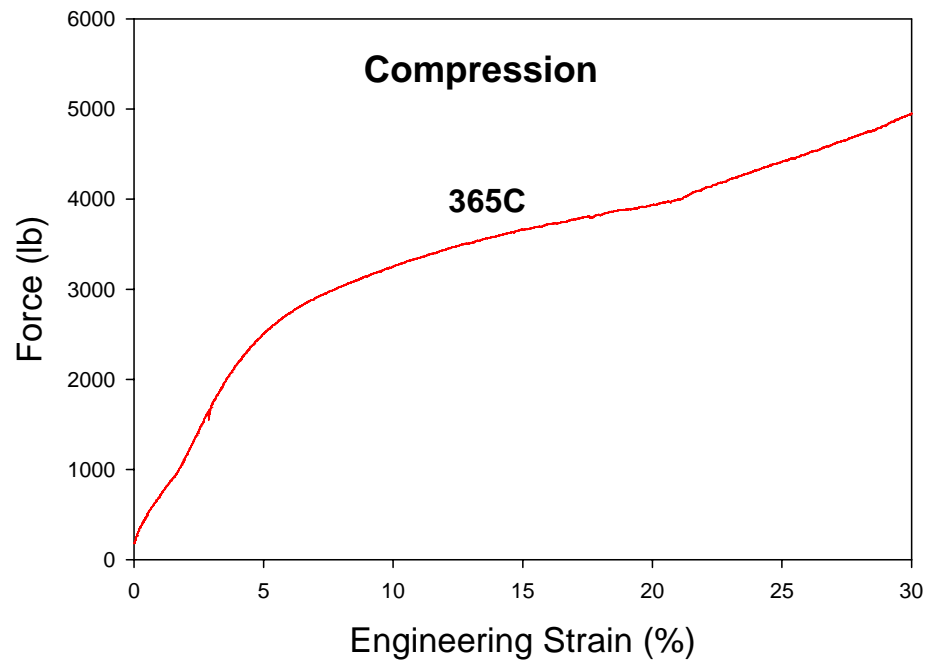


Figure 4-14 NiTiPd Force Strain Curve at 365°C

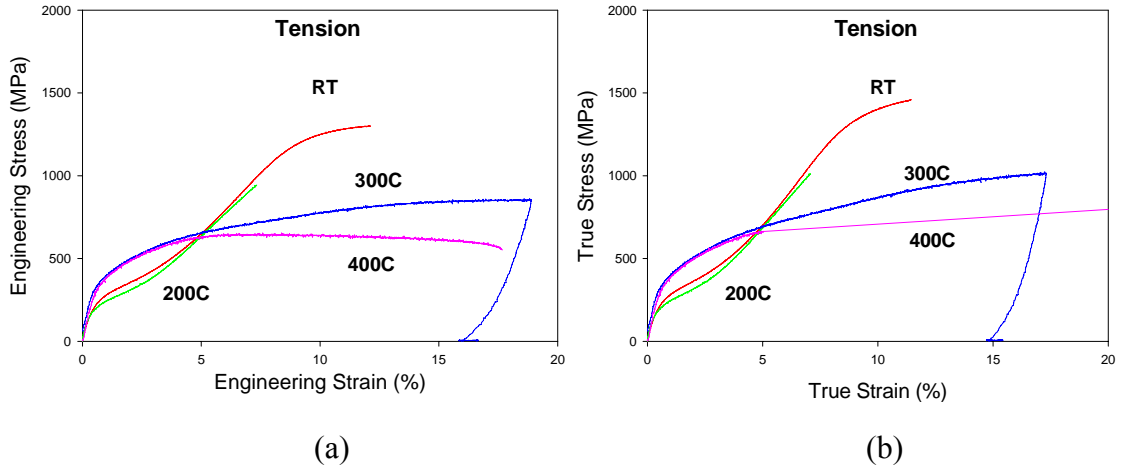


Figure 4-15 NiTiPd Alloy Uniaxial Isothermal Tensile Tests at RT, 200°C, 300°C and 400°C (a) Engineering Stress Strain Curve (b) True Stress Strain Curve including correction for non-uniform deformation of the 400C sample

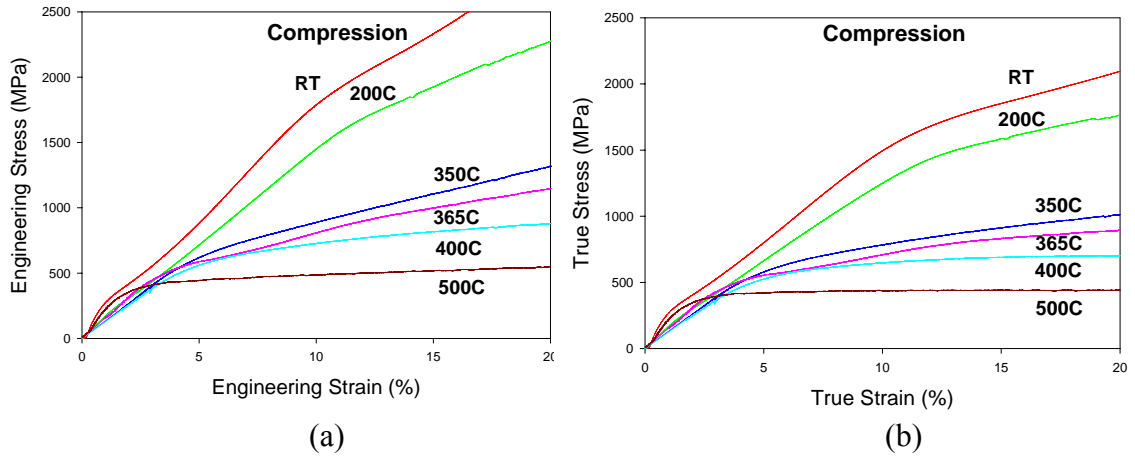


Figure 4-16 NiTiPd Alloy Uniaxial Isothermal Compression Tests at RT, 200°C, 350°C, 365°C, 400°C and 500°C (a) Engineering Stress Strain Curve (b) True Stress Strain Curve

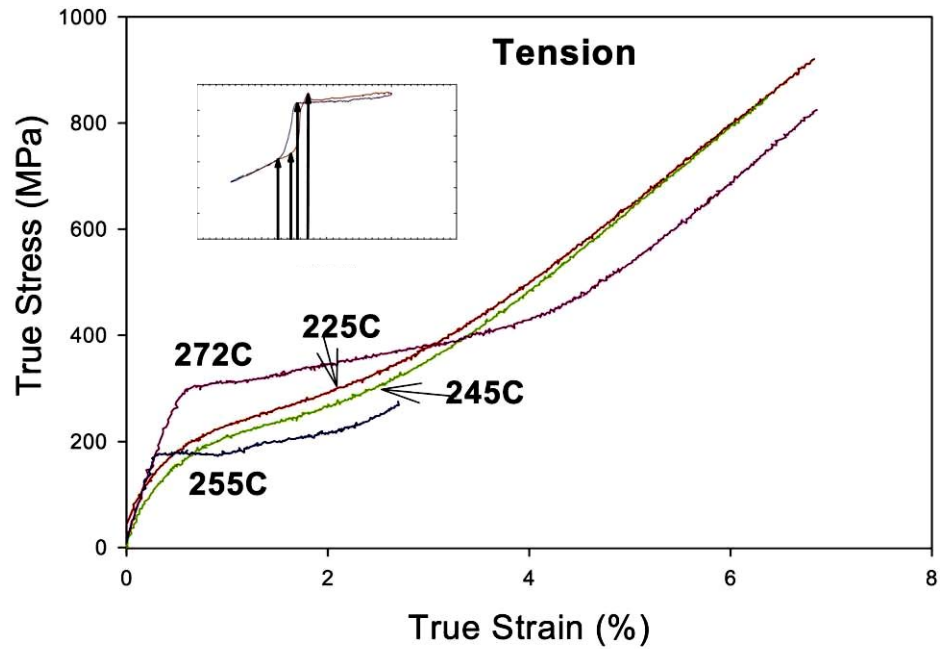


Figure 4-17 NiTiPd Alloy Uniaxial Isothermal Tensile Tests at 225°C, 245°C, 255°C and 272°C

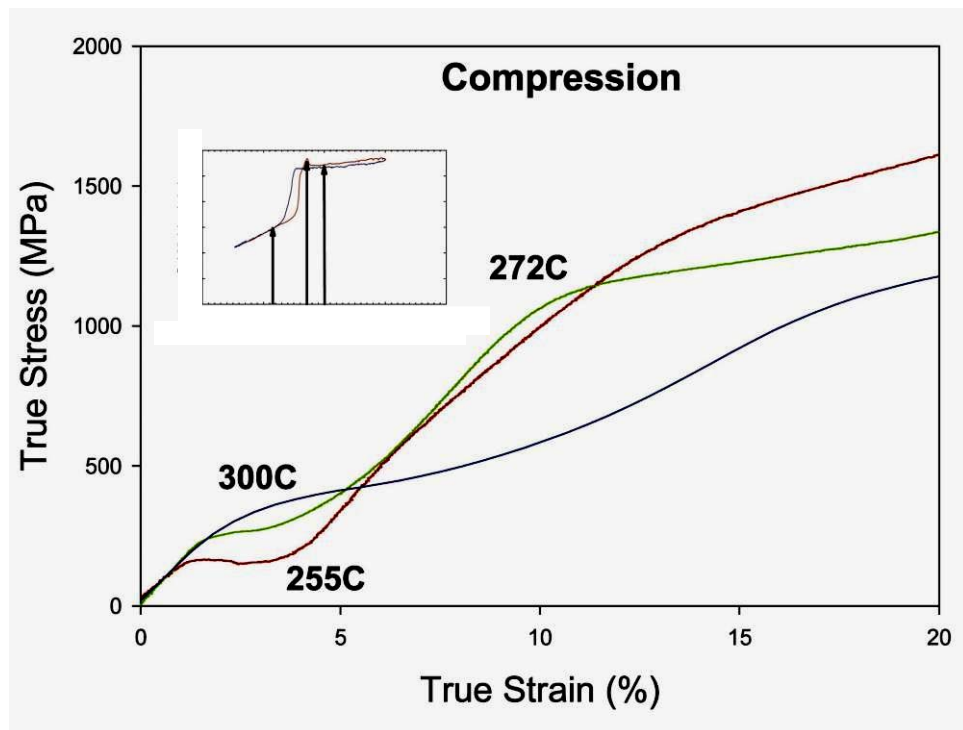


Figure 4-18 NiTiPd Alloy Uniaxial Isothermal Compression Tests at 255°C, 272°C and 300°C

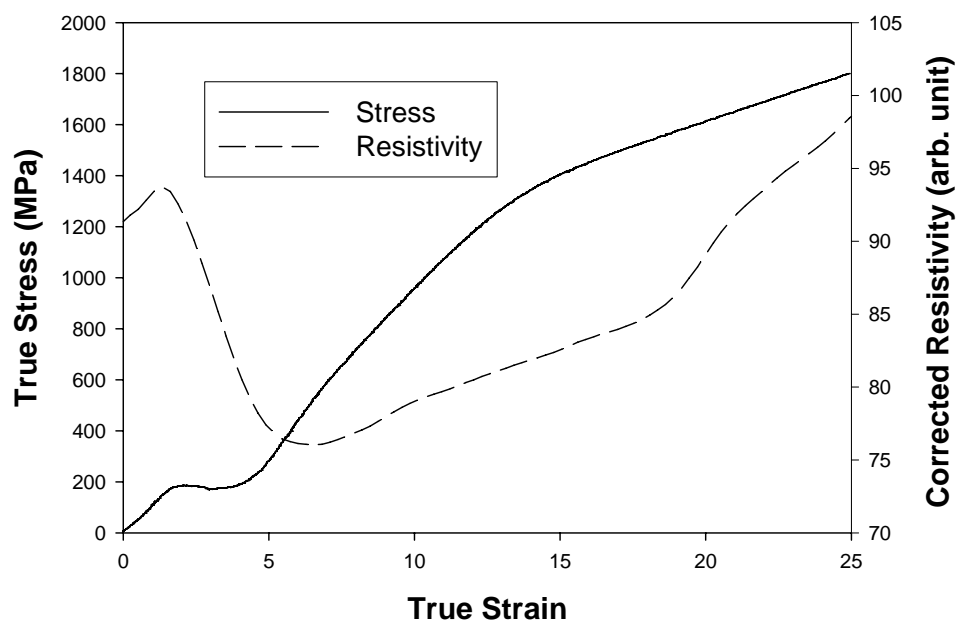


Figure 4-19 Isothermal Uniaxial Stress Strain Curve with Resistivity Exhibiting a Stress Induced Transformations

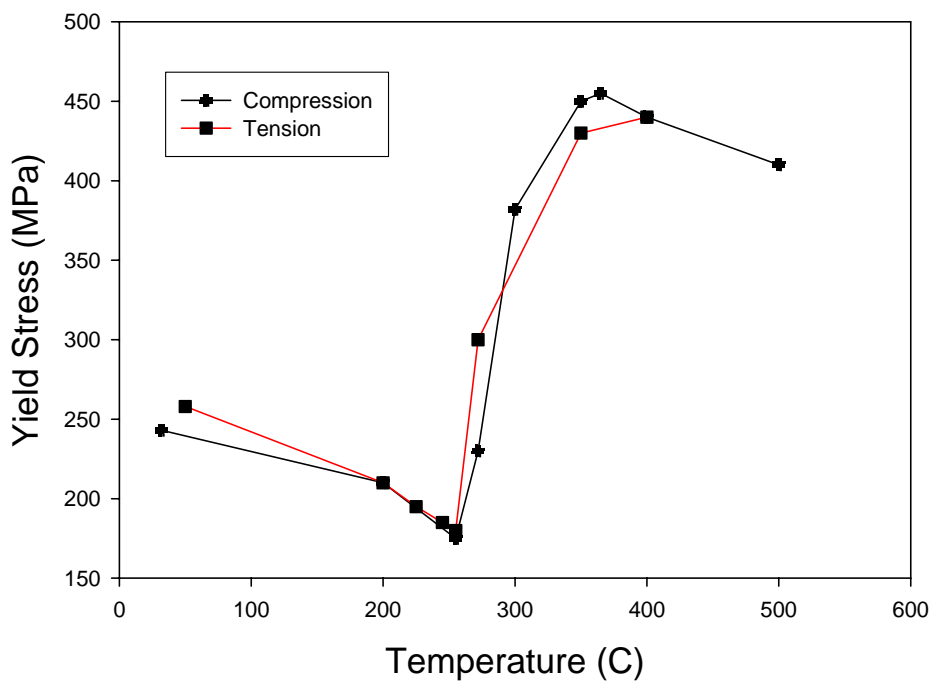


Figure 4-20 NiTiPd Yield Stress vs. Temperature in tension and compression

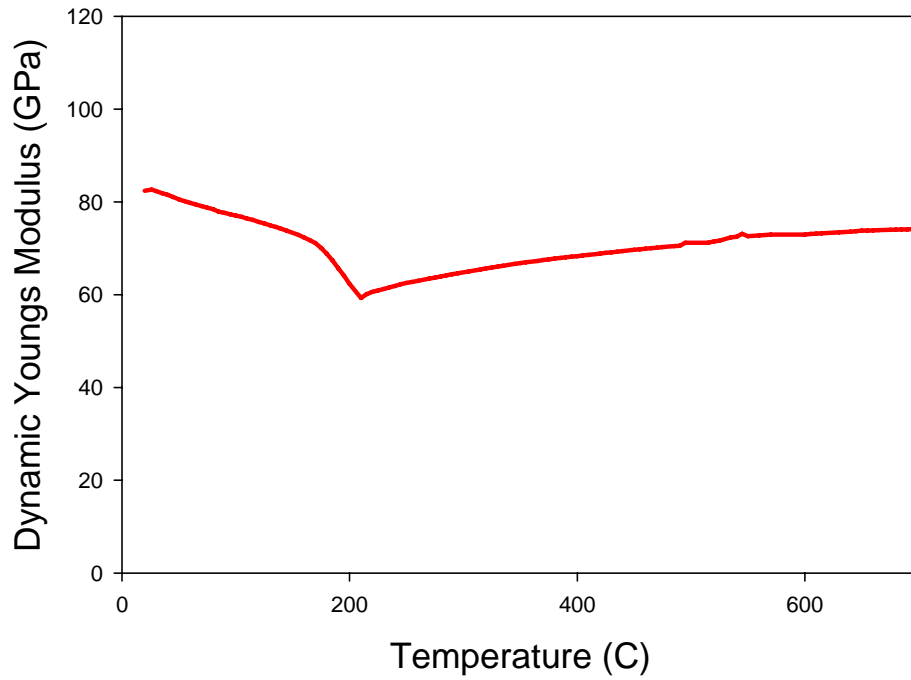


Figure 4-21 Temperature Dependent Dynamic Elastic Modulus measured on heating

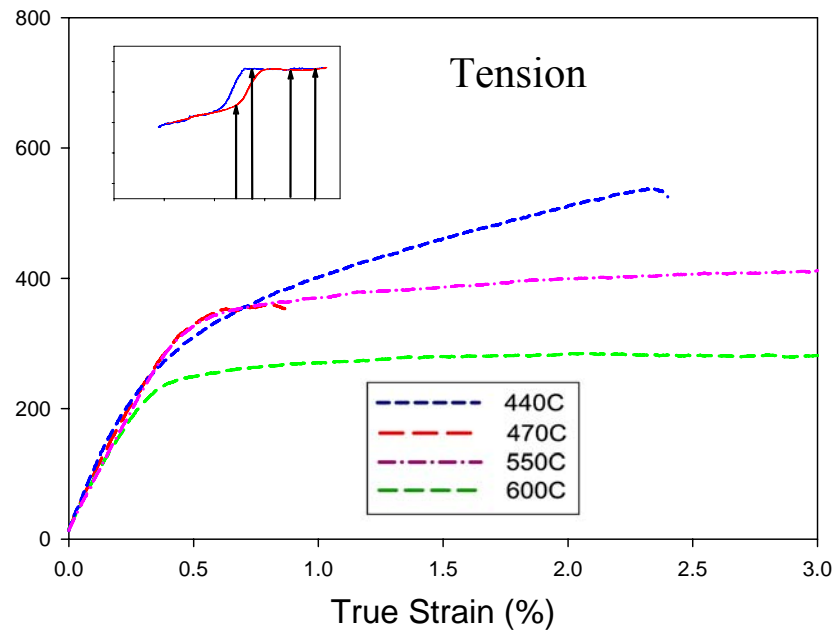


Figure 4-22 NiTiPt Alloy Uniaxial Isothermal Tensile Tests at 440°C, 470°C, 550°C and 600°C

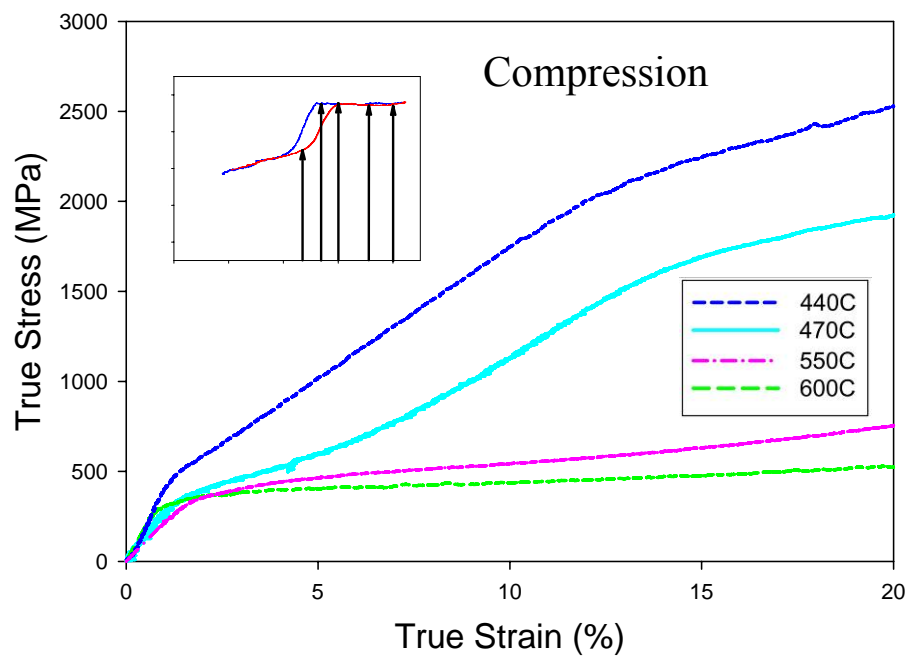


Figure 4-23 NiTiPt Alloy Uniaxial Isothermal Compression Tests at 440°C, 470°C, 490°C, 550°C, and 600°C

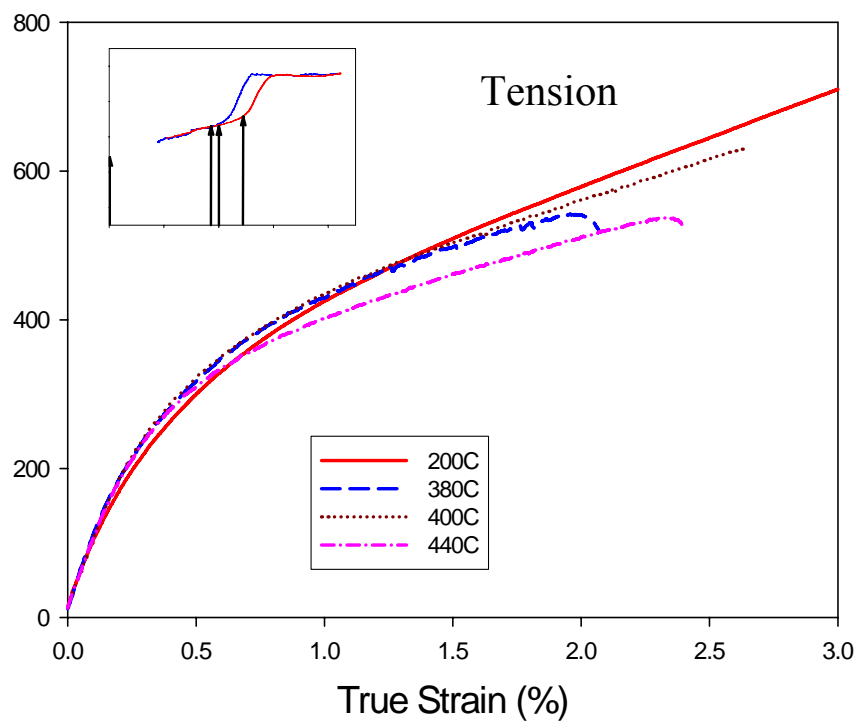


Figure 4-24 NiTiPt Alloy Uniaxial Isothermal Tensile Tests at 200°C, 380°C, 400°C and 440°C

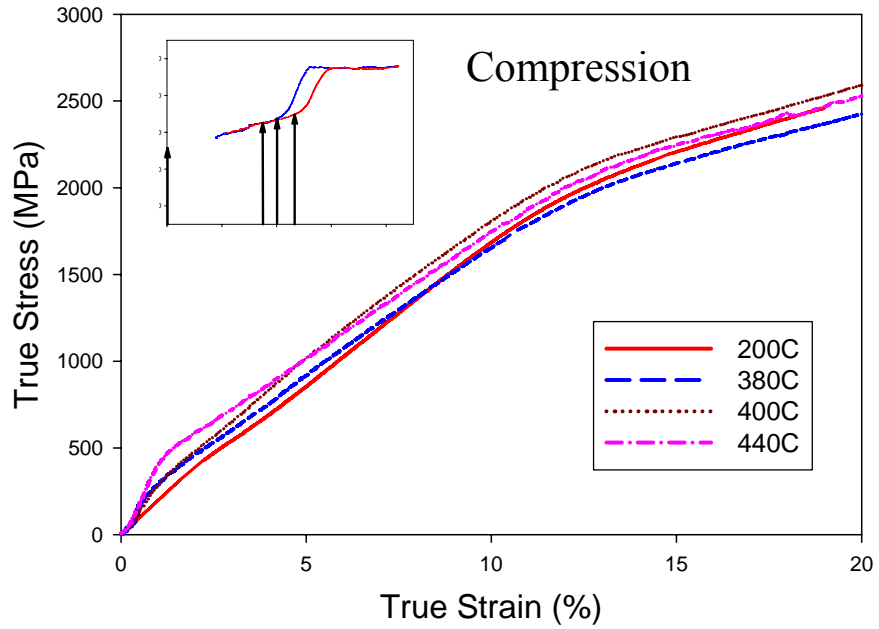


Figure 4-25 NiTiPt Alloy Uniaxial Isothermal Compression Tests at 200°C, 380°C, 400°C and 440°C

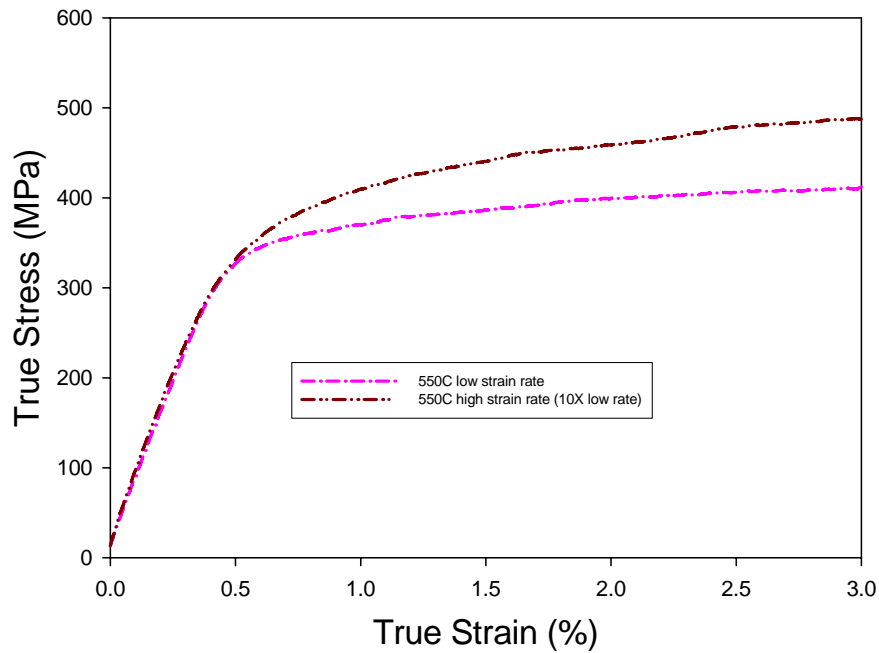


Figure 4-26 Stress Strain Curve at 500 Celsius at Low and High Strain Rates

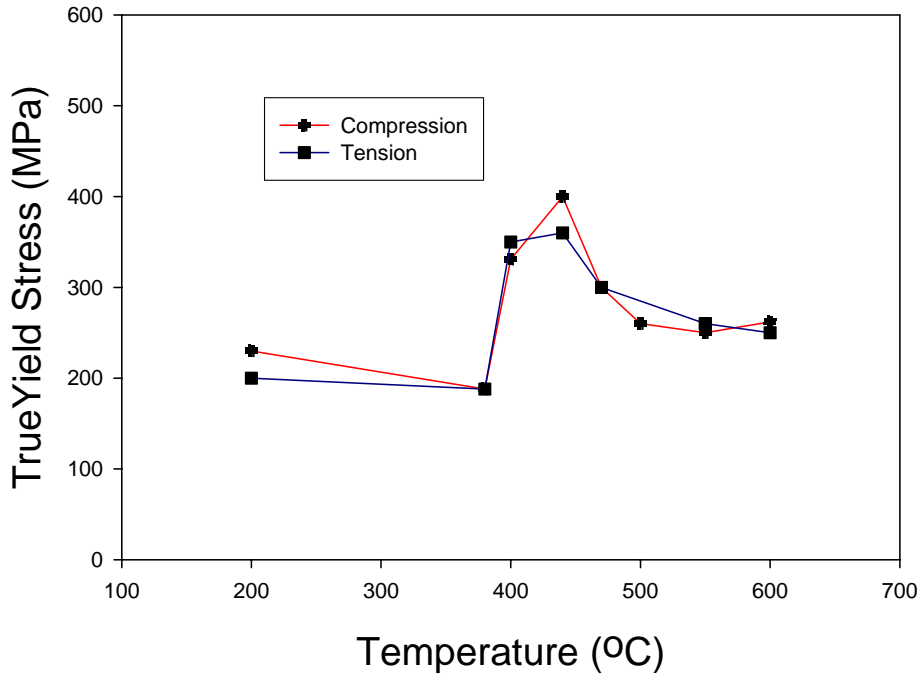


Figure 4-27 Yield Stress vs. temperature for NiTiPt

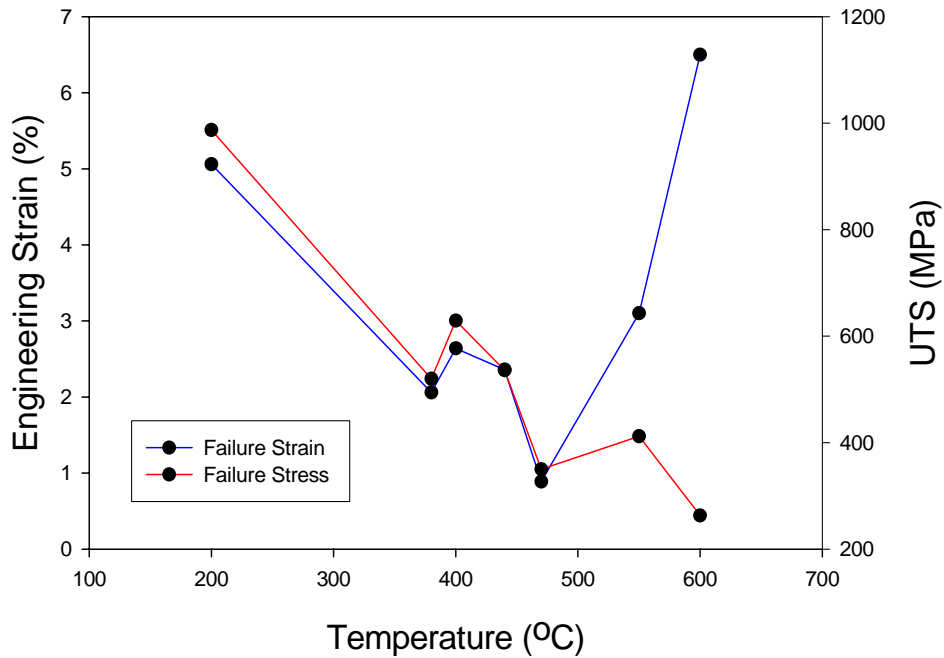


Figure 4-28 Fracture Stress and Strain vs. temperature for NiTiPt

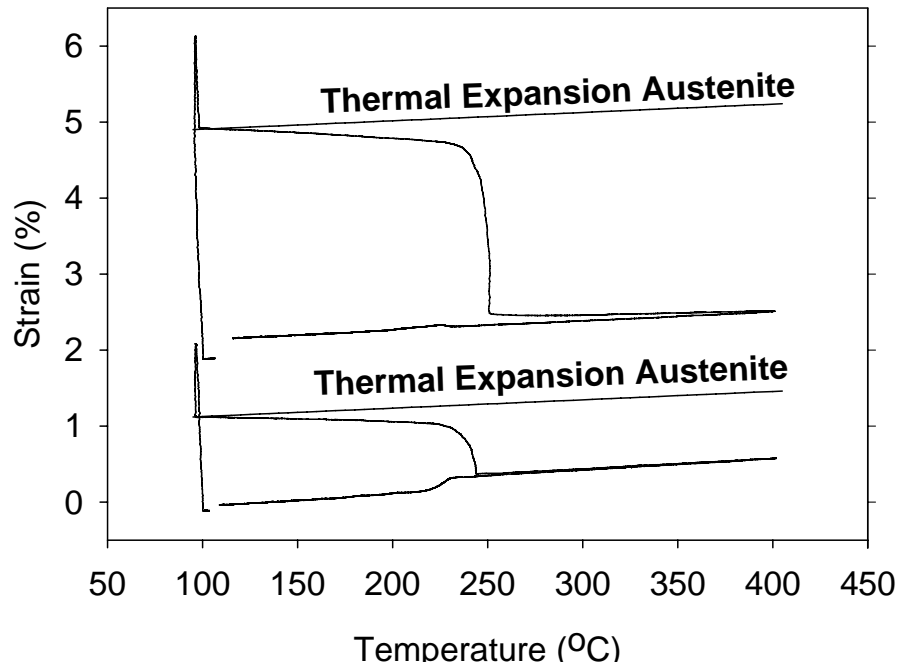


Figure 4-29 NiTiPd Unconstrained Recovery Test at 4 and 2 Percent Initial Strains.

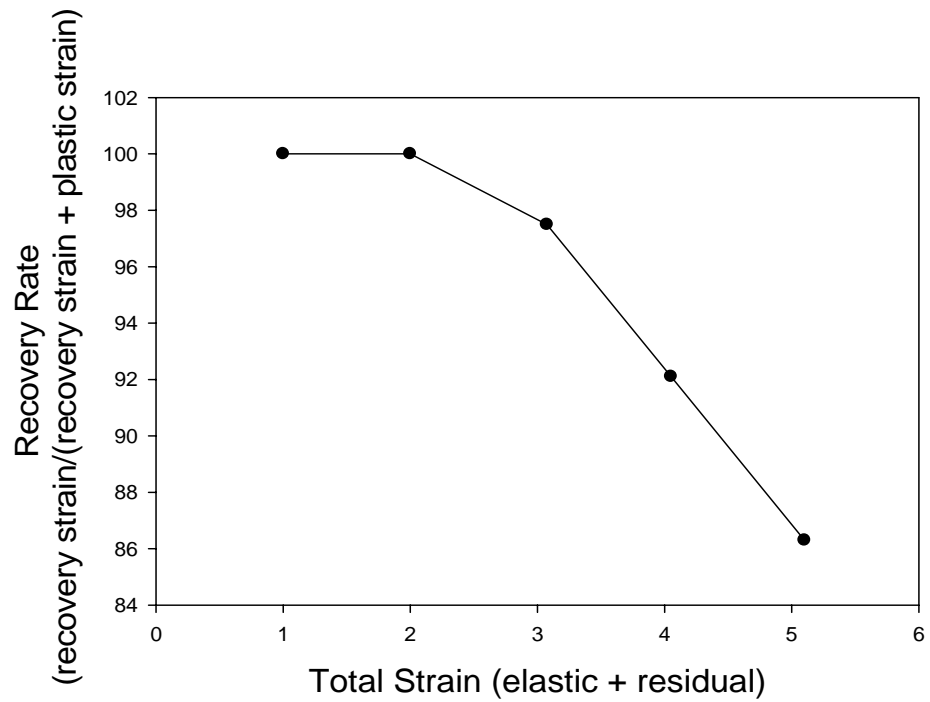


Figure 4-30 Total Recovery Rate vs. Total Strain for NiTiPd

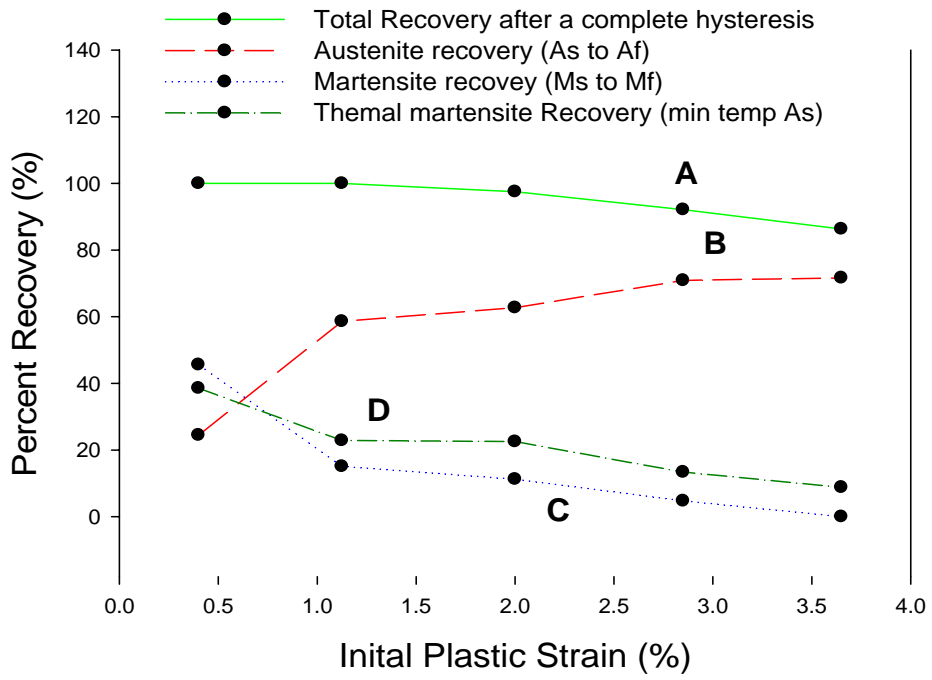


Figure 4-31 Load Free Recovery Individual Components of Total Recovery for NiTiPd

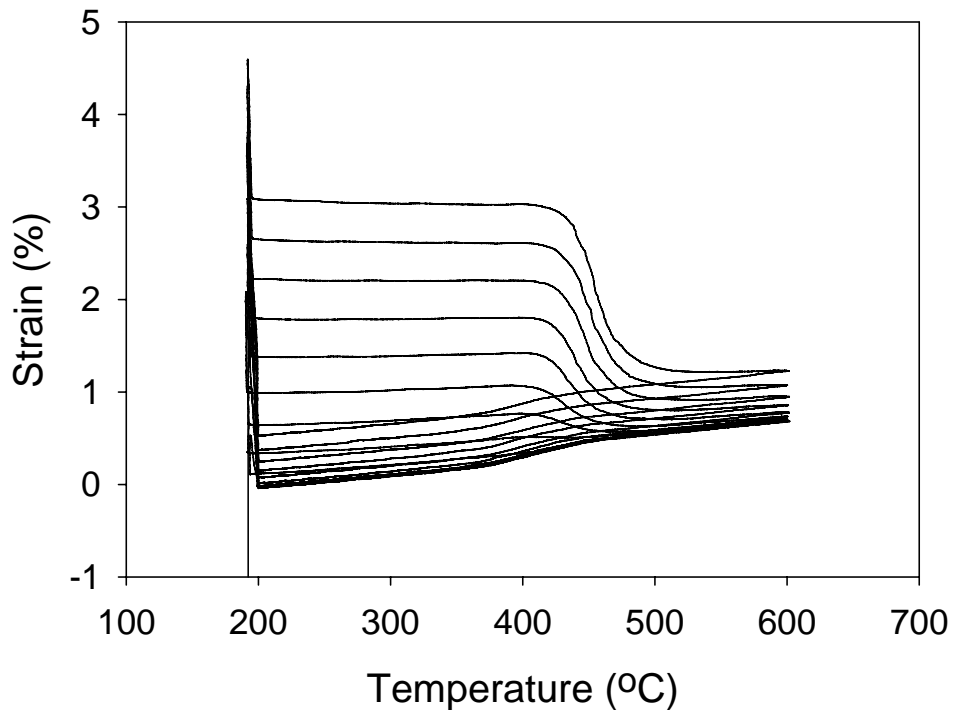


Figure 4-32 Temperature Dependent Load Free Recovery Curve for Complete NiTiPd Test

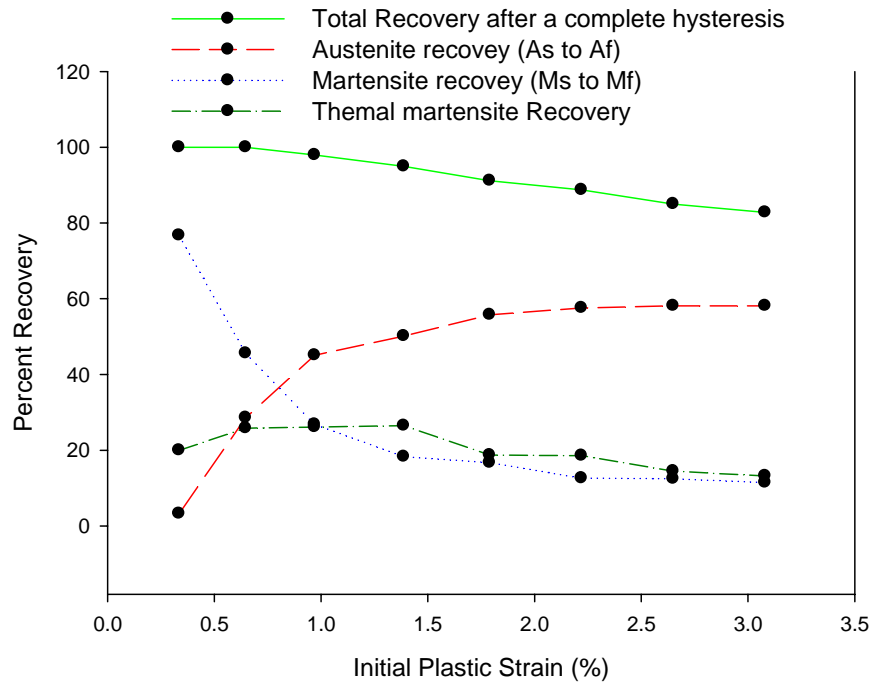


Figure 4-33 Load Free Recovery Individual Components of Total Recovery for NiTiPt

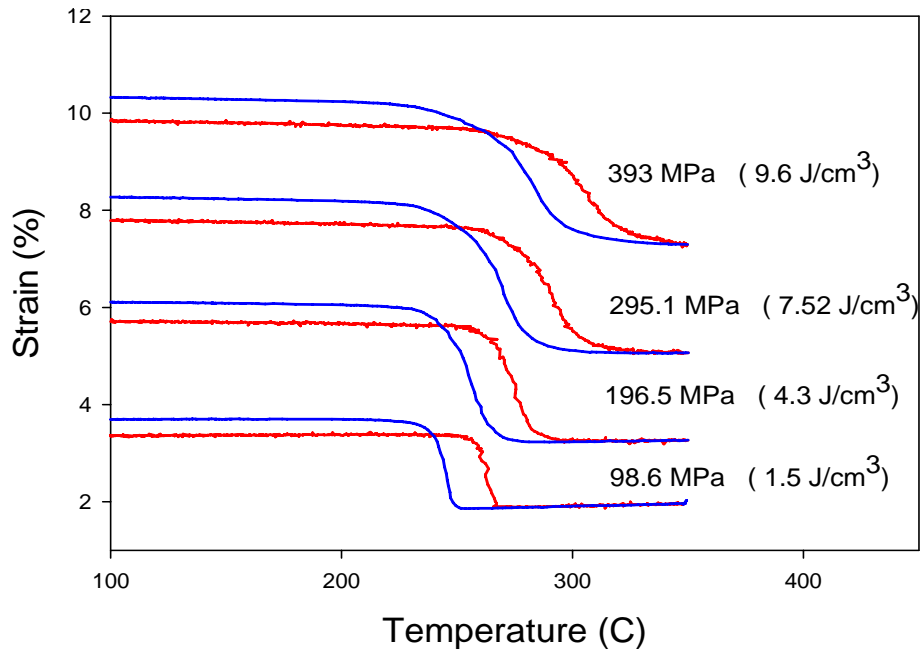


Figure 4-34 Load Bias in Tension (Specific Work Output) for NiTiPd

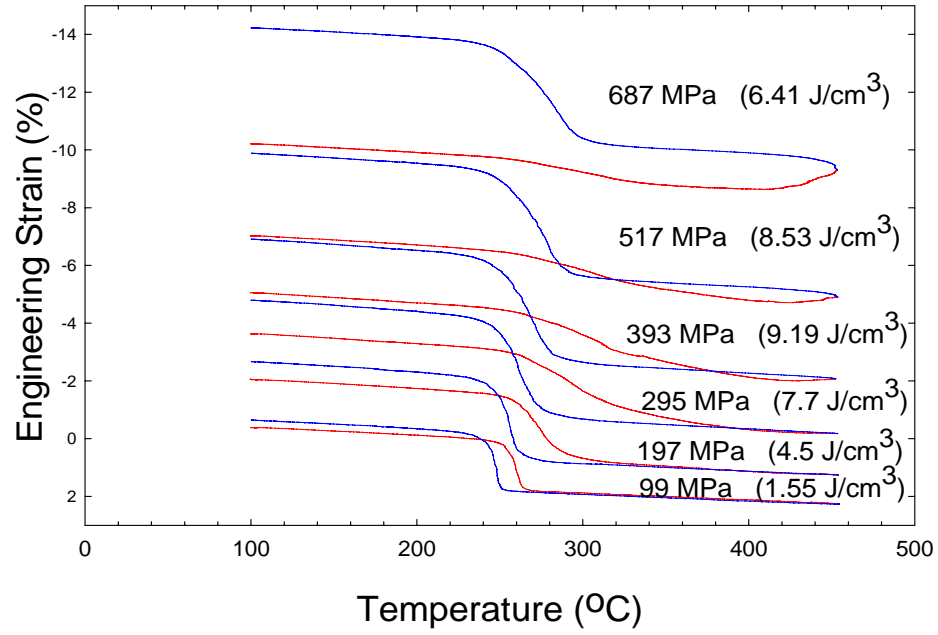


Figure 4-35 Load Bias in Compression (Specific Work Output) for NiTiPd

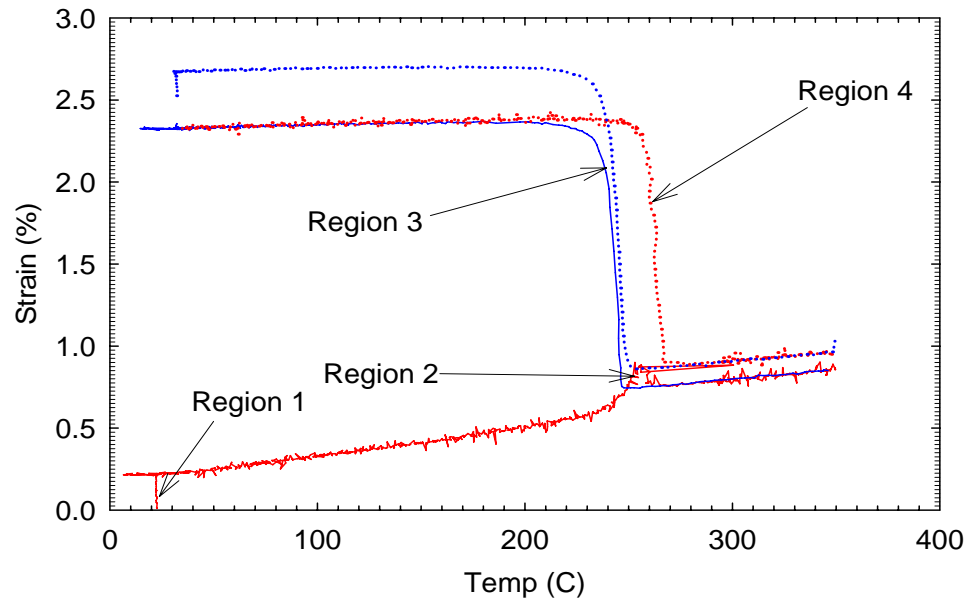


Figure 4-36 Load Bias in Tension (Specific Work Output) Complete Thermomechanical Path for NiTiPd

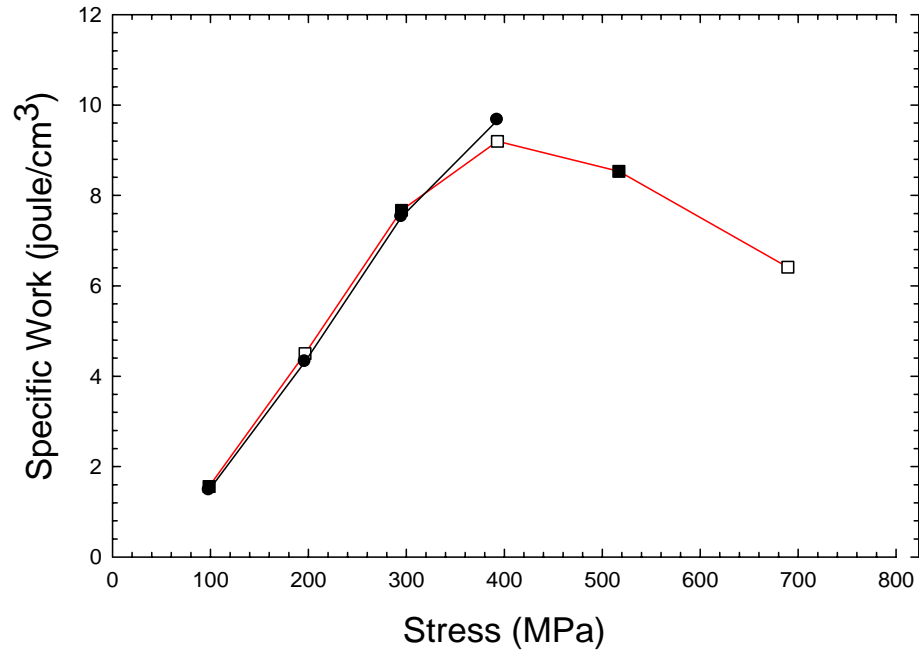


Figure 4-37 Specific Work vs. Biasing Load for NiTiPd

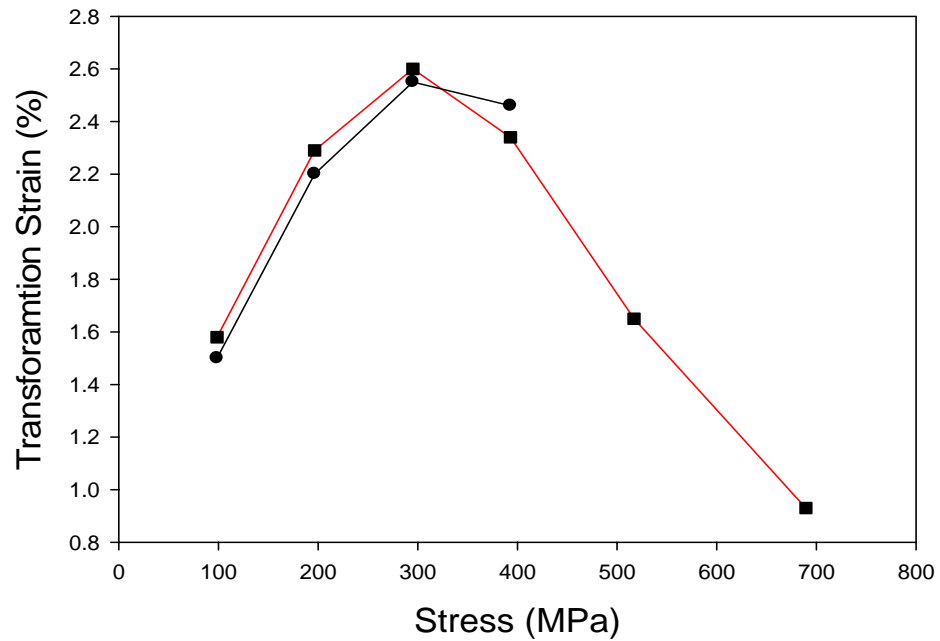


Figure 4-38 Transformation Strain (2nd cycle martensite to austenite) vs. Biasing Load for NiTiPd

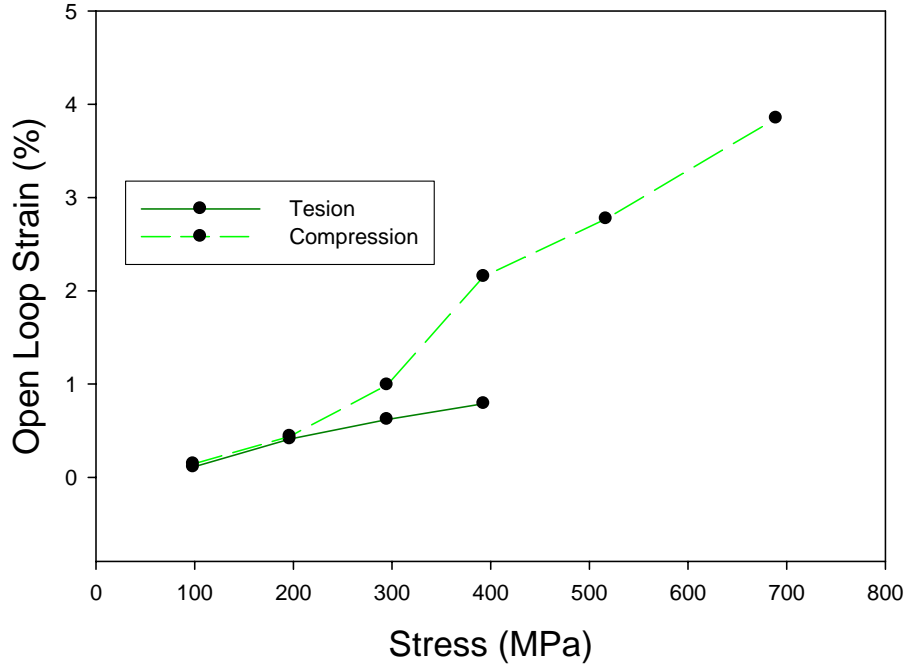


Figure 4-39 Open Loop Strain vs. Biasing Stress for NiTiPd

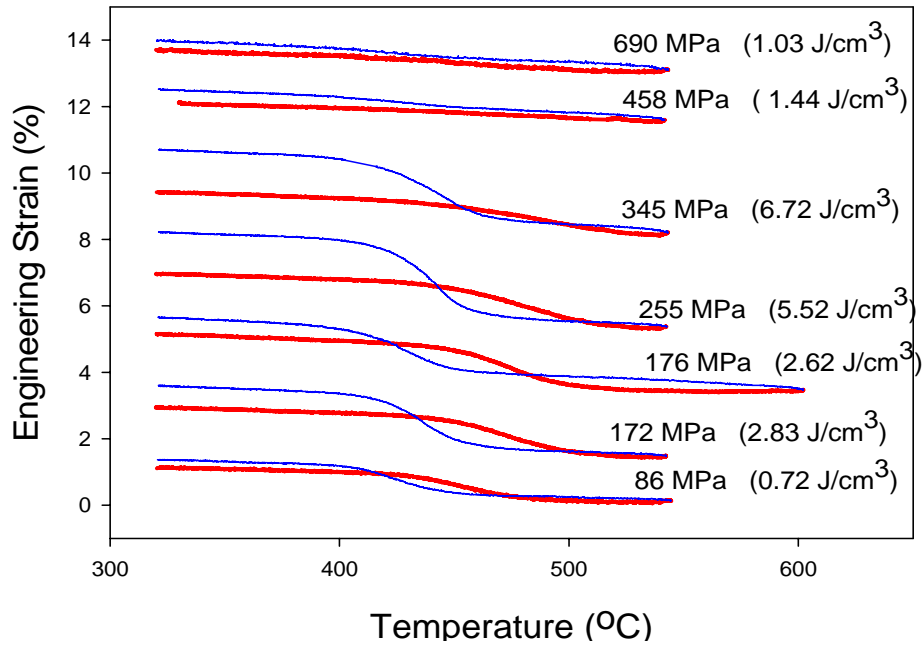


Figure 4-40 Load Bias in Compression (Specific Work Output) for NiTiPd

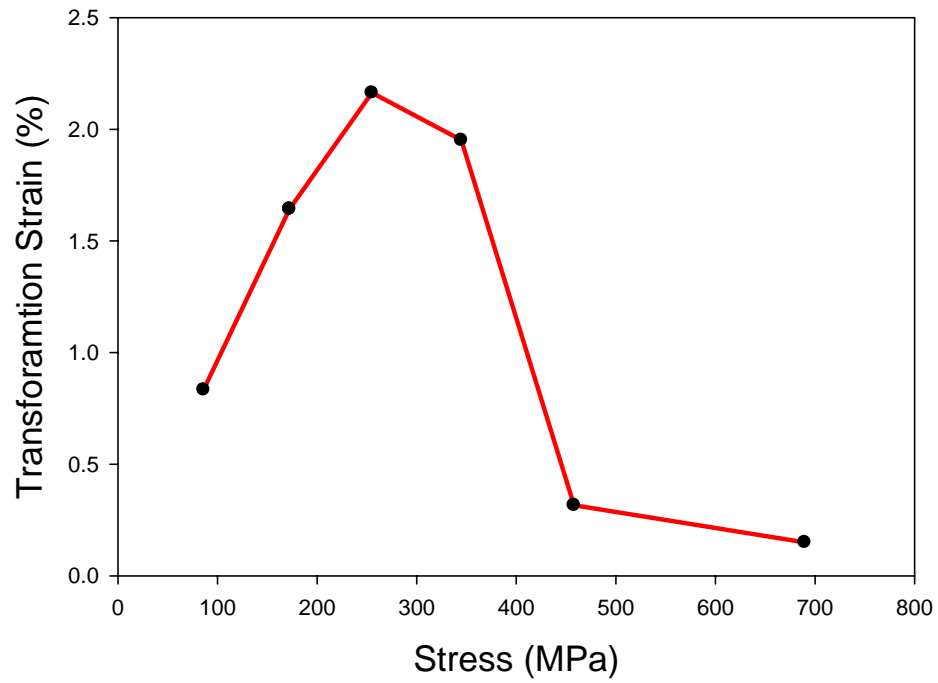


Figure 4-41 Transformation Strain (2nd cycle martensite to austenite) vs. Biasing Load for NiTiPt

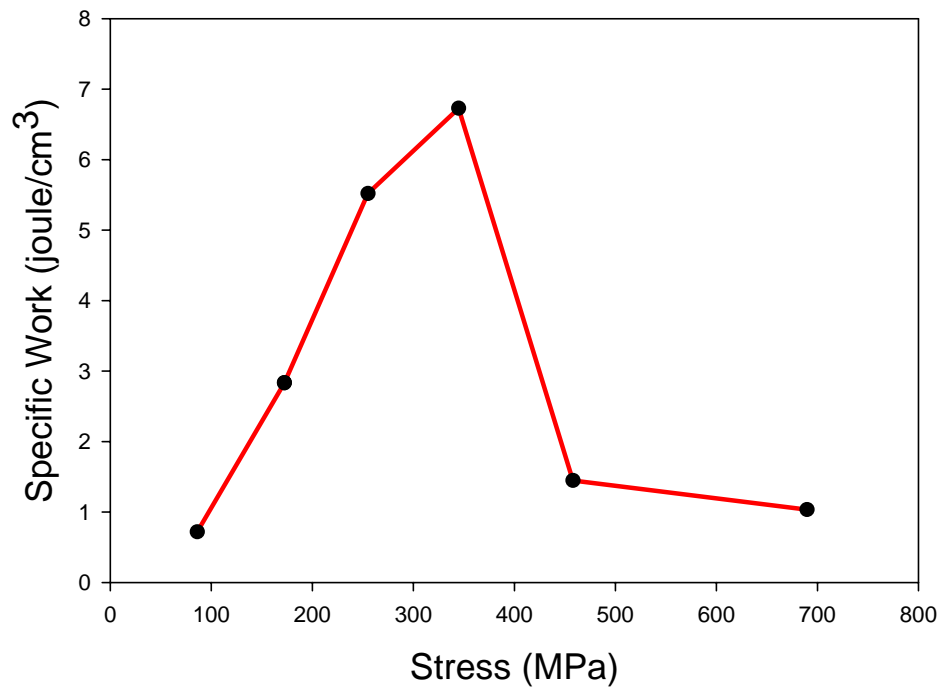


Figure 4-42 Specific Work vs. Biasing Load for NiTiPt

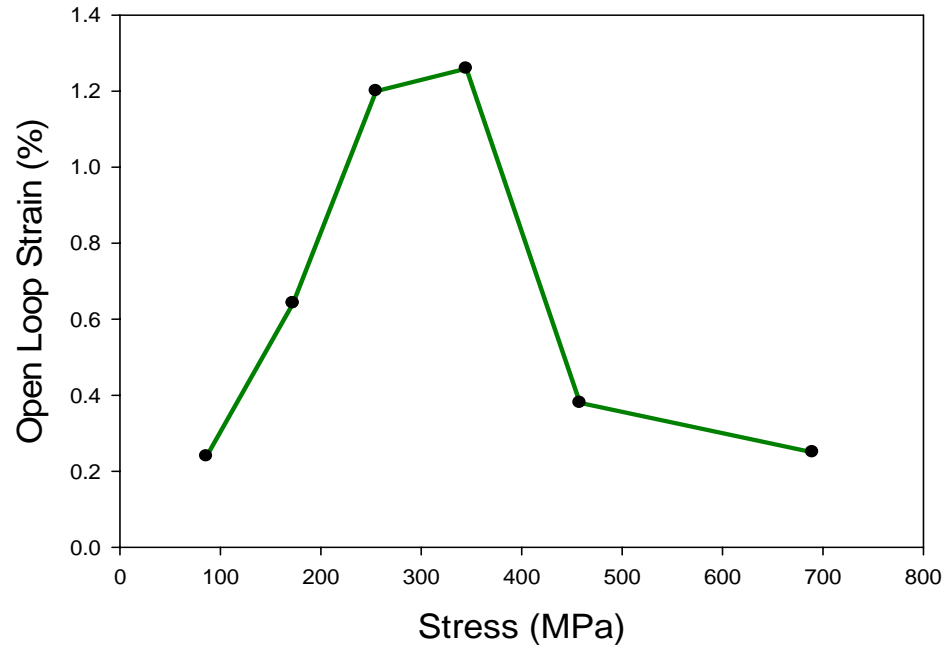


Figure 4-43 Open Loop Strain vs. Biasing Stress for NiTiPt

CHAPTER 5 SUMMARY AND CONCLUSIONS

Alloy Development

Of the several candidate alloy systems for high temperature shape memory actuation, the NiTiPt and NiTiPd systems were selected. Pt or Pd additions to binary NiTi above approximately 10%, satisfying the $\text{Ni}_{50-x}\text{Pt}_x\text{Ti}_{50}$ or $\text{Ni}_{50-x}\text{Pd}_x\text{Ti}_{50}$ compositional relationship, raise the thermoelastic transformation temperatures significantly. Although both alloying additions to NiTi resulted in elevated transformation temperatures and comparable ordered orthorhombic crystal structures, each system had quite different mechanical properties and shape memory attributes. Therefore, a multi system comparison was explored in an attempt to draw parallels to these differences in mechanical properties and the shape memory specific properties of each alloy.

Two alloys, one from each alloy system were selected for thermo-mechanical testing and comparison of shape memory specific properties. The $\text{Ni}_{30}\text{Ti}_{50}\text{Pt}_{20}$ alloy was selected based on the results from an initial screening study of over 20 NiTiPt alloys that focused on elevated transformation temperatures and the effects of deviations from stoichiometry (i.e., deviations from $(\text{Ni}+\text{Pt})/\text{Ti} = 1$). Analysis of this compositional study in combination with the results of a baseline thermo-mechanical studies on the $\text{Ni}_{30}\text{Pt}_{20}\text{Ti}_{50}$ and $\text{Ni}_{20}\text{Pt}_{30}\text{Ti}_{50}$ facilitated the selection of a Pt modified NiTi shape memory alloy based on transformation temperatures, microstructure and specific work output. The NiTiPd alloy was selected based on prior studies which focused on the effect of stoichiometric Pd for Ni alloying additions on transformation temperatures and no-load

recovery tests. Particularly the baseline composition of 30Pd showed a maximum in the no-load recovery therefore it seemed probable that this alloy was a good candidate for high temperature shape memory actuation.

The final selection of the $\text{Ni}_{30}\text{Pt}_{25}\text{Ti}_{50}$ and $\text{Ni}_{30}\text{Pd}_{30}\text{Ti}_{50}$ was made slightly Ti rich by .5% in order to insure elevated transformation temperatures. This yields a small volume fraction Ti rich phase since both the iso-stoichiometric lines between NiTi-PtTi and NiTi and PdTi are strong line compounds with little solubility for excess Ti. This Ti rich phase has a high affinity for interstitial elements and therefore reacts with any available carbon impurities acquired from the graphite crucible to form carbides. The excess Ti has a high affinity for carbon and oxygen thus assures that very little carbon or oxygen goes into solid solution but rather forms a small volume fraction of oxide and or carbide phases.

Characterization and Thermomechanical Testing

The transformation temperatures were determined by electrical resistivity techniques and dilatometric techniques. The change in resistivity and transformation strain were measured along side the temperature coefficient of resistivity and thermal expansion. These are important parameters in the design of shape memory alloy devices. A unique instrument was developed which simultaneously measure mechanical and electrical properties. This instrument was employed in order to accurately determine what the initial structure is and where the test temperature lies relative to the transformation temperatures. Additionally the structure during deformation and loading schemes is determined by analysis of the sample's electrical resistivity.

Isothermal mechanical test were conducted above below and at the transformation temperatures which developed the baseline mechanical properties of the austenitic and

martensitic phases. Analysis of the temperature dependent yield stress showed that the difference in yield strength between the high and low temperature phases was significantly different in the NiTiPt and NiTiPd alloys. The NiTiPt alloy exhibited a smaller change in yield strength between the martensite and the austenite. Recalling that the yield strength in the martensite is indicative of the stress required for detwinning while the yield strength in the austenite is related to slip processes therefore for a shape memory alloy to be a good candidate for actuation applications the martensite must be weaker than the austenite. Additionally the martensite in the NiTiPt alloy fractured in a brittle manner at low strains. It was possible to stress induce martensite in the NiTiPd alloy while no detectable stress induced transformations occurred in the NiTiPt alloy. Dynamic modulus measurements provided confirmation of pre-martensitic elastic softening in the NiTiPd alloy which is an important characteristic of thermoelastic transformations.

Analysis of the fracture stress and strain at various temperatures revealed a change in fracture mechanisms (ductile to brittle behavior) near the transformation temperatures of the NiTiPt alloy. Particularly the stress and strain both decreased with increasing temperature up to the transformation temperatures after which the fracture stress decreased with increasing temperature as the fracture strain increased. Isothermal uniaxial tests at different strain rates verified that dynamic recovery is a prevalent mechanism in the austenite phase. This is a feasible mechanism which explains the increase in transformation strain and associated decrease in transformation stress as temperature increases.

Load free recovery tests were performed on each alloy incrementing the initial strain levels until fracture. The strain was monitored continuously during the deformation and recovery process. Thermal cycling through the hysteresis revealed several stages of recovery processes which contribute to the total recovery. The three main contributions consisted of thermal recovery, martensite to austenite recovery and austenite to martensite recovery. The analysis of these measurements revealed the fraction of strain which is accommodated by reversible (detwinning) and non-reversible processes (slip) as well as the strain associated with the formation of correspondent variant pairs. Combined with the isothermal martensitic stress-strain curves it was possible to correlate regions of the stress strain curves with the underlying deformation mechanisms. Particularly the pseudo stress strain curve, for low strain values, was determined to be deforming completely by detwinning yet the rearrangement of twins did not occur at a constant stress.

Load bias test were conducted in tension and compression for the NiTiPd alloy. These test measure a shape memory alloys ability to do work (specific work output). Thermal cycling through the hysteresis was performed under a constant load. The transformation strains associated with the forward (austenite to martensite) and reverse (austenite to martensite) reactions were measured. The specific work was calculated from the product of the engineering stress and the transformation strain or recovery strain during the heating cycle upon which the sample does work against the biasing load. The results were similar in tension and compression. A maximum in the work output vs. biasing stress relationship was seen in both tension and compression. This maximum was linked to a maximum in the recovery strain which results from two components, mainly

non-recoverable slip and the formation of an oriented correspondent variant pair structure.

Conclusions Relevant to Alloy Design

This study is a section of a larger study geared toward the development of high temperature shape memory actuation materials. The further development of high temperature shape memory alloys to the point where they are feasible for commercial applications is limited by the limited knowledge database on advanced alloy development, thermomechanical processing and mechanical test procedures and results. Several goals were sought in this portion of the study. Unique instrumentation and testing methods were explored and developed to examine the baseline mechanical properties in combination with shape memory alloy specific properties. Additionally, this study was to identify areas in high temperature shape memory alloys where targeted alloy development and thermomechanical processing could improve the shape memory characteristics of the alloy, specifically the work output. In order to accomplish this two comparable alloys were developed from a relatively well known system (NiTiPd) and a system which, although superior in high temperature transformation temperatures, has received little advanced thermomechanical studies. These systems parallel each other structurally, yet have very different shape memory performances. Therefore a comparison of these alloys could give some insight as to where future work should focus.

Throughout this study it seemed that two main properties were inhibiting the performance of these alloys. Primarily the alloys resistance to slip under a biasing load in the temperature regions near the transformation temperatures prevented complete recovery and thus a maximum in the recovery strain. Additionally a link between the difference in yield strength between the austenite and martensite and the performance

under a biasing load was confirmed. During the transformation the stress state in the interface is high, therefore, in order to prevent slip in a region of the material which is already highly stressed a permanent strengthening mechanism which is stationary as the interface passes must be present. Second phase strengthening and dispersion hardening are both methods which may accomplish this. Additionally a sessile dislocation network which is formed by the movement of the interface itself could prove useful in forming entanglements for mobile dislocations. Although a direct link to the prior statement has not been made, repeated movements of the interface under load (training) has been shown to decrease the amount of slip under a biasing load. This would be feasible for the NiTiPd alloy and not the NiTiPt alloy as dynamic recovery sets in heavily just above the transformation temperatures.

Future Studies

Although mechanisms explaining the deformation behavior were proposed here, significant gaps remain in their experimental confirmation. In order to address these a series of experiments could be conducted which analyze the extruded and deformed structures. This investigation consists of three main parts. Primarily a set of martensitic samples will be strained in into the different regions of the stress strain curves then unloaded. The as extruded and deformed structures will then be analyzed by TEM and the results compared. This could be used to determine prevalent detwinning reactions by the comparison of the starting and deformed structures. A similar study has been performed on NiTi thin films⁶².

A second part of the investigation will analyze the structure of the stress induced martensite which consists of highly oriented correspondent variant pairs, in comparison to the thermal martensite which should be more randomly oriented. Although not

included in this work preliminary investigations showed that at particular test temperatures the stress induced martensite remains in the material even after the applied stress is removed. Upon unloading a two phases exist in the alloy. These are the stress induced martensite and the austenite. Now if the sample is allowed to cool the remaining austenite transforms thermally to martensite. It has been verified in preliminary test that these structures are indeed different by DTA analysis which showed two peaks in a sample which contains stress induced martensite while a sample which does not exhibits one peak. The orientation relationship between the stress induced martensite and the martensite which transforms under no-load could be exploited to compare the formation a random distribution and an oriented one.

A significant question in thermoelastic transformations and in the development of shape memory alloys ask how is the strain be accommodated. If it is largely plastic, then the deformation is not reversible in contrast to elastic accommodation and detwinning. The final phase of the proposed study applies the thermodynamics of thermoelastic transformations as a tool to measure the amount of residual elastic stress remnant after deformation. This portion of the study models the relationship between the transformation temperatures and applied stress. Prior work conducted here has developed a test method which measures the shift in transformation temperatures and has successfully conducted the necessary test to build a baseline relationship between the transformation temperatures and the materials stress state. Now by taking the alloys deformed for TEM analysis and recovering them in a DTA it is possible to determine what the internal stress state of the material is by correlating the shift in transformation temperature to the materials stress state.

APPENDIX A
NiTiPd HTSMA MATERIAL DATA SHEET

(This material is suitable for shape memory applications with transformation temperatures greater than 200 °C)

Physical Properties

Density 7.6 g/cm³

Electrical Resistivity

Martensite (@ A _s)	93 μohm-cm
Austenite (@ M _s)	114 μohm-cm

Thermal Coefficient of Resistivity

Martensite	12 x 10 ⁻² μohm-cm /°C
Austenite	18 x 10 ⁻³ μohm-cm /°C

Coefficient of Thermal Expansion

Martensite	16 x 10 ⁻⁶ /°C
Austenite	11 x 10 ⁻⁶ /°C

Shape Memory Properties

Transformation Temperatures

Austenite Start Temperature (A _s)	255 °C
Austenite Finish Temperature (A _f)	260 °C
Martensite Start Temperature (M _s)	249 °C
Martensite Finish Temperature (M _f)	239 °C

Composition

Nickel (nominal)	19.5 at.%
Palladium (nominal)	30.0 at.%
Titanium (balance)	balance
Oxygen (maximum)	0.30 at.%
Carbon (nominal)	0.50 at.%

APPENDIX B
NiTiPt HTSMA MATERIAL DATA SHEET

(This material is suitable for shape memory applications with transformation temperatures greater than 400 °C)

Physical Properties

Density 9.9 g/cm³

Electrical Resistivity

Martensite (@ A _s)	110 μohm-cm
Austenite (@ M _s)	135 μohm-cm

Thermal Coefficient of Resistivity

Martensite	85 x 10 ⁻³ μohm-cm /°C
Austenite	91 x 10 ⁻⁴ μohm-cm /°C

Coefficient of Thermal Expansion

Martensite	99 x 10 ⁻⁷ /°C
Austenite	96 x 10 ⁻⁷ /°C

Shape Memory Properties

Transformation Temperatures

Austenite Start Temperature (A _s)	446 °C
Austenite Finish Temperature (A _f)	491 °C
Martensite Start Temperature (M _s)	458 °C
Martensite Finish Temperature (M _f)	417 °C

Composition

Nickel (nominal)	19.5 at.%
Platinum (nominal)	25.0 at.%
Titanium (balance)	balance
Oxygen (maximum)	0.30 at.%
Carbon (nominal)	0.50 at.%

APPENDIX C
CHEMICAL ANALYSIS OF EXTRUDED MATERIALS

Ext. ID	Ti	Ni	Pt	Pd	C	N	O
20	50.4	19.3		29.4	0.446	0.014	0.334
21	50.5	19.4		29.3	0.437	0.014	0.305
22	50.4	19.4		29.5	0.436	0.014	0.268
23	50.6	19.6		29.0	0.400	0.014	0.270
24	50.6	19.3		29.4	0.421	0.014	0.263
25	50.6	19.2		29.4	0.482	0.014	0.266
30	50.4	24.4	24.4		0.431	0.018	0.277
31	50.3	24.4	24.3		0.645	0.018	0.306
32	50.3	24.4	24.5		0.504	0.012	0.283
33	50.4	24.4	24.4		0.449	0.018	0.269
34	50.4	24.4	24.4		0.503	0.015	0.280
35	50.3	24.4	24.5		0.468	0.012	0.299

LIST OF REFERENCES

1. C. M. Wayman MRS Bulletin April (1993) 49.
2. R.D. Noebe, T. Biles, and S.A Padula, in Advanced Structural Materials: Properties, Design Optimization, and Applications, W.O. Soboyejo, ed., Taylor & Francis Group, Boca Raton, FL. 2005. p. 141.
3. C.M. Wayman and T.W. Duerig, in Engineering Aspects of Shape Memory Alloys, ed., Butterworth-Heinemann, Boston, 1990. p. 3.
4. J. V. Humbeeck, *Maters. Sci. Eng. A* 273 (1999) 134.
5. L. McD. Schetky, *Maters. Sci. Forum* 327 (2000) 9.
6. C. Mavroidis, *Res. Nondestr. Eval.*, 14 (2002) 1.
7. C.M. Hwang and C.M. Wayman, *Scripta Metall.* 17 (1983) 38.
8. S. Miyazaki and K. Otsuka, *Metall. Trans.* 17A (1986) 53.
9. K. Otsuka and X. Ren, *Intermetallics* 7 (1999) 511.
10. K. Hane and T. Shield, *Acta Materialia* 47 (1999) 2603.
11. P.G. Lindquist, Ph.D. Dissertation, University of Illinois (1988).
12. T. Hara, T. Ohba, and K. Otsuka, *Mater. Trans. JIM* 38 (1997) 11.
13. L.L. Meisner, V.P. Sivokha *Physica B* 344 (2004) 93.
14. R. Reed-Hill, R. Abbaschian, in *Physical Metallurgy Principles*, ed. PWS Publishing, 1992. p. 267.
15. R. J. COMSTOCK, *Acta Met.* 44 (1996) 3505.
16. D. S. Lieberman, M. S. Wechsler, and T. A. Read, *J. Appl. Phyx.* 26 (1955) 473.
17. M. S. Wechsler, D. S. Lieberman, and T. A. Read, *Trans. AIME* 197 (1953) 1503.
18. J. S. Bowles and J. K. Mackenzie, *Acta Metall.* 2 (1954) 129.

19. C.M. Wayman, in *Introduction to the Crystallography of Martensitic Transformations*, ed. Macmillan, NY 1964. p. 84.
20. K. Hane and T. Shield *Philosophical Magazine A*. 78 (1998) 1215.
21. K. Bhattacharya, in *Microstructure of Martensite*, ed. Oxford University Press 2003. p.144.
22. D. A. Porter and K. E. Easterling, in *Phase Transformations in Metals and Alloys*, ed. Chapman & Hall, London, 1991. p. 122.
23. H. C. Ling and W. S. Owen, *Acta Metall.* 29 (1981) 1721.
24. J. Uchil, K. Ganesh Kumara, and K. K. Mahesh, *Mater. Sci. Eng. A*, 332 (2002) 25.
25. http://www.sma-inc.com/html/_shape_memory_alloys_.html, Jan 2005.
26. L. Zhao, Ph.D. Thesis, University of Twente, Enschede, The Netherlands (1997).
27. R. Reed-Hill, R. Abbaschian, in *Physical Metallurgy Principles*, Ed. PWS Publishing, 1992. p. 580.
28. D. P. Dunne and C. M. Wayman, *Metall. Trans.* 4 (1973) 147.
29. J. Ortin and A. Planes, *Acta Met.* 36 (1988) 1873.
30. G. B. Olsen and M. Cohen, *Scripta Metall.* 9 (1975) 1247.
31. G. B. Olsen and M. Cohen, *Scripta Metall.* 11 (1977) 345.
32. http://home.paran.com/babocpu/_jwhbbs/12849882/1102477889_icpms.ppt Nov 2006.
33. G.W.H. Hohne, W.F. Hemminger, and H.J. Flammersheim, in *Differential Scanning Calorimetry*, ed. Springer, Berlin, 2003. p. 116.
34. J.G. Hust and A.B Lankford National Bureau of Standards Report of Investigation Research Materials 8420 and 8421.
35. R. Noebe, D. Gaydosh, S. Padula II, A. Garg, T. Biles, M. Nathal, *SPIE Conf. Proc.:Smart Structures and Materials 2005 San Diego, CA.*; 5761 (2005) 364.
36. P.G. Lindquist and C.M. Wayman, in *Engineering Aspects of Shape-Memory Alloys*, ed. T.W. Duerig, K.N. Melton, D. Stockel, and C.M. Wayman, ed. Butterworth-Heinemann, Boston 1990. p. 132.
37. H.C. Donkersloot and J.H. Van Vucht, *J. Less-Common Mets.* 20 (1970) 83.

38. T. Biggs, M.B. Cortie, M.J. Witcomb, and L.A. Cornish, *Metall. Mater. Trans. A* 32 (2001) 1881.
39. K. Otsuka and X. Ren, *Intermetallics* 7 (1999) 511.
40. T. Biggs, L.A. Cornish, M.J. Witcomb, and M.B. Cortie, *J. Alloys Compds.* 375 (2004) 120.
41. A. Garg, Unpublished Research, NASA Glenn Research Center, 2004.
42. O. Rios, R. Noebe, T. Biles, A. Garg, A. Palczer, D. Scheiman, H. J. Seifert, M.Kaufman, *SPIE Conf. Proc.: Smart Structures and Materials 2005*, San Diego, CA, 5761 (2005) 376.
43. W.B. Cross, A.H. Kariotis, and F.J. Stimler, *NASA CR-1433*, (1969).
44. N.G. Boriskina and E.M. Kenina, in *Titanium 80, Science & Technology, Proceedings of the 4th International Conference on Titanium 1980*. p. 2917.
45. N. Matveeva, Y. Kovneristy, A. Savinov, V. Sivokha, and V. Khachin, *J Phys* 4312 (1982) C4-249.
46. P.G. Lindquist and C.M. Wayman, in *Engineering Aspects of Shape-memory Alloys*, ed. T.W. Duerig, K.N. Melton, D. Stockel and C.M. Wayman, Butterworth-Heinemann, London, 1990. p.58.
47. V.N. Khachin, *Revue Phys. Appl.* 24 (1989) 733.
48. Q. Tian and J. Wu, *SPIE Conf. Proc.* 5116 (2003) 710.
49. S. Shimizu, Y. Xu, E. Okunishi, S. Tanaka, K. Otsuka and K. Mitose, *Maters. Lett.* 34 (1998) 23.
50. W.S. Yang and D.E. Mikkola, *Scripta Metall. Mater.* 28 (1993) 161.
51. K. Otsuka, K. Oda, Y. Ueno, M. Piao, T. Ueki, H. Horikawa, *Scripta Metall. Mater.* 29 (1993) 1355.
52. K. Otsuka and X. Ren, *Prog. Mater. Sci.* 50 (2005) 511.
53. M.V. Nevitt, *Trans. Metall. Soc. AIME* 218 (1960) 327.
54. R. Reed-Hill, R. Abbaschian, in *Physical Metallurgy Principles*, Ed. PWS Publishing, 1992 p. 230.
55. W. B. Cross, A. H. Kariotis, and F. J. Stimler *NASA CR-1433*, 1970.
56. M. J. ek, M. Slámová, and M. Hájek, *Journal of Alloys and Compounds*, 378 (2004) 316.

57. K. Gall, H. Sehitoglu, Y. I. Chumlyakov, and I. V. Kireeva *Acta, mater.* 47 (1999) 1203.
58. H. Sehitoglu, I. Karaman, X. Zhang, A. Viswanath, Y. Chumlyakov and H. J. Maier *Acta Mater.* 49 (2001) 3621.
59. V.N. Kachin, N.M. Matveeva, V.P. Sivokha, D.B. Chernov, and Yu. K. Koveristy, *Doklady Akad. Nauk SSSR* 257 (1981) 195.
60. Y. Suzuki, Y. Xu, S. Morito, K. Otsuka, and K. Mitose, *Maters. Lett.* 36 (1998) 85.
61. D. Goldberg, Y. Xu, Y. Murakami, S. Morito, K. Otsuka, T. Ueki, and H. Horikawa, *Scripta Metall. Mater.* 30 (1994) 1349.
62. W. Cai, S. Tanaka, and K. Otsuka, *Maters. Sci. Forum* 327 (2000) 279.
63. K. F. Hane and T. W. Shield, *Philosophical Magazine A*, 78 (1998) 1512.
64. J.X. Zhang, M. Sato, and A. Ishida, *Acta Materialia* 54 (2006) 1185.

BIOGRAPHICAL SKETCH

Orlando Rios was born in Elizabeth, NJ in April 18, 1978. His parents are Jose and Marta Rios both of which were both born in Cuba and are currently US citizens.

Orlando's primary language were English and Spanish as this is what was spoken in his household and neighborhood. Orlando was raised in Miami, Fl where he had his primary schooling.

At the age of eight he began attending karate classes. This continued until he began college at the age of 19. He was awarded a black belt as well as receiving high marks and recognition in several competitions. Orlando is also an established scuba diver and has completed advanced training in scuba diving including night, wreck, blue water, search and recovery and deep diving.

Upon completion of high school Orlando was educated as automotive technician at Linsy Hopkins in Miami, Fl. After which he worked on rotary engines for two years while attending Miami Dade Community College where he received an associate in arts in engineering sciences. He then attended the University Of Florida where received a bachelors degree in materials science and engineering. Afterwards Orlando completed his Masters at the University of Florida on a NASA funded GSRP three year fellowship. He spent significant time working at the NASA Glenn research centers advanced metallic division where he focused on instrumentation, instrument development and design, alloy development and advanced thermomechanical testing of high temperature shape memory alloys.

Orlando's work experience includes retail work in Eckerd Drugs Pharmacy and at Rose auto parts. He also worked as a rotary engine mechanic at CL motor sports in Miami, Fl. He also worked as a researcher at a Christian-Albrechts University of Kiel

Germany in the Materials engineering department. There he had experience working with III-V semiconductors and porous silicon. His experience there included SEM analysis, precision electrochemical etching and electrochemical impedance spectroscopy.